DOPED TIN OXIDE SUPPORTS FOR THE OXYGEN EVOLUTION REACTION

Submitted in part-fulfilment of the requirements for the degree

Master of Chemistry in Applied Sciences.

in the

Department of Chemistry

Cape Peninsula University of Technology

By

JULIE-ANN HOFFMAN

Student No: 216234379

Principal Supervisor: Assoc. Prof Mangaka Matoetoe (CPUT)

External Supervisor: Dr Rhiyaad Mohamed (UCT)

January 2022

"Wisdom begins in wonder."

–Socrates

PLAGIARISM DECLARATION

I, <u>Julie-Ann Hoffman</u>, know the meaning of plagiarism and declare the contents of this document, save for that which is properly acknowledged, represents my own work. I declare that this thesis/dissertation has not previously been submitted for academic examination towards any qualification. This thesis/dissertation has been submitted to 'Turnitin' similarity/ originality checking software and I confirm that my supervisors have seen my report and any issues have been resolved with the guidance of my supervisors. Furthermore, it represents my own opinions and not necessarily those of the Cape Peninsula University of Technology.

Signature: Date: 18th January 2022

ABSTRACT

The utilisation of hydrogen as a clean and renewable energy carrier in transport applications and as a chemical feedstock, is a promising strategy to limit fossil fuel emissions and mitigate climate change. Water electrolysis, especially proton exchange membrane water electrolysis (PEMWE), efficiently produces clean, high purity hydrogen, with virtually no carbon dioxide (CO_2) emissions when coupled with primary renewable energy sources such as solar and wind. The oxygen evolution reaction (OER) occurring at the PEMWE anode, under highly oxidative conditions, is kinetically challenging and requires large quantities of noble metal oxide electrocatalysts for feasible operations. Iridium oxide (IrO_2) is seen as the most suitable OER electrocatalyst due to its high activity and corrosion resistance. However, the high cost and scarcity of iridium limits its widespread application as an OER electrocatalyst materials in PEMWEs. As such, ways of reducing the Ir content includes the use of suitable support materials to improve the utilisation and operational lifetime of the metal.

In this thesis, the use of tin-doped indium oxide, commonly referred to as indium tin oxide (ITO), as a support material for Ir-based OER electrocatalysts was explored. Various phases of Ir-based nanoparticles, ranging from metallic or oxidic (generally referred to as IrO_x: where x ranges from 0–2) were deposited on ITO by an in-house developed metal-organic chemical deposition (MOCD) technique. The physicochemical properties of the supports and the supported electrocatalyst counterparts were determined by X-ray diffraction (XRD), scanning electron microscopy-energy dispersive X-ray spectroscopy (SEM-EDX), high resolution-scanning transmission electron microscopy (HR-STEM) and X-ray photoelectron spectroscopy (XPS). The OER performance in terms of activity and stability were investigated using the rotating disk electrode (RDE) technique in acidic electrolyte.

The results showed that the support physicochemical properties influenced the nature, activity, and stability of the MOCD IrO_x/ITO electrocatalysts. The electrocatalysts that were prepared on a low BET surface area ITO support had higher coverage of IrO_x nanoparticles over the support, higher surface Sn^{2+}/Sn^{4+} and Ir^{4+}/Ir^{3+} with lower surface In_2O_3/In(OH)$_3$ component ratios than those utilised on high BET surface area ITO support. The best performing electrocatalyst, which was active and the most stable, had uniformly distributed, small (2.4 ± 0.7 nm) size, predominately Ir metal nanoparticles with a good mass specific OER activity of 207 ± 34 A g_{Ir}^{-1} at 1.525 V vs. reversible hydrogen electrode (RHE).

ACKNOWLEDGEMENTS

SCIENTIFIC PRESENTATIONS

2019

Julie-Ann Hoffman, Ziba Rajan and Rhiyaad Mohamed

"Preparation of Iridium-Ruthenium Oxide Electrocatalysts for the Oxygen Evolution Reaction"

Poster presentation at the 30th Annual Meeting of the Catalysis Society of South Africa (CATSA), Langebaan, South Africa.

2021

Genna Moss and Julie-Ann Hoffman

"*Truth about Hydrogen*"

University-level pool Runner-up: International Partnership for Hydrogen and Fuel cells in the Economy (IPHE's) Student Infographic Challenge 2021.

TABLE OF CONTENTS

LIST OF TABLES

LIST OF FIGURES

Chapter 6:

Appendices

NOMENCLATURE

List of abbreviations

PEMWE	Proton exchange membrane water electrolysis
OER	Oxygen evolution reaction
ATO	Antimony-doped tin oxide
ITO	Indium tin oxide or tin-doped indium oxide
FTO	Fluorine-doped tin oxide
MOCD	Metal-organic chemical deposition
AWE	Alkaline water electrolysis
SOWE	Solid oxide water electrolysis
AEMWE	Anion exchange membrane water electrolysis
MEA	Membrane electrode assembly
CCM	Catalyst coated membrane
PFSA	Perfluorosulphonic acid
CL	Catalyst layers
PTL	Porous transport layer
GDL	Gas-diffusion layer
MPL	Microporous layer
HER	Hydrogen evolution reaction
EDX	Energy-dispersive X-ray spectroscopy
HAADF	High angle annular dark field
FWHM	Full width at half maximum
XRD	X-ray diffraction
TEM	Transmission electron microscopy
HR-STEM	High resolution-scanning transmission electron microscopy
SEM-EDX	Scanning electron microscopy-energy dispersive X-ray spectroscopy
BET	Brunauer, Emmett and Teller
ICP-OES	Inductively coupled plasma-optical emission spectroscopy
XPS	X-ray photoelectron spectroscopy
RDE	Rotating disk electrode

RHE	Reversible hydrogen electrode
CV	Cyclic voltammetry
CA	Chronoamperometry
EIS	Electrochemical impedance spectroscopy

List of units of measurements

V	Volts (potential unit of measurement)
Mt	Megaton (10^6 t, mass unit of measurement)
kt	Kiloton (10^3t, mass unit of measurement)
eV	Electron volt (energy unit of measurement)
kV	Kilovolts (10^3V, potential unit of measurement)
nm	nanometre (10^{-9} m, distance unit of measurement)
mg	Milligrams (mass unit of measurement)
wt.%	Weight percent (mass unit of measurement)
°C	Degrees Celsius (temperature unit of measurement)
°C min^{-1}	Degrees Celsius per minute (temperature unit of measurement)
mL min^{-1}	Millilitres per minute (rate unit of measurement)
hr	Hour (time unit of measurement)
A	Amps (current unit of measurement)
A g_{Ir}^{-1}	Amps per gram of iridium content (current density unit of measurement)
ml	Millilitres (10^{-3}L, volume unit of measurement)
rpm	Rotations per minute (speed unit of measurement)
μL	Microlitres (10^{-6} L, volume unit of measurement)
m^2g^{-1}	Meters square per gram (surface area unit of measurement)

CHAPTER 1: INTRODUCTION

This chapter provides the current status of the hydrogen-based economy and brief description on the current challenges in proton exchange membrane water electrolysis including the need for supported electrocatalysts for the oxygen evolution reaction. The motivation for the investigation of ITO as an OER catalyst support material as the focus of this study is addressed. In addition, the chapter outline of the thesis is also presented.

1.1 Background

The increasing greenhouse gas emissions can be attributed to the continuous use of fossil fuels to meet the high energy demand of the world's growing population (Da Silva Veras et al., 2017). At the recent 26th UN Climate Change Conference, COP26 (Glasgow 2021) (United Nations, 2021) world nations committed to further accelerate the process of reaching the Paris Agreement (United Nations Framework Convention on Climate Change, 2021) goals to limit greenhouse gas emissions and mitigate climate change. The utilisation of hydrogen as a clean and renewable energy carrier in transport applications and as a chemical feedstock, is a promising strategy to limit the detrimental environmental issues driven by fossil fuel emissions (Sapountzi et al., 2017). To achieve global net-zero emission by 2050, it is estimated that an increase in hydrogen production from the current 90 Mt to 528 Mt of hydrogen will be required (International Energy Agency, 2021b).

Hydrogen can be produced using a variety of processes such as thermal (natural gas reforming, biomass, and coal gasification etc.), photochemical, (water splitting via solar energy absorbed by a semiconducting photoelectrode immersed in an aqueous electrolyte) and electrochemical processes (water splitting via an electrochemical cell using direct current in an aqueous solution) (Kalamaras & Efstathiou, 2013). However, the global statistics in 2020, showed that hydrogen production was almost completely dominated by fossil fuel-based processes, whereas water electrolysis generated only a small quantity of 30 kt (~0.03% of total 90 Mt hydrogen produced in 2020) (International Energy Agency, 2021a). This fossil-fuel driven hydrogen production led to direct CO_2 emissions of ~900 Mt, which was equivalent to the amounts produced by both Indonesia and United Kingdom in 2020. To lower these emissions, utilisation of carbon capture and storage technologies must be implemented which is not yet a widely adopted approach (International Energy Agency, 2021a).

Proton exchange membrane water electrolysis (PEMWE) when coupled with primary renewable energy sources i.e., solar and wind, enables efficient production of clean, high purity hydrogen (so-called green hydrogen), with virtually no CO_2 emissions. Current state-of-the-art PEMWE technology utilises precious group metal (PGM) based electrocatalysts for both cathodic and anodic processes. Anodic oxygen evolution reaction (OER) is considered to be specifically challenging due to requirement for high reaction overpotential and limitations in choice of materials that demonstrate sufficient catalytical activity and stability under operating conditions. Iridium oxide (IrO_2) is seen as the most suitable OER electrocatalyst due to its high activity and corrosion resistance. However, its high cost and scarcity are the limiting factors when considering PEMWE scale-up and widespread commercialisation (Fabbri et al., 2014).

To overcome these challenges, industry and academia are focused on the development of supported electrocatalysts where the reduction in Ir content and increase in catalyst utilisation and operational lifetime can be optimised. (Reier, Oezaslan & Strasser, 2012). Unlike in proton exchange membrane fuel cells, where platinum nanoparticles are supported on carbon materials, OER catalysts use metal oxides instead, as carbon would corrode at the highly oxidizing anodic operating potentials (Hartig-Weiss et al., 2020). Umicore AG & Co.KG developed the first supported catalyst at industrial scale: iridium oxide supported on titania (IrO_2/TiO_2). However, the lack of support electronic conductivity and low support surface area are the major drawbacks for this catalyst, which is why high iridium loadings (75 wt.% Ir) are necessary (Hartig-Weiss et al., 2020; Oakton et al., 2017).

Doping can considerably improve the conductivity of oxides as in the case of antimony-doped tin oxide (ATO), tin-doped indium oxide (ITO) and fluorine-doped tin oxide (FTO) (Oh, Hyung-Suk, Nong & Strasser, 2015; Puthiyapura et al., 2014a; Silva et al., 2020). The usage of these supports resulted in very fine dispersion of Ir-based nanoparticles (IrO_x: referring to either metallic iridium for x=0 or iridium oxide for x=2) which significantly increased the active catalytic surface area, and consequently improved the OER performance (Böhm et al., 2019; Oh, Hyung-Suk, Nong & Strasser, 2015; Xu et al., 2012). However, Ir deposition by conventional wet chemistry process may lead to the poor dispersion of the catalyst nanoparticles over the support and as such more robust, and simple methods of deposition have been explored (Lebedev & Copéret, 2019; Rajan et al., 2020). Recently, a metal-organic chemical deposition technique (MOCD), developed in-house, was used to prepare highly crystalline, small (1–3 nm) iridium oxide nanoparticles on ATO support with good activity and

stability towards the OER in acidic electrolyte. The high performance of the ATO supported IrO$_2$ electrocatalyst was attributed to the uniform distribution of the predominately crystalline, rutile IrO$_2$ nanoparticles resulting in a greater iridium utilisation over the support (Rajan et al., 2020).

In this study, the extension of the MOCD technique to the use of ITO as a support material was investigated. The physicochemical properties of various ITO supports and their supported electrocatalyst counterparts were studied to understand their influence on their electrochemical behaviour towards the OER in acidic media. This work contributes towards the development of next generation electrocatalysts for PEMWE applications.

1.2 Problem statement

The production of supported electrocatalysts for the OER, that are both stable and active is challenging, primarily due to the criteria associated to the development of high-performance supports such as surface area, conductivity, and dissolution stability (Fabbri et al., 2014; Sasaki et al., 2010). While oxide support materials are the most suitable for the OER, they lack electronic conductivity, so they must be doped. As reported in literature, promising doped oxide catalyst support materials with good electronic conductivity such as tin-doped indium oxide (ITO) would provide an improved physical surface for the fine dispersion of iridium oxide. However, ITO has not been recommended as an OER support material as it known to suffer from chemical instability particularly in an acidic electrolyte under anodic OER operating potentials and this is seen in the Pourbaix diagram (Pourbaix, 1974), where the host lattice (In$_2$O$_3$) of ITO has shown to be unstable in acidic environments (pH=1) (Benck et al., 2014; Geiger et al., 2017). On the contrary, other studies have reported the use of ITO as an efficient OER support material (Lebedev & Copéret, 2019; Lebedev et al., 2020; Puthiyapura et al., 2014b). Therefore, to gain further fundamental understanding of ITO as an OER support material it is necessary to determine whether the nature of the catalytic nanoparticles (Ir species present on the support; Ir coverage over the support etc) and/or the nature of the support (In$_2$O$_3$: SnO$_2$ ratio; electronic conductivity; surface area etc) could facilitate the stabilisation of ITO. To investigate the nature of both catalytic particles and support, the use of a facile deposition technique, in-house metal-organic chemical deposition (MOCD) (Rajan et al., 2020), to deposit uniformly distributed, small IrO$_x$ catalytic nanoparticles on various ITO supports and investigate the conditions that may lead to ITO being stable at OER conditions.

1.3 Hypothesis & Assumptions

As the utilisation of the MOCD technique produced uniformly distributed, small (1–3 nm) crystalline IrO_2 nanoparticles on ATO support, which led to an increased stability compared to commercially available OER catalysts (Rajan et al., 2020) it would be assumed that certain catalyst-support properties are exhibited and that these properties stabilise an oxide such as ITO which is known to be unstable under OER conditions.

It is hypothesised that:

1. The MOCD technique can be successfully used with other oxide supports such as ITO while maintaining the uniformly distributed, small IrO_x nanoparticles over the support.
2. The nature of the support influences the properties of the IrO_x catalytic nanoparticles.
3. Under certain conditions (dependent on properties of IrO_x catalytic nanoparticles present), the ITO support can be stabilised

1.4 Delimitations

Low quantity (200–250 mg) sample sizes were synthesised due to the apparatus availability, time constraints and costing of precursors.

Only ex-situ electrochemical testing was performed in this study, due to equipment constraints. Thus, only ex-situ mass specific OER performance and stability were investigated and studied.

Extensive physical characterisation studies (synchrotron characterisation techniques such as Extended X-ray fine structure (EXAFS) and X-ray absorption near edge spectroscopy (XANES) etc) and in-situ electrolyser testing are beyond the scope of this study.

1.5 Aim & Objectives

The aim of this study was to investigate the viability of tin-doped oxides such as ITO as an OER catalyst support material by determining whether certain catalyst–support properties can stabilise an oxide such as ITO for the highly oxidising OER operating potentials.

As this was an initial study, to investigate the influence of catalyst–support properties, commercially available ITO with various physiochemical properties (particle size, BET surface area; conductivity; In_2O_3: SnO_2 ratios) are used. During this study, the approach of improving the activity and/or stability using a conductive support material was also explored.

The objectives of this study were:

1. Deposit IrO_x (x = 0–2) onto the commercially available ITO support materials, with varying physiochemical properties such as in composition and particle size, using the in-house metal-organic chemical deposition (MOCD) technique (Rajan et al., 2020).

2. Determine the suitability of the commercially available ITO support materials for the preparation of OER catalysts through physical characterisation and electrochemical characterisation in order to understand influence of varying their physiochemical properties.

3. Characterise the synthesised IrO_x/ITO electrocatalysts to understand their electrochemical behaviour on various commercially available ITO support materials.

Overall, this study is to gain a better understanding of using supported catalysts for OER and the influence of their properties on their performance as an OER electrocatalyst, using general lab-based characterisation equipment. This study is significant as it showcases how catalyst-support properties of a IrO_x/ITO supported electrocatalyst can stabilise ITO which is known to be unstable in OER conditions.

1.6 Thesis outline

The study is comprised of eight chapters.

Chapter 1: Highlights the current status of hydrogen-based economy and challenges faced by PEMWE including the promising approach of using supported OER electrocatalysts. The outline and the rationale for the research approach taken in this study is also provided.

Chapter 2: Provides background on water electrolysis, with focus placed on PEMWE and motivation for iridium-based supported OER electrocatalysts, particularly use of ITO as the catalyst support material.

Chapter 3: Description of the experimental methodology including the catalyst deposition technique, physical and electrochemical characterisation used in this work.

Chapter 4: Commercially available ITO catalyst support materials were physically and electrochemically characterised to gain an understanding of the catalyst support

material prior to Ir deposition. The physical characterisation was also compared to data provided by the supplier of the material.

Chapter 5: IrO$_x$/ITO electrocatalysts prepared by the in-house metal-organic chemical deposition technique were investigated through physical characterisation techniques including high resolution- scanning transmission electron microscopy and X-ray photoelectron spectroscopy.

Chapter 6: The OER electrochemical performance of the prepared IrO$_x$/ITO electrocatalysts were investigated, coupled with information acquired from the physiochemical properties of these electrocatalysts in order to gain understanding of the effect of the physiochemical properties on the electrochemical performance of the electrocatalysts.

Chapter 7: The overall conclusions of this study and recommendations for future work that can be done to investigate catalyst support materials.

CHAPTER 2: LITERATURE REVIEW

Chapter 2 provides a background on water electrolysis with a more in-depth description on proton exchange membrane water electrolysis. A literature overview of the utilisation of doped oxide support materials for iridium-based supported electrocatalysts is discussed and the metal-organic chemical deposition technique for the preparation of iridium-based supported electrocatalysts is introduced.

2.1 Water electrolysis

Fundamentally, water electrolysis is the application of electrical energy to water molecules to produce chemical energy in the form of hydrogen, with oxygen as a by-product (Holladay et al., 2009). Currently, there are four main types of water electrolysis technologies used i.e. alkaline water electrolysis (AWE), solid oxide water electrolysis (SOWE), proton electron membrane water electrolysis (PEMWE) and anion exchange membrane water electrolysis (AEMWE) (Kumar & Himabindu, 2019). Alkaline-based electrolysis is the most well-developed and commercialised technology as it is the cheapest (in terms of capital cost) and uses non-noble metal electrocatalysts. The alkaline electrolysis process utilises an asbestos diaphragm which separates the anode and cathode electrodes and their respective electrocatalytic products in alkaline (KOH/NaOH) electrolyte. However, its main disadvantages are that it has a lower energy efficiency (70–80%) due to limited current densities that can be achieved (below 400 mA.cm^{-2}) and its operation requires low pressures (3–30 bar) with temperatures ranging from 30–80°C. In contrast, SOWE is not as well-established (largely still at the laboratory scale stage), and while having a higher energy efficiency (90–100%), it suffers from corrosion and degradation issues that need to be overcome. This system uses a solid proton conductive ceramic electrolyte membrane instead of a diaphragm and electrolyte as seen in AWE. (Holladay et al., 2009; Kumar & Himabindu, 2019). PEMWE has lower energy efficiency of (80–90%) compared to SOWE, however it has various advantages such as high current density (above 2 A.cm^{-2}), compact design, fast start-up and shut down, produces high purity hydrogen and oxygen as by-products and has a minimal carbon footprint. In this process, the anode and cathode with their respective produced gases are separated by a proton conducting membrane, which facilitates the mobility of the protons from the anode to cathode, while H$_2$O is pumped over the anode. However, the main challenge of this technology is the reduction of high production costs of the components (e.g., noble metal

electrocatalysts and bipolar plates) while trying to maintain high energy efficiency (Ahmad Kamaroddin et al., 2021; Kumar & Himabindu, 2019). Lastly, AEMWE is a new emerging alkaline electrolysis technology which extends the advantages of PEMWE to an alkaline membrane as anionic conductive polymers membranes are used instead of the asbestos diaphragm. The main benefit is that this process can use milder alkaline electrolytes and as such possibly a more cost-effective system (e.g., cheaper electrocatalysts and components etc). However, the main challenges for AEMWE are low conductivity, relatively lower energy efficiency, requires large catalyst loadings and lacks membrane stability. To this end, this technology is still at the early stage of development and further efforts, especially for catalyst design and synthesis are needed.

2.2 Proton Exchange Membrane Water Electrolysis

The use of proton exchange membranes (PEM) in the process of electrolysis was first invented by Thomas Grubb and Leonard Niedrach at General Electric Co (Odetola et al., 2016). This technology was developed in 1966 as an alternative to alkaline water electrolysis and its many drawbacks. The PEM worked both as electrolyte (proton conductor) and gas separator. Its initial utilisation in water electrolysis was for an undersea life support unit by the US Navy (Bender et al., 2019; Odetola et al., 2016).

PEM water electrolysers are commercially available, however due to the high capital and operational costs, they have only been employed in niche applications such as life support units and industrial gas supply. The technology produces "green" hydrogen as it leaves very little carbon footprint, especially when coupled with renewable energy sources (i.e., solar and wind). According to United States Department of Energy, for this technology to reach the public market, the cost of hydrogen will have to be 2 $/kg or less, with a life span of over 40 000 hrs. This can only be achieved by large investments and significant efforts in research and development of this technology (Bender et al., 2019; Brauns & Turek, 2020).

In 2021, Air Liquide (FR) has built the world's largest PEM electrolyser to date, in Bécancour, Québec. This new 20 MW PEM electrolyser, coupled with renewable energy sources can produce 8.2 t of green hydrogen per day (Gulf Publishing Holdings LLC, 2021). This indicates an improvement in the output of power of this technology as previously, in 2020, Japan had the world's largest facility for green hydrogen production (10 MW electrolyser coupled with 20 MW solar panels). Japan's project was developed with several partnerships including

Toshiba and Tohoka Electric Power and the produced hydrogen was used as a fuel for proton exchange membrane fuel cell operated cars and buses in Tokyo (Lee, 2020). Before that, in 2019, the largest plant was a 6MW facility, which utilised Siemens' electrolysers for green hydrogen production for the steel industry in Austria (Collins, 2019).

A joint project by ITM power and Linde will be building the next "world's largest PEM electrolyser" with plant production starting in 2022. The 24 MW electrolyser will produce green hydrogen for the Linde's industrial customers as well as for hydrogen refuelling stations (Radowitz, 2021). Siemens recently have announced their aim to produce a 1 GW PEM electrolyser by 2030 (Siemens Energy, 2021). From these recent developments of larger-scale PEM electrolysers it shows that this technology is gaining momentum.

In PEMWE technology, water electrolysis is performed by a module which is composed from stacked unit cells consisting of membrane electrode assemblies (MEAs) sandwiched between bipolar plates. Figure 2.1 shows a schematic representation of the unit cell and summarises the electrochemical reactions that occur during water electrolysis. The central part of an MEA is a catalyst coated membrane (CCM). Typically, CCMs use perfluorosulphonic acid (PFSA) membranes (50–200 µm thickness) such as Nafion®, which are well-known due to their good ionic conductivity and are widely used in industry. Membrane is coated with catalyst layers (CLs), which generally have thickness of 10 µm, and consist of PGM electrocatalysts. On the cathode side: Pt-based catalysts e.g., Pt/C are used and on the anode side: Ir-based catalysts e.g., IrO_2 are deposited (Ahmad Kamaroddin et al., 2021; Bühler et al., 2019). The CCM is clamped between a porous transport layer (PTL) on the anode side and a gas-diffusion layer (GDL) covered by a microporous layer (MPL) on the cathode side. In addition, bipolar plates are placed at each end (Fornaciari et al., 2020). PTL, usually made from sintered titanium foam or felt, allows the transport of the reactants and produced gas to and from the anode catalyst layer (Bühler et al., 2019; Moschovi et al., 2021). GDL and MPL, which are made from carbon materials, (Polonsky´ et al., 2017) uniformly distribute the produced gas from the cathode catalyst layer to the bipolar plate (Odetola et al., 2016; Regmi et al., 2020). Bipolar plates are made from materials such as graphite, stainless steel or titanium. These plates have channel-like structures (flow field) which range from 0.3 to 3 mm and are used for the transport of the reactants and produced gas, to facilitate coolant handling and partake in the electrical connections of the cell (Bareiß et al., 2019; Bühler et al., 2019; Odetola et al., 2016).

In essence, the MEA enables the process of water splitting into hydrogen and oxygen with application of electrical energy (Holladay et al., 2009). During this process, water molecules and ions are transferred through the membrane from anode to cathode. At the anode, which utilised Ir-based catalyst, oxygen evolution reaction (OER) occurs where water molecules are split into protons and O_2 gas. Only the protons travel through the membrane to the cathode (catalyst is Pt supported on carbon) where the hydrogen evolution reaction (HER) takes place, and the protons recombine and form H_2 gas. During this reaction, electrical energy is supplied to the cell through the bipolar plates and converted into chemical energy. The electrons travel from the anode via an external circuit to the cathode, where they are used in the HER. The O_2 gas at the anode and H_2 gas at the cathode exit via channels of their respective bipolar plates. (Abdol Rahim et al., 2016; Holladay et al., 2009; Moschovi et al., 2021).
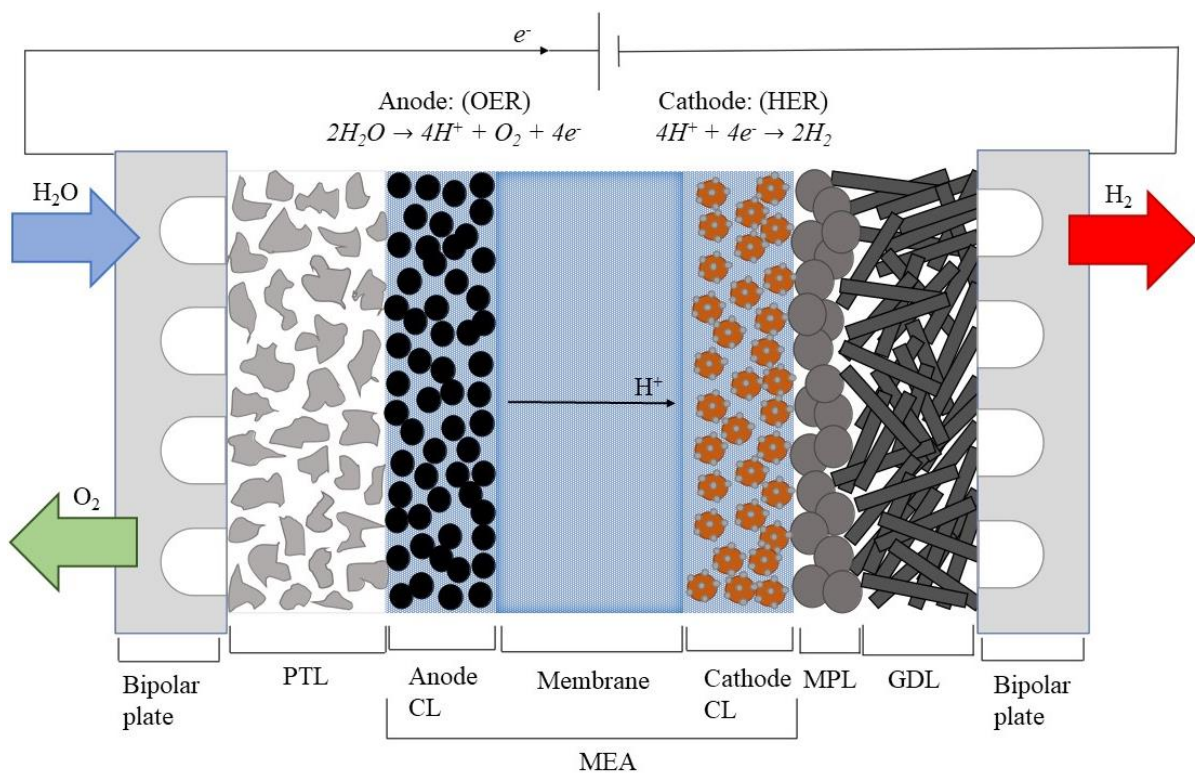
Figure 2.1: Schematic diagram of proton exchange membrane water electrolysis unit cell.

While PEMWE is an appealing means of hydrogen production, it suffers from several drawbacks. Such as the use of scarce, expensive PGM catalyst materials (e.g., IrO_2 and RuO_2) and components (e.g., titanium PTLs and bipolar plates) due to these materials being corrosion resistance (to an extent) in the acidic OER environment and being able withstand the high applied over voltage (~2 V). However, despite the use of these corrosion resistance materials,

this technology still suffers from low stability compared to other technologies (Ahmad Kamaroddin et al., 2021; Carmo et al., 2013; Kumar & Himabindu, 2019).

2.3 Unsupported catalysts for OER

Compared to HER, the OER is a kinetically challenging process due to the involvement of a four electron-proton coupled reaction at the anode, which leads to a large overpotential which hinders the overall water-splitting reaction. To overcome this, the development of suitable electrocatalysts with low overpotential and high activity and stability is essential (Fabbri et al., 2014; Qu et al., 2021).

Typically, precious metal oxides, such as iridium oxide (IrO_2) and ruthenium oxide (RuO_2), are currently used in state-of-the-art technology (Marshall et al., 2006; Trasatti, 1984; Wei et al., 2019). RuO_2 is a more active catalyst compared to IrO_2, but it lacks the stability that is required for industrial-scale production of hydrogen with PEMWE (Reier, Oezaslan & Strasser, 2012). Literature search reveals that, various types of OER electrocatalysts have been synthesised to improve electrochemical performance and/or increase catalyst utilisation and stability and therefore contribute towards the PEMWE process cost reduction. Some examples include iridium-ruthenium mixed oxides (Audichon et al., 2014; Mamaca et al., 2012; Pham et al., 2015; Saveleva et al., 2016); iridium-iridium oxide core-shells (Nong et al., 2014; Tackett et al., 2018) and high surface area amorphous iridium oxide (Abbott et al., 2016; Pfeifer et al., 2016).

These studies found that iridium-ruthenium mixed oxides were more active than IrO_2 electrocatalysts and that incorporation of IrO_2 with RuO_2 does lead to a stabilisation of the Ru-based catalyst, but that was not sufficient for the OER conditions (Audichon et al., 2014; Mamaca et al., 2012; Pham et al., 2015; Saveleva et al., 2016). High surface area amorphous iridium oxide was very active but lacked stability (Abbott et al., 2016). Preparation of core-shells proved to lower the Ir content by a factor of 2–3 and yielded a more electrochemically active catalyst than IrO_2, but scaling-up of this catalyst to relevant industrial scale is challenging. Therefore, further development of the lowering of the noble metal content to produce a more cost-effective catalyst is required (Nong et al., 2014; Tackett et al., 2018).

2.4 Supported electrocatalysts for OER

To reduce the cost and quantity of rare noble metals used in PEMWE and to make it more economically feasible for large scale hydrogen production, the use of supported catalysts for the OER has been established to be a promising approach (Hartig-Weiss et al., 2020). The main requirements for the support materials are high surface area, high electronic conductivity, and stability. As the OER conditions are highly oxidative, both electrochemical and chemical stability of a support material needs to be taken into consideration. High surface area supports ensure that the deposited catalyst nanoparticles are well-dispersed over the support to provide greater noble metal utilisation. High electronic conductivity provides sufficient pathways for electron to move throughout the reactive interfaces for high-rate electrochemical reactions. The electrochemical and chemical stability of the support is important as the deposited catalyst is dependent on the support's stability in the OER operating conditions and the interaction between the catalyst and support has been seen to stabilise the deposited catalyst nanoparticles (Böhm et al., 2019; Kim et al., 2021). These catalyst–support electronic interactions have been found to be evident between oxide supports and IrO_x nanoparticles, while on carbon supports were found to be mostly non-existent (Oh, H.S. et al., 2016).

Metal oxides are well-established as OER support materials as they are typically stable under the operating potentials. As such, titanium oxide (TiO_2) and tin oxide (SnO_2) are generally used. However, the major drawback of these materials is that they lack the electronic conductivity to completely facilitate high-rate electrochemical reactions. A solution to this drawback is the incorporation of dopants to TiO_2 and SnO_2 support materials (Kim et al., 2021).

2.5 Doped Oxide Supports

The doping of SnO_2 with Sb (V), In (III) or F has shown to significantly increase its electronic conductivity (Oh, Hyung-Suk, Nong & Strasser, 2015; Puthiyapura et al., 2014a; Silva et al., 2020). Oh, Hyung-Suk, Nong & Strasser (2015) reported an approximate 100-fold increase in electrical conductivity from the synthesised undoped SnO_2 to the doped oxides. The dopants reported in this work, were 6.2 at% Sb in antimony-doped tin oxide (ATO), 2.3 at% F in fluorine-doped tin oxide (FTO) and 9.1% Sn in tin-doped indium oxide (ITO) (Oh, Hyung-Suk, Nong & Strasser, 2015). However, some studies have suggested that these doped oxide materials may still not be stable enough in OER operating conditions.

For example, Geiger et al. (2017) studied in detail the corrosion of ITO, ATO and FTO in acidic electrolyte (0.1M H_2SO_4) and reported that all the materials were unstable at high cathodic and anodic potentials due to the combination of electrochemically and chemically driven dissolution processes (Geiger et al., 2017; Pourbaix, 1974). The findings of the study showed that trend for dissolution was the following: $In_2O_3 \gg Sb_2O_3 \gg SnO_2$.

This work found that the dissolution during the anodic polarisation cannot be easily explained especially for potentials from 2 V to 3.2 V vs. RHE. They proposed an explanation that an additional electrochemical process was taking place: evolution of oxygen from lattice units of the materials as described by reactions (1–3) below.

$$In_2O_3 \rightarrow 2In^{3+} + 1.5\ O_2 + 6e^- \tag{1}$$

$$SnO_2 \rightarrow Sn^{4+} + O_2 + 4e^- \tag{2}$$

$$Sb_2O_5 \rightarrow 2Sb^{5+}\ 2.5\ O_2 + 10e^- \tag{3}$$

It was concluded that FTO was the most relatively stable doped oxide, followed by ATO and then ITO. (Geiger et al., 2017).

However, in a study by Benck et al. (2014), where potential windows of various support materials in acidic, neutral and basic electrolytes were investigated, it was seen that ITO could be electrochemically inert for the potential range from -0.46 V to 2.15 V vs. RHE in an acidic electrolyte (pH=1). This would suggest that the main source of dissolution would be due to chemical instability rather than due to the applied electrochemical potentials. In addition, it was noted that the overall stability of ITO as a support material is not only dependent on the electrolyte and potential window applied but also on the amount of coverage of supported catalytic particles present after deposition (Benck et al., 2014).

2.6 Deposition of IrO_x onto Doped Oxide Supports

Various wet chemistry deposition routes such as Adams' fusion, polyol, solvothermal, microwave assisted hydrothermal have been used to deposit IrO_x (x = 0–2) onto doped oxide synthesised supports (Böhm et al., 2019; Hartig-Weiss et al., 2020; Massué et al., 2017) and commercial supports (Liu et al., 2015; Puthiyapura et al., 2014a). The morphology of the IrO_x has been seen to affect the electrochemical performance. For example, it has been shown that an amorphous iridium oxide is highly active but lacks stability, while rutile IrO_2 is considerably less active, but is stable (Abbott et al., 2016). Iridium oxide is described as amorphous iridium

13

oxide when both iridium oxidation states Ir^{3+} and Ir^{4+} are present in the material, while for rutile IrO_2, Ir^{4+} is the dominant oxidation state (Massué et al., 2017; Pfeifer et al., 2016). Metallic iridium also exhibits OER activity upon being subjected to oxidising electrochemical potentials, because it immediately forms a hydrous, amorphous iridium oxide (Saveleva et al., 2018).

Wet chemistry deposition routes typically generate catalysts with iridium loadings in the range of 15–60 wt.%, which is not a cost-effective approach. This suggests that applying a deposition method that generates a well-performing supported electrocatalyst at low iridium loadings, with increased iridium utilisation, would be desired.

Recently, one such deposition route has been reported by Rajan et al (2020) where a one-step metal-organic chemical deposition (MOCD) technique was used to obtain 1–5 nm size rutile IrO_2 nanoparticles, with predominantly Ir^{4+} oxidation state, that were uniformly distributed and epitaxially anchored onto a high surface area, conductive ATO support. Interestingly, this type of anchoring may have encouraged the growth of rutile IrO_2 nanoparticles during the deposition process due to the connecting of their rutile lattices. This technique showed that well-dispersed, small IrO_x nanoparticles over a doped oxide support prove to produce an electrocatalyst that was both active and stable. Evidently, this deposition technique is able to promote efficient iridium utilisation over a support material, which is required for achieving improved electrochemical performance at lower iridium loadings. The reported supported electrocatalyst had a low iridium loading of 9 wt.% and showed a significantly higher OER performance compared to a IrO_2/TiO_2 commercial benchmark.

Furthermore, the uniform distribution of relatively small IrO_x nanoparticles (2–8 nm size) onto a doped oxide support, with a resulting large active surface area have led to an improved electrochemical performance (Böhm et al., 2019; Hartig-Weiss et al., 2020; Puthiyapura et al., 2014a; Puthiyapura et al., 2014b). This approach has also been seen to substantially decrease the iridium mass loading on the support material relative to Ir utilisation, which is significant as it would lower the electrocatalyst cost for industrial-scale production of hydrogen with PEMWE (Böhm et al., 2019; Ledendecker et al., 2019; Oh, H. S. et al., 2015). Doped-oxide supported electrocatalysts have also proven to have a higher performance than the Ir-black and IrO_2/TiO_2 commercial benchmarks (Hartig-Weiss et al., 2020; Lebedev & Copéret, 2019; Lebedev et al., 2020; Rajan et al., 2020)

Recently, it has been reported that IrO_x/ITO electrocatalysts have been successfully explored as OER electrocatalysts with their initial activities being comparable to IrO_x/ATO electrocatalysts (Lebedev & Copéret, 2019) and superior to Ir and IrO_2 electrocatalysts (Lebedev et al., 2020). This contradicted the studies (Benck et al., 2014; Geiger et al., 2017) that showed ITO would not be efficient as an OER support material due to its instability.

To this end, it would be interesting to investigate whether or not ITO can be efficient used as an OER support material through the application of the robust and simple MOCD technique for the preparation of IrO_x/ITO electrocatalysts.

CHAPTER 3: EXPERIMENTAL PROCEDURE

This chapter reports on the deposition technique used to prepare supported OER electrocatalysts and summarises the physical and electrochemical methods used to characterise these electrocatalysts.

3.1 Preparation of IrO$_x$/ITO by metal-organic chemical deposition

All IrO$_x$/ITO supported electrocatalysts were prepared using a previously developed in-house MOCD technique. **Figure 3.1**: Schematic representation of the MOCD technique set up (adapted from Rajan et al. 2020) Figure 3.1 illustrates the reactor system used in this work. This system was originally established by Taylor et al. (2016), and subsequently adapted in works of Jackson, Conrad & Levecque (2017), Mohamed et al. (2018) and Rajan et al. (2020).
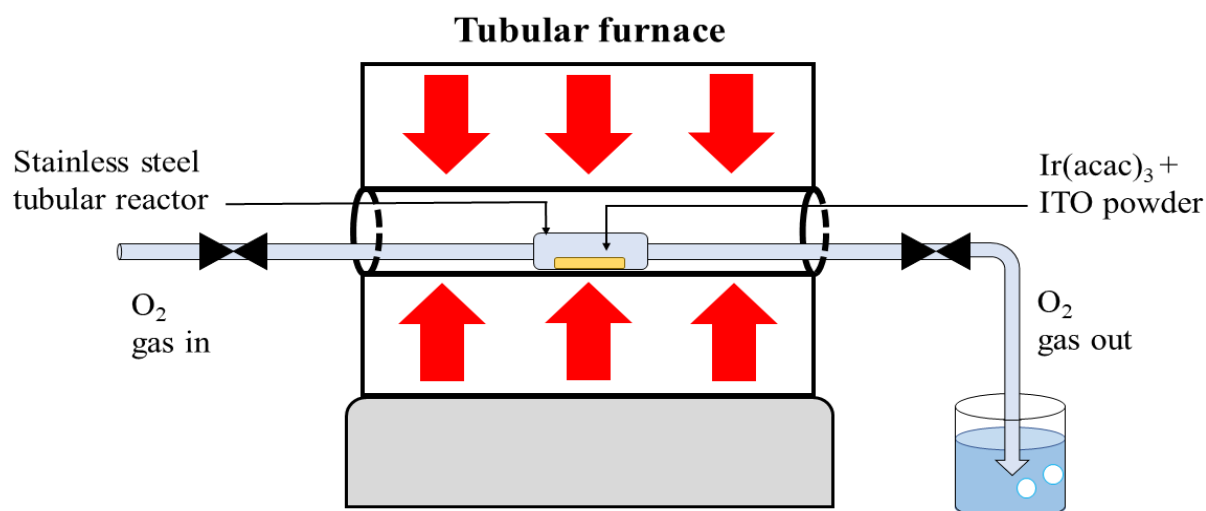
Figure 3.1: Schematic representation of the MOCD technique set up (adapted from Rajan et al. 2020)

Four different commercially available ITO nanopowder support materials (US Research Nanomaterials Inc., 99.99% purity), with varying In$_2$O$_3$:SnO$_2$ (95:5 or 90:10 wt.%) and varying average particle size (small (14 nm) and large (up to 75 nm)) were used as supports for IrO$_x$ deposition. Refer to *Appendix A* for the chemical product and equipment information, and *Chapter 4* for more information regarding the ITO support material.

A nominal loading of 20 wt.% iridium was used for all the electrocatalysts discussed in this work. To achieve this 200 mg of ITO nanopowder was used as the support material with 132 mg of the metal organic precursor iridium (III) acetylacetonate, Ir(acac)$_3$. The following

outlines the IrO$_x$ deposition procedure applied for all the electrocatalysts utilising various ITO nanopowders supports: ITO nanopowder and Ir(acac)$_3$ were mixed and crushed together using an agate mortar and pestle. The mixture was then transferred to a 20 mL sample holder of the tubular reactor which was placed into a tubular furnace. The heat treatment involved two stages. The first stage was the heat treatment from room temperature to 120 ℃, with a 3.33 ℃ min^{-1} ramp rate followed by a hold at 120 ℃ for 0.5 hr to remove the water from the mixture. During this stage, oxygen gas was introduced through the reactor tube at rate of 20 mL min^{-1} to fill the whole reactor. After 1 hr, the stainless-steel tubular reactors' valves were closed, sealing the oxygen gas with the mixture in the reactor. The second stage involved the reactor being heated to the deposition temperature of 320 ℃, with a 5 ℃ min^{-1} ramp rate and holding at this temperature for 2 hr. Thereafter, the reactor was cooled down at room temperature prior to the IrO$_x$/ITO electrocatalyst powder being retrieved.

3.2 Physical Characterisation Techniques

To understand the electrochemical performance of the prepared electrocatalysts, the physicochemical properties of both the support material and the electrocatalysts were investigated. In the following section, a description of the method and the experimental details for each technique is outlined.

3.2.1 X-ray Diffraction

X-ray diffraction (XRD) analysis was used to investigate support and electrocatalyst crystallographic structure.

The method is based on the principle of coherent scattering of X-ray radiation, in directions that adhere to Bragg's law, which occurs due to the defined structure of the crystal unit cells (Khan et al., 2020; Niemantsverdriet, 2007). Bragg's law (refer to Figure 3.2) describes the relation between the spacing of atomic planes (d) in crystals, and angles (θ) at which the incident X-ray beam with a wavelength (λ) gets diffracted from crystalline planes producing constructive interference (Niemantsverdriet, 2007).

$$n\lambda = 2d\ \sin\theta$$
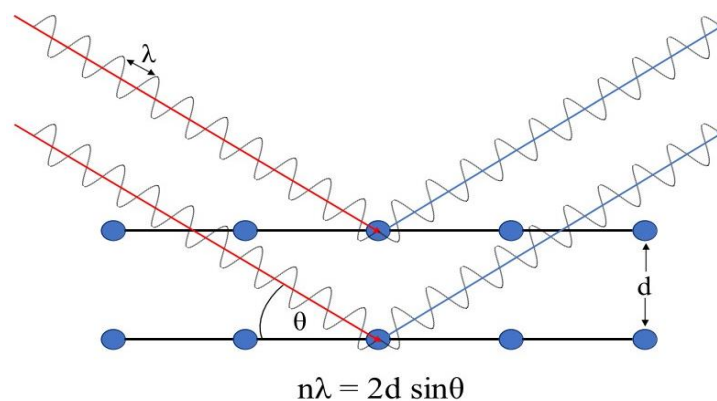
Figure 3.2: Representation of X-rays scattering in directions which adhere to Bragg's law, from atomic planes.

X-ray diffractograms are widely used to obtain structural features of nanoparticle materials such as crystal structure and crystallite size. The crystallite size is determined from the broadening of a diffraction peak provided that the crystallite size observed is greater than that of the detection limit of the instrument (3 nm). The Scherrer equation which uses the full width at half maximum (FWHM) of a diffraction peak, is used to determine average crystallite size of a sample, (Akbari, 2011; Che & Ve´drine, 2012; Khan et al., 2020)

$$\text{Scherrer equation: } D = \frac{k\lambda}{B Cos\theta}$$

Here D is the calculated crystallite size, λ is the diffraction wavelength of the X-ray source, B is the corrected FWHM, θ is the diffraction angle of the peak and k is the Scherrer constant or constant of proportionality (in this study, the value of $k = 0.9$ was used for the calculation).

3.2.1.1 Experimental details

In this work, a Bruker D8 Advance diffractometer operating at 40 kV with a Co-Kα radiation source (kα₁ = 0.178897 nm) was used to perform X-ray Diffraction measurements on the commercially available support ITO materials and MOCD prepared IrO_x/ITO electrocatalysts at the University of Cape Town. The plotting of graphs and determination of the FWHM was done using Origin 2018 Analysis & Graphing software.

3.2.2 Transmission Electron Microscopy

Transmission electron microscopy (TEM) imaging analysis was used to investigate the microstructure of the support and electrocatalyst nanoparticles and their particle size distribution.

TEM utilises a finely focused high energy electron probe to obtain information on structure, morphology, size and distribution of materials. The requirement is that material of interest (nanoparticles or thin films) is stable under the vacuum and thin enough to allow electron beam to pass through and form a projection image from (Niemantsverdriet, 2007; Wang, 2000).

In the context of the catalyst investigation, this characterisation technique enables the individual catalyst nanoparticles and support material to be directly observed and measured to provide data for nanoparticle size and morphology, nanoparticle size distribution, crystalline nature, material composition and distribution/dispersion (Akbari, 2011).

High-resolution scanning transmission electron microscopy (HR-STEM) is a modern TEM system which allows electron beam to be rastered across the sample in order to form the micrograph and generate characteristic X-ray signals for chemical information. The electrons that pass through the sample and get scattered at high angles are detected by a high-angle annular dark field (HAADF) detector leading to the creation of micrographs where the observed contrast arises from differences in material atomic number (Wang, 2000). This is particularly useful for imaging of supported metal nanoparticles where the atomic number of the metal nanoparticle differs greatly from that of support material and thus resulting in a micrograph where the metal nanoparticles appear significantly brighter compared to those of the support (Niemantsverdriet, 2007; Wang, 2000). In HR-STEM chemical analysis is done via energy-dispersive X-ray spectroscopy (EDX), where emitted characteristic X-rays are collected and analysed to provide information on sample's elemental composition, element distribution and concentration.

3.2.2.1 Experimental details

Transmission Electron Microscopy (TEM) measurements were performed by Mrs Nasheeta Hanief and Mr Richard Martin at the University of Cape Town's Electron Microscope Unit, using FEI F20 CRYO FEGTEM microscope with high performance image 200kV with cryo capabilities, using FEI imaging software. Measurements were performed on all used commercially available ITO support materials and their IrO_x/ITO electrocatalysts counterparts.

High Resolution-Scanning Transmission Microscopy (HR-STEM) measurements were performed by Prof. Patricia Kooyman at the Nelson Mandela Metropolitan University on the selected IrO_x/ITO electrocatalysts using a JEOL JEM ARM200F double Cs-corrected electron microscope, with a field emission gun (FEG) and a HAADF detector, operated at 200 kV which had an Oxford XMax 100 TLE detector for EDX mapping. As IrO_x and support particles are

not necessarily spherical, particle Ferret maximum diameters were measured from recorded micrographs using Image J software to obtain particle size distributions. Normalisation of particle size distribution was achieved by using the measurement of 300 nanoparticles. material.

3.2.3 Brunauer, Emmett and Teller Surface Area analysis

Brunauer, Emmett and Teller (BET) is widely used method for determination of material average specific surface area (in m^2g^{-1}) by means of nitrogen adsorption. The amount of gas that gets adsorbed on the surface of a solid is a function of exposed surface area, temperature, gas pressure as well as strength of interaction between the gas and solid.

To improve the interaction between the solid sample and nitrogen gas, the sample is first cooled with liquid nitrogen after which known quantities of nitrogen gas is released into the sample cell at relative pressures (which creates a partial vacuum). Once saturation pressure is reached, no further adsorption will occur. These changes in relative pressure are measured by highly precise and accurate transducers (Raja & Barron, 2021). The reported measurement is based on nitrogen adsorption isotherms which plot the amount of gas adsorbed as a function of relative pressure. Notably, an inverse correlation between particle size and surface area can be seen. (Bowen, 2002; Walton, 2007).

3.2.3.1 Experimental details

All BET physisorption surface area measurements of the commercially available ITO support materials were performed by Miss. Shene Klink at the University of Cape Town's Analytical Laboratory using a Micromeritics Tristar® II Series instrument which had a range from 0 to 950 mmHg and it was analysed using Micromeritics TriStar II 3020 Version 2.00 software.

3.2.4 Inductively Coupled Plasma- Optical Emission Spectroscopy

Inductively coupled plasma-optical emission spectroscopy (ICP-OES) is a technique that enables elemental analysis of a sample.

First Argon plasma is generated using a quartz torch, after which samples are introduced into the center of the plasma as aerosols. The plasma excites sample atoms and as they are returning to their lower energy states, they emit light that is then focused onto the entrance slit of monochromator (or polychromator), in order to monitor the emission from different elements which are depicted as spectral lines (Olesik, J. W., 1991). Figure 3.3 illustrates the systems that are a part of the ICP-OES instrument.
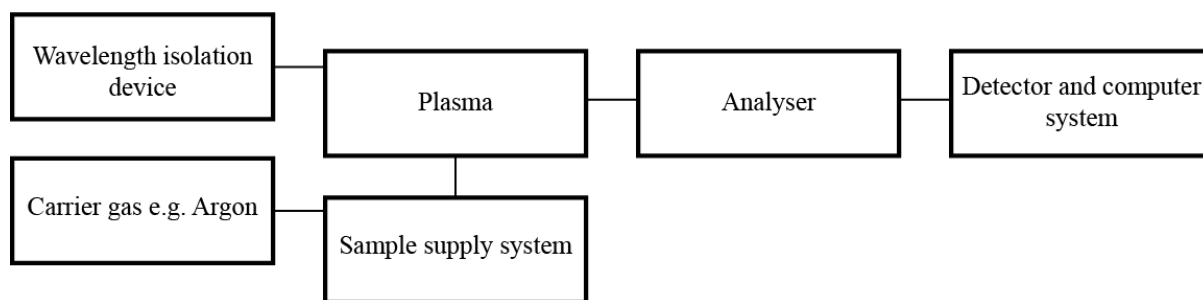
Figure 3.3: Block diagram of a typical ICP-OES instrument.

A major limitation with ICP-OES, is that organic species are not detectable (e.g., C, N, O and H) as molecular species are not strong emitters (Olesik, J. W., 1991). Due to this limitation, only quantitation of metals and not their metallic oxide counterparts can be determined. Thus, in this work only the amount of Sn and In present in the commercially available support materials can be indicated.

3.2.4.1 Experimental details

In this work, Mars 6 Microwave Digester was used to digest the sample and Varian ES 730 ICP-OES to perform ICP-OES measurements. These measurements were performed by the Analytical Team at the University of Cape Town's Analytical Laboratory.

3.2.5 Scanning Electron Microscopy-Energy Dispersive X-ray Spectroscopy

Scanning electron microscopy-energy dispersive X-ray spectroscopy (SEM-EDX) is a technique that enables quantitative elemental analysis for all conductive and vacuum stable samples.

As incident electron beam interacts with the sample's atoms, X-ray signals are generated that are characteristic of the elements within the sample. These X-rays are detected via silicon drift detector and separated in an energy spectrum. Quantitative analysis is achieved either by comparing the intensity (or area) of measured X-ray peaks against those from standard materials or by applying standardless-software based procedures (Niemantsverdriet, 2007).

3.2.5.1 Experimental details

SEM-EDX measurements were used in this work for the quantitation of the elements in the commercial ITO support materials and for the determination of the iridium mass loadings in MOCD IrO_x/ITO electrocatalysts. These measurements were performed by the author, with the assistance of Mrs Nasheeta Hanief at University of Cape Town's Electron Microscope Unit, on FEI Nova NanoSEM 450 operating at 20 kV beam energy and equipped with Oxford X-

Max detector that was used to generate and detect X-rays while INCA Point & ID software was used to obtain X-ray spectra and element quantification.

3.2.6 X-ray Photoelectron Spectroscopy

X-ray photoelectron spectroscopy (XPS) analysis is used to investigate the chemistry at the surface of materials.

This characterisation technique is based on the photoelectric effect. When an incident X-ray beam is irradiated onto the sample (refer to Figure 3.4), its energy is absorbed by the sample atoms, after which core or valance electrons are ejected with particular kinetic energies (E_k) (Niemantsverdriet, 2007). A photoelectron spectrum is recorded by counting number of ejected electrons over a range of kinetic energies. Only photoelectrons generated within the top 2–5 nm-surface layers are able to reach the detector after passing through the energy analyser, which makes this technique very surface sensitive (Che & Ve´drine, 2012; Niemantsverdriet, 2007). More frequently XPS spectrum is plotted using electron binding energies (E_b) that are calculated as a difference between energy of the X-ray source, measured electron E_k and instrument work function. The binding energies and intensities of detected photoelectron peaks enable identification and semi-quantification of elements present at the sample's surface. XPS also provides information about the elemental oxidative states as the peak shapes and binding energy shifts are linked to chemical bonding information within the sample.
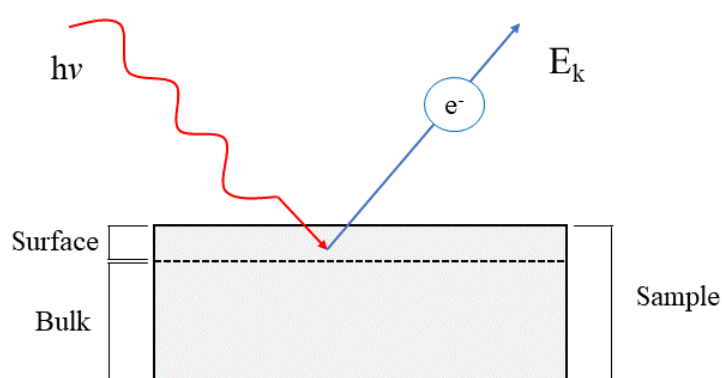
Figure 3.4: Representation of the photoelectric effect experienced by a sample during XPS.

3.2.6.1 Experimental details

In this work, X-ray Photoelectron Spectroscopy (XPS) measurements were performed by Mr Michael CP Wang at the 4D Labs Nanofabrication facility at Simon Fraser University (Canada) on Kratos Analytical Axis Ultra DLD system together with a monochromated Al Kα source

(1486.71 eV). XPSPeak4.1 software was utilised for fitting of the Ir 4f, In 3d, Sn 3d and O 1s components. For all photoelectron peaks a Lorentzian/Gaussian ratio of 20, TS and TL asymmetry factors of 0.2 and 100 were used for curve-fitting of the spectra, unless stated otherwise. For In 3d and Sn 3d spectra an approach similar to the published papers by Detweiler et al. (2019), Donley et al. (2002) and Teterin et al. (2020) was used. For all In 3d and Sn 3d where Sn^{2+} (SnO) and Sn^{4+} (SnO_2) were identified at 486.5 eV and 487.1 eV respectively For Ir 4f spectrum, curve-fitting was done following approach taken by Rajan et al. (2020) which was in agreement with works of Pfeifer et al. (2016) and Yu et al. (2018). Metallic Ir, Ir^{4+} and Ir^{3+} were identified at 60.8 eV, 61.5 eV and 62.4 eV respectively. Where satellite peaks for Ir^{4+} were identified at 62.8 eV and 67.8 eV and for Ir^{3+} at 63.3 eV. The O 1s spectrum, had all oxygen components fitted with a FWHM of 1.38 eV and TS and TL asymmetry factors of 0.1 and 100 were implemented for oxygen bonded to metallic components, while asymmetry factors of 0 and 1 were implemented for oxygen bonded to carbon components.

3.3 Electrochemical Characterisation Techniques

In the following section, the electrochemical characterisation procedure is explained including the preparation of the equipment, testing protocol, and data analysis. The benchmarking of a commercial electrocatalyst that will be compared against in this study is also shown.

3.3.1 General equipment set up

This electrochemical experimental set-up consists of three main components which are the glass cell, electrodes, and electrolyte. The electrolyte solution (that can be neutral, acidic, or alkaline) facilitates the reaction as it is in contact with all the electrodes that are involved. The reference electrode ensures the accuracy of the measurements of the working electrode as it measures the applied potential that is experienced by the catalyst material and as such it must be stable and well-defined in the chosen electrolyte. The working electrode for RDE set-up is usually a glassy carbon disk electrode where it serves as a flat surface to which the catalyst ink (prepared from catalyst powders) can be deposited onto and thus providing an interface at which the reactions can occur from which specific and mass activities can be derived. Counter electrodes that are generally used are Pt wires, foils and meshes which are inert in both HER and OER. Its purpose is to complete the circuit and to not limit the current (which can be achieved by ensuring the counter electrode has a greater surface area than that of the working electrode) to the working electrode. Lastly, a gas inlet is required to ensure saturation of the H_2 or O_2 gas which promotes the equilibrium at standard potential is achieved. The constant

bubbling from the gas inlet into the electrolyte also helps removal any evolved gases that are positioned on electrodes (Fabbri et al., 2014; Wei et al., 2019).
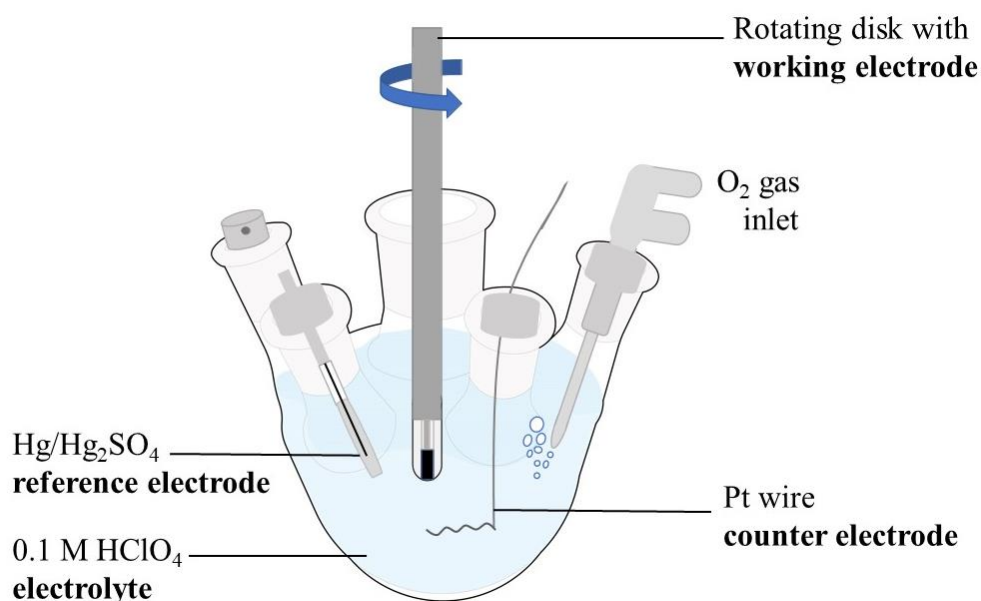
Figure 3.5: Diagram representing a single compartment three-electrode cell using a rotating disk electrode (RDE) set-up.

In this study, the electrochemical tests were performed in a single compartment three-electrode cell (150 mL glass cell, PINE Research), refer to Figure 3.5, using a rotating disk electrode (RDE) set-up (Schmidt, 1998) and a Bio-Logic SP-300 double-channelled potentiostat, equipped with EC-Lab V11.20 software. All electrochemical raw data were generated using the Biologic SP-300 RDE setup utilising EC-Lab V11.20 software and were analysed using Origin 2018 Analysis & Graphing software.

The electrochemical performance of an anode catalyst in a highly oxidative, acidic OER environment was investigated, thus an acidic electrolyte was chosen. This electrolyte was 0.1 M perchloric acid (prepared from 70% $HClO_4$ stock solution, Merck). and as such Hg/Hg_2SO_4 reference electrodes were used as they have stable and well-defined potentials in $HClO_4$ solution. A piece of platinum wire (with a larger surface area than that of the working electrode) was utilised as a counter electrode. Glassy carbon disks (0.196 cm^2) were used at the working electrode as a substrate onto which the catalyst material was deposited.

To encourage removal of O_2 bubbles, the electrochemical RDE set-up was set to rotate the working electrode at 1600 rpm and the whole set-up was tilted by 15–30° to promote the

removal of the evolved O_2 gas bubbles (Fabbri et al., 2014; Garcia & Koper, 2018; Oakton et al., 2017).

3.3.2 Cleaning and calibration

To avoid contamination of any organic and metallic impurities in the electrolyte during electrochemical testing which leads to uncertainties in measurements; all experimental glassware was firstly boiled at 100–120°C in concentrated sulphuric acid solution. After which all the glassware was rinsed 4–5 times with ultrapure 18 MΩ Millipore deionised water to remove the sulphuric acid solution and lastly boiled in ultrapure 18 MΩ Millipore deionised water at 80–100°C. All glassware was stored in ultrapure 18 MΩ Millipore deionised water before use. The platinum wire, used as the counter electrode, was flame sterilised by use of a blow torch, and rinsed with ultrapure 18 MΩ Millipore deionised water before each measurement.

Prior to electrochemical testing, the reference electrodes were calibrated in the 0.1 M $HClO_4$ electrolyte saturated with hydrogen, to ensure that the applied potentials measured are accurate and known against the reversible hydrogen electrode (RHE) (Wei et al., 2019).

3.3.3 Working electrodes preparation

All catalyst inks were prepared by adding together the 10 mg of the catalyst material (either ITO only or IrO_x/ITO supported electrocatalysts) with 4 ml of ethanol, 1 ml of ultrapure 18 MΩ Millipore deionised water and 20 µL of 5wt% Nafion® (Nafion 117, Sigma-Aldrich).

For the commercial benchmark, 10 mg of IrO_2/TiO_2 (Elyst Ir75, Umicore AG & Co. KG) electrocatalyst powder, 1 ml of isopropanol, 4 ml of ultrapure 18 MΩ Millipore deionised water and 20 µL of 5wt% Nafion® (Nafion 117, Sigma-Aldrich) was used.

The inks were ultra-sonicated for 0.5 hr before being magnetically stirred at 400 rpm, and then deposited onto glassy carbon disk surfaces. The ink was collected with a micropipette while undergoing magnetic stirring to ensure well-dispersed ink for deposition onto the surface of the working electrode. The working electrodes' catalyst coated surfaces were prepared for the commercially available ITO support materials and IrO_x/ITO electrocatalysts, by depositing of 40µL of their prepared catalyst ink onto a glassy carbon disk (0.196 cm^2) surface. This resulted in catalyst loading of 400 μg_{cat} cm^{-2}. However, the working electrodes prepared for the IrO_2/TiO_2 (Elyst Ir75) commercial benchmark were prepared were done by depositing of 10 µL of its prepared catalyst ink onto glassy carbon disk surface, which would achieve a catalyst

loading of 100 μg_{cat} cm$^{-.2}$. This difference in catalyst loading was done for the purpose of validating the electrochemical experiment. Lastly, the working electrodes were dried stationary and at room temperature in air.

The reliability of the results was ensured by preparing three working electrodes for each of the catalysts undergoing electrochemical testing and the results were then averaged from the data collected.

3.3.4 Electrochemical testing protocol

The electrochemical testing protocol parameters for both the activity and stability can be summarised into four parts. Table 3.1 indicates the electrochemical techniques used and the purpose of using these electrochemical techniques. The electrochemical testing protocol is an in-house developed protocol which was utilised in the study by Rajan et al. (2020). The protocol used for activity testing, refer to Table 3.1, was *(No. 1–3)*, while for stability testing was *(No. 4)*, with the addition of repetition of activity testing *(No. 1–3)* before and after.

Table 3.1: Electrochemical testing protocol parameter table.

Step No.	Electrochemical Techniques	Parameter settings	Purpose
1	CV	1–1.4 V vs. RHE; 10 mV s^{-1}; 10 cycles 1–1.4 V vs. RHE; 50 mV s^{-1}; 10 cycles	To remove surface contaminants and activate the catalyst layer.
2	CA & CV	1.4 –1.48 V vs. RHE; 4 steps; 1 min hold per step 1.5–1.56 V vs. RHE; 4 steps; 1 min hold per step 1–1.6 V vs. RHE; 50 mV s^{-1}; 10 cycles	Further activation of the catalyst layer; OER window where activity measurements are determined.
3	EIS	1 V vs. RHE; 200 kHz to 100 mHz	Measuring of effective ohmic resistance seen between working electrode and counter electrode.
4	CA	1.6 V vs. RHE; 2 hr hold	The relative OER mass-specific activity loss experienced after expose of the catalyst layer to harsh oxidising environment (i.e., 1.6 V).

To determine the activity (performance descriptor) of electrocatalysts, ohmic correction is required in order to know the true applied potential that was experienced by the electrocatalyst.

This ohmic correction is done by the substraction of 'iR', which is the product of observed current 'i' and the uncompensated resistance 'R' from the measured potential. The 'R' can be determined by electrochemical impedance spectroscopy or current-interrupt methods. To further ensure reliable measurements the reduction of background current or capacitive currents is necessary. This can be done by measuring activity from chronoamperometry (CA) instead of cyclic voltammetry (CV) measurements (Fabbri et al., 2014; Wei et al., 2019).

To avoid the overestimation of the OER activity measurements, the reduction of the effect of transient capacitive currents is necessary. This can be done by only deriving the OER activity values from the latter half of a CA measurement as it is assumed that the produced current there is affected predominately by OER reaction kinetics (Fabbri et al., 2014; Rajan et al., 2020). It is also important to benchmark or validate electrochemical experiment to ensure accuracy and reliability of the obtained results. This can be done by comparison of results to a known standard or benchmark electrocatalyst.

3.3.5 Electrochemical performance data analysis and correction

The *ex-situ* OER mass-specific activities determined in this study were reported at 'E-iR' or iR-corrected OER potential of 1.525 V vs. RHE, which were extrapolated from the Tafel slopes. Tafel slope plots were drawn from the averaging of these various values from the three different runs of each electrocatalyst. The various values or plotted points were determined from CA measurements of each run, in the 1.5–1.56 V vs. RHE range.

To reduce the contribution of the transient capacitive currents, values only produced in the 2nd half (30 seconds) of the individual CA measurements, were used in the determination of OER activity and stability (Fabbri et al., 2014; Rajan et al., 2020).

Mass-specific OER data were obtained by normalisation of the data, with regards to iridium mass present on the working electrode. This mass was calculated using the iridium mass loading (wt.%) determined by EDX measurements. The correction of the OER potentials were determined by from EIS measurements and were found to be in the range of 20–35 Ω value (dependent on the catalyst tested).

3.3.6 Benchmarking

A commercial IrO$_2$/TiO$_2$ electrocatalyst (Elyst Ir75, Umicore AG & Co. KG) which had 75 wt.% iridium mass loading, was used to validate to ensure reliable results are achieved by the electrochemical set-up and protocol as well as for comparison of results to the prepared

IrO$_x$/ITO electrocatalysts. The working electrode for this experiment was prepared to have a catalyst loading of 100 μg$_{cat}$ cm^{-2} as similar loadings of the same commercial benchmark were reported in literature (Oakton et al., 2017; Rajan et al., 2020).

The commercial benchmark was analysed using the Tafel slope analysis Figure 3.6 a) below exhibited the Tafel slopes obtained from activities obtained before and after stability testing. The *ex-situ* OER mass-specific activities before and after the stability test were reported at 1.525 V vs. RHE (iR-corrected) were extrapolated from the Tafel slopes (Figure 3.6 b)).
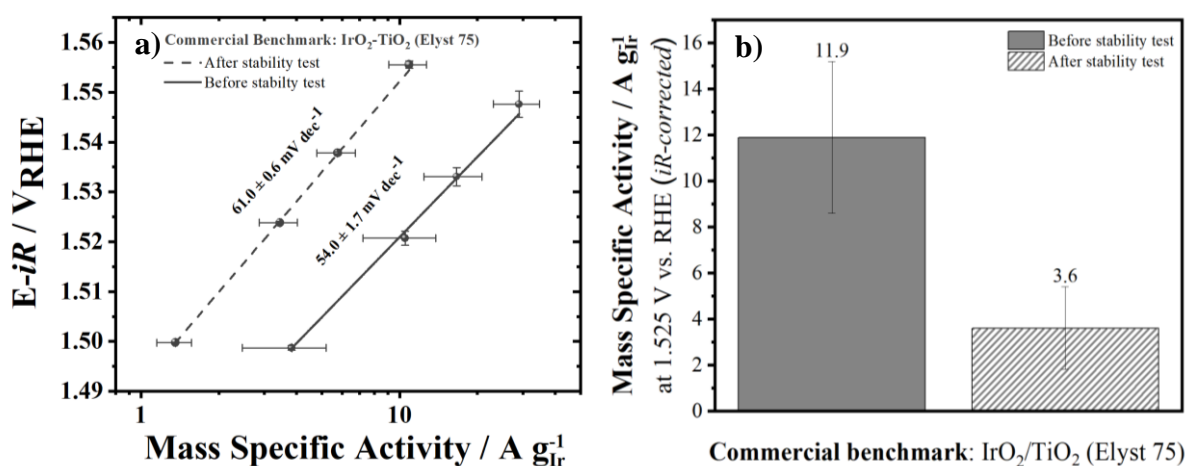
Figure 3.6: **a)** Mass specific Tafel plots for IrO$_2$/TiO$_2$ commercial benchmark (Elyst 75), where the initial mass specific OER activity (solid line) and mass specific activity after stability testing (dashed line). **b)** Mass specific OER activity of commercial benchmark at 1.525 V vs. RHE (iR-corrected), before (solid bar) and after (pattern bar) stability testing by chronoamperometry.

The results achieved for this IrO$_2$/TiO$_2$ commercial electrocatalyst for initial mass specific OER activity was 4.1 $\pm$ 1.4 A g$_{Ir}^{-1}$, 11.9 $\pm$ 3.3 A g$_{Ir}^{-1}$ and 14.8 $\pm$ 4.2 A g$_{Ir}^{-1}$ at 1.5 V, 1.525 V and 1.53 vs. RHE (iR-corrected), respectively. The initial Tafel slope value was found to be 54.0 $\pm$ 1.7 mV dec^{-1}. These values were similar to those values obtained in literature for the same commercial electrocatalyst at their respective reported potentials (Hartig-Weiss et al., 2020; Oakton et al., 2017; Rajan et al., 2020; Spöri et al., 2019).

CHAPTER 4: TIN-DOPED INDIUM OXIDE SUPPORTS

The properties of the commercially available tin-doped indium oxide support materials were evaluated by physical and electrochemical characterisation. The naming convention for the commercially available ITO supports is also presented.

4.1 Naming convention of the supports

Four different commercial ITO supports were used in this study. Table 4.1 provides information regarding sample identification of the commercially available ITO supports used throughout this study and their physicochemical properties specified by the supplier.

Table 4.1: Naming convention for the various commercially available ITO supports used in this study and information provided by the supplier.

Sample ID	Nanopowder colour	$In_2O_3:SnO_2$ ratio (wt.%) [1]	Average particle size (nm) [2]
ITO-A	Blue	95:5	18
ITO-B	Yellow	95:5	20–70
ITO-C	Blue	90:10	18
ITO-D	Yellow	90:10	20–70

[1]Determined by inductively coupled plasma-atomic emission spectroscopy (ICP-AES).

[2]Measured by Transmission Electron Microscopy (TEM).

The supports differ by the amount of Sn dopant and average particle size. It is noted that blue nanopowder supports have similar average particle size but different amount of Sn likewise with the yellow nanopowder.

Nanopowder colour is related to the synthesis conditions of the ITO, where a colour change can be seen for ITO in a partially reductive environment from yellowish-white to blue and in highly reductive environment to a metallic grey (Guenther et al., 2008). And as such blue ITO would be considered as the partially reduced form of the yellow ITO.

4.2 Physical characterisation of the ITO support

4.2.1 Elemental analysis

The elemental composition of the commercially available ITO support materials was evaluated in-house via inductively coupled plasma-optical emission spectroscopy (ICP-OES) and scanning electron microscopy-energy dispersive X-ray spectroscopy (SEM-EDX) (Table 4.2).

Table 4.2: Comparison of bulk elemental composition of the commercially available ITO support materials.

Sample I.D.	ICP-OES measurements (with standard deviation)		SEM-EDX measurements (with standard deviation)	
	In (wt.%)	Sn (wt.%)	In (wt.%)	Sn (wt.%)
ITO-A	95.0 ± 0.5	5.0 ± 0.1	94.0 ± 2.3	6.0 ± 1.8
ITO-B	95.0 ± 0.4	5.0 ± 0.1	95.0 ± 1.7	5.0 ± 1.5
ITO-C	90.0 ± 0.4	10.0 ± 0.1	90.0 ± 1.7	10.0 ± 1.4
ITO-D	90.0 ± 0.1	10.0 ± 0.1	90.0 ± 1.8	10.0 ± 1.5

*ICP-OES quantification error of measurement is $\pm 0.2\%$ of the relative concentration (Olesik, J.W., 2020). EDX quantification error of measurement for these elements (In and Sn) is from 0.1–0.2 wt% (GlobalSino, 2020).

It is evident that internally taken measurements are in excellent agreement with the data provided by the supplier (Table 4.1) for all ITO support materials. The measured ICP-OES results were seen to be reliable and showed a good correlation with average $R^2 = 0.9997$ to the standards. The presented EDX results are based upon averaging of three readings.

4.2.2 Structural studies

The structural characterisation for all ITO supports was done via X-ray diffraction (XRD). Figure 4.1 shows the X-ray diffractograms of the four commercial ITO supports parallel to each other with matched diffraction pattern reference lines. The X-ray diffraction patterns are shown for the diffraction angle (2θ) range of 20 to 80˚.

All ITO support materials were identified as that of the body-centered cubic structure of In_2O_3 (PDF 00-044-1087) without any distinguishable peaks for SnO_2 as an additional phase from the X-ray diffractograms. This is also supported by the absence of the most intense peaks at

26.5° for SnO$_2$ and 33.2° for SnO, as indicated in Figure 4.1 by the purple and grey dotted lines respectively (Senthilkumar, Senthil & Vickraman, 2012).This result indicates the formation of ITO phase rather than a mixture of In$_2$O$_3$ and SnO$_2$. The successful incorporation of SnO$_2$ into the In$_2$O$_3$ host lattice is known to lead to high electronic conductivity due to generation of conducting carrier-oxygen vacancies (Ayeshamariama et al., 2014; Puthiyapura et al., 2014b). However, the presence of amorphous SnO$_2$ which is not detectable by XRD due to detection limit of 3 nm cannot be excluded.
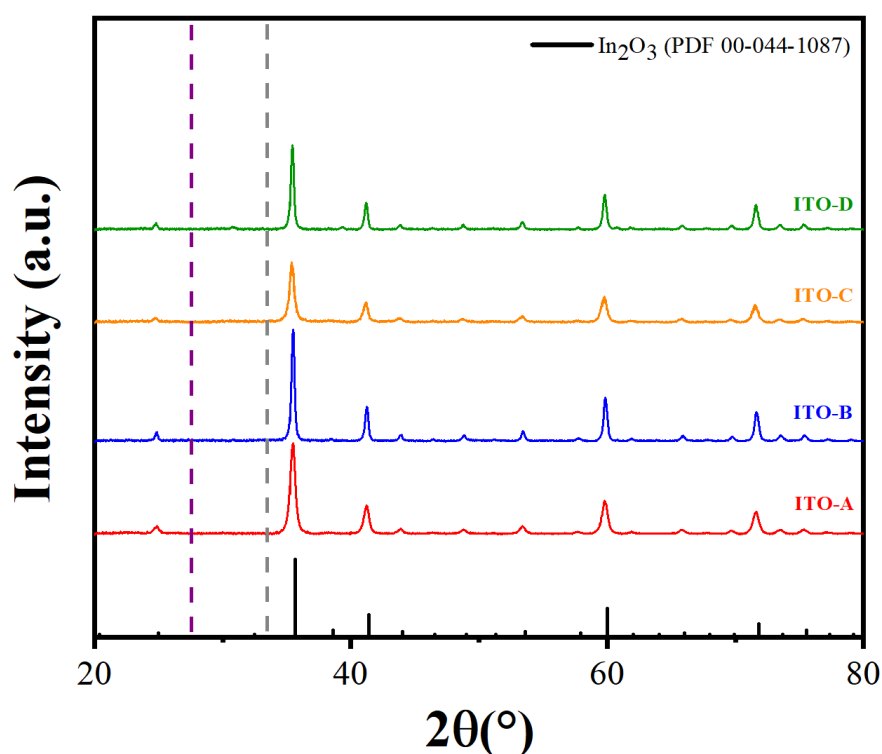
Figure 4.1: X-ray diffractograms of the commercial ITO supports investigated in this study, where the position of the expected prominent peaks for SnO$_2$ and SnO are indicated by purple and grey dotted lines, respectively.

The crystallite sizes of the ITO supports were calculated from the full width at half maximum (FWHM) of the most intense diffraction peak corresponding to (2 2 2) lattice plane (peak position at 35°) using Scherrer's equation (Table 4.3).

The FWHM measurements from respective X-ray diffractograms showed a good correlation with average R^2 = 0.9785. The results show that smaller crystallite sizes are obtained for ITO-A and ITO-C compared to ITO-B and ITO-D.

Table 4.3: The FWHM and estimated crystallite size of the ITO supports determined via Scherrer's equation.

Sample I.D.	FWHM (θ) (with standard deviation)	Estimated crystallite size (nm)
ITO-A	0.5±0.2	18.6
ITO-B	0.3 ±0.1	31.9
ITO-C	0.5 ±0.2	17.2
ITO-D	0.3 ± 0.1	30.9

*XRD error of measurement for fitting of profile (2θ and FWHM) should be < 10% (Speakman, 2021).

4.2.3 Microstructure of the ITO supports

The representative Transmission Electron Microscopy (TEM) micrographs of the ITO support materials are shown in Figure 4.2. These micrographs showed that the nanoparticles of all the ITO support materials were irregularly shaped. It is also evident that ITO-A and ITO-C have smaller particles compared to ITO-B and ITO-D, which is in agreement with information provided by the supplier. This would also be consistent with materials having varying surface areas as well.
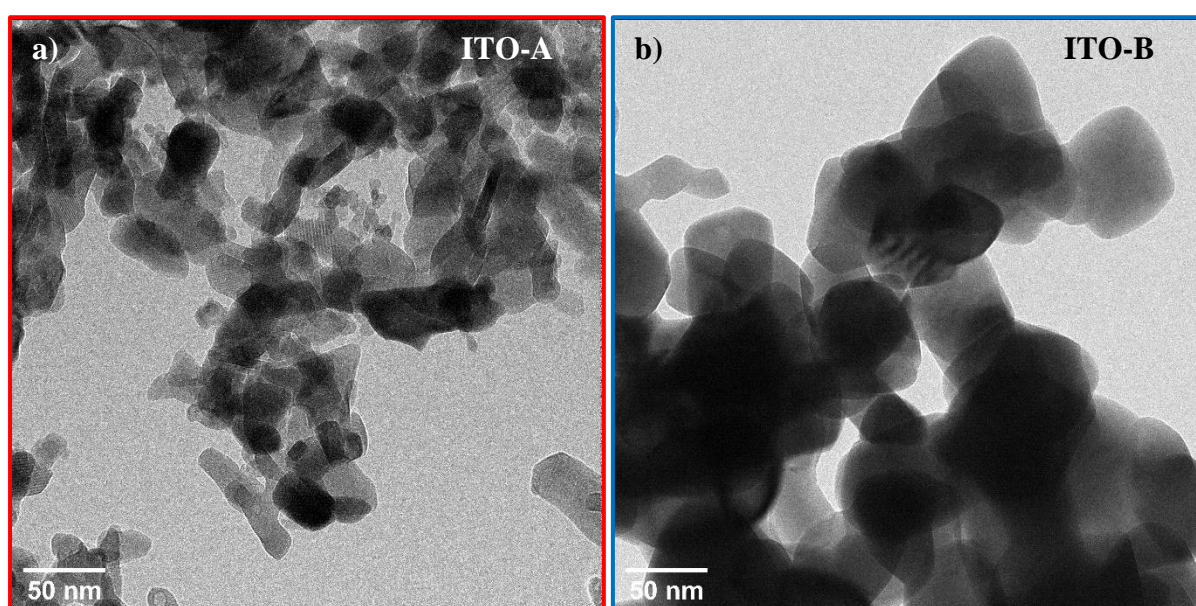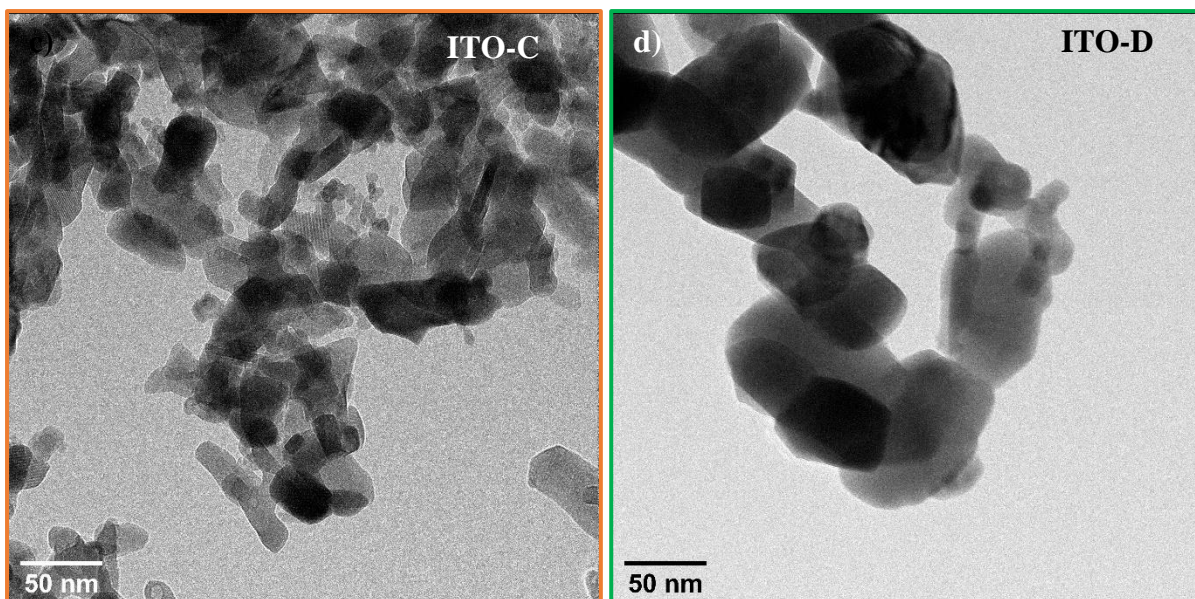
Figure 4.2:TEM micrographs **(a-d)** representative of ITO-A, ITO-B, ITO-C and ITO-D, respectively.

From TEM micrographs, Ferret maximum was measured typically for 300 nanoparticles to generate particle size distribution histograms. Figure 4.3 shows measured particle size distribution histograms for ITO supports and the average particle diameter values which are referred to as "particle size". ITO-A and ITO-C, seen in Figure 4.3 (a & c) have a uniform size distribution of the particles which can be seen by the 'curve' of the frequency polygon, and both have a frequency maximum at ~14 nm. ITO-B and ITO-D, shown in Figure 4.3 (b & d) have much broader distributions with higher contributions from larger particles (irregular shape of the frequency polygon and larger standard deviation of the nanoparticles). The frequency maxima for ITO-B are at ~50 and 65 nm, however there is a large frequency of particles at ~ 40 nm as well. The shape of ITO-D distribution appears to be bi-modal, indicating two predominant frequency maxima at ~35 and 55 nm.
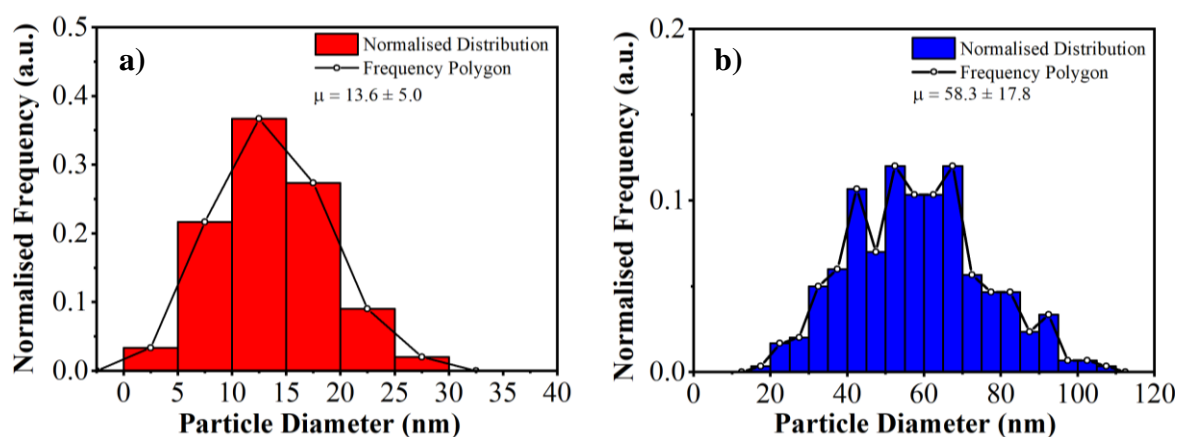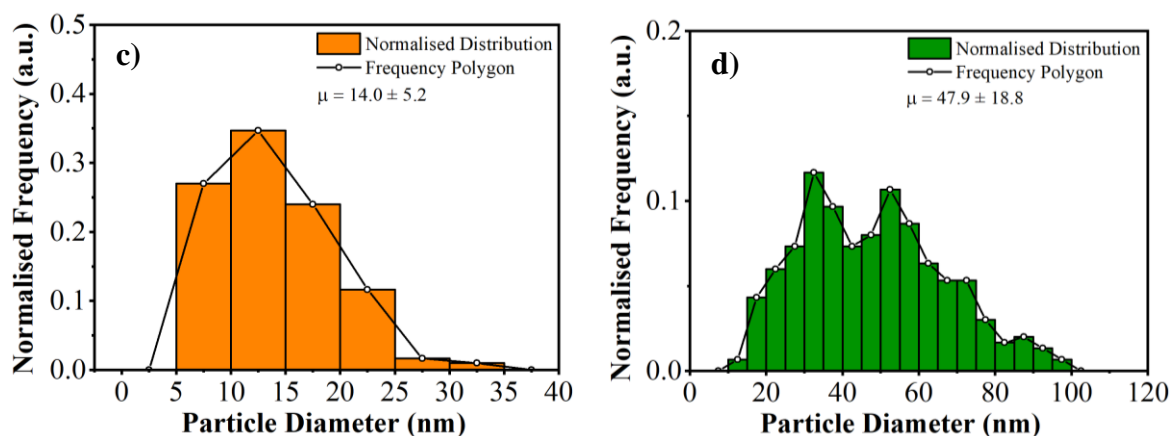
Figure 4.3: Particle size distributions of **a)** ITO-A, **b)** ITO-B, **c)** ITO-C and **d)** ITO-D nanoparticles.

4.2.4 Surface area analysis

The specific surface areas of the ITO support materials were measured by using the Bruaner, Emmett and Teller (BET) surface area analysis. Surface area and particle size have an inverse relationship, i.e. high surface area is obtained from samples with small particle sizes. Therefore ITO-A and ITO-C, display a surface area that is about three times larger compared to that of ITO-B and ITO-D (refer to Table 4.4).

Table 4.4: Average TEM nanoparticle sizes and BET surface area of the commercially available ITO support materials.

Sample I.D.	Average TEM particle size (nm)	Average BET surface area ($m^2 g^{-1}$)[1]
ITO-A	13.6 ± 5.0	29.0
ITO-B	58.3 ± 17.8	10.0
ITO-C	14.1 ± 5.2	32.0
ITO-D	47.9 ± 18.8	10.0

*TEM error of measurement of particle diameter ranges from 2–8% (Verleysen et al., 2019).
BET error of measurement is $\leq 3\%$ for surface areas ≥ 10 m^2 (Bosch & Peppelenbos, 1977).

4.2.5 Chemical stability of the ITO supports

According to the Pourbaix diagram (Pourbaix, 1974), ITO is expected to be unstable due to the dissolution of its host lattice (In_2O_3) in acidic electrolytes (pH=1) at all potentials. However, as Benck et al. (2014) determined that ITO was electrochemically inert for potential range from -0.46 V to 2.15 V vs. RHE in an acidic electrolyte (pH=1). Therefore, it was concluded that any ITO instability will be the consequence of chemical dissolution rather than electrochemical activity. As such in the following section, the chemical dissolution of the ITO supports is investigated.

The chemical stability of the commercial ITO supports was evaluated by a time-based chemical dissolution of the material in the 0.1 M $HClO_4$ electrolyte. Quantitative analysis of the composition was performed from supernatant samples and determined via ICP-OES analysis.

Two different commercial ITO supports, ITO-A and ITO-B, which varied in colour, particle size and BET surface area (refer to Table 4.1) were used as representative samples for the chemical stability testing. Figure 4.4 shows the chemical dissolution profiles over a period of 24 hr, while Table 4.5 summarises calculated percentage of dissolution.
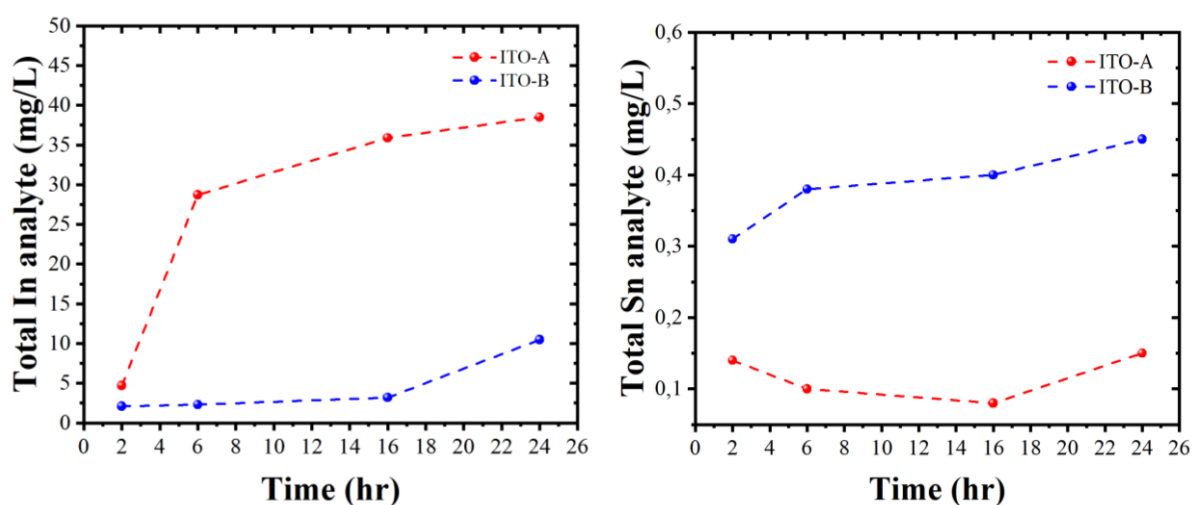
Figure 4.4: Chemical dissolution of ITO-A and ITO-B.: **a)** total analyte (mg/L) present in the supernatants over a 24 hour period and **b)** total Sn analyte (mg/L) present in the supernatants over a 24 hour period is shown.

Table 4.5: Quantitative analysis of the dissolved In and Sn from ITO-A and ITO-B during the chemical stability test.

Time (hr)	Sample I.D.			
	ITO-A		ITO-B	
	In dissolution (%)	Sn dissolution (%)	In dissolution (%)	Sn dissolution (%)
2	11	4	5	8
6	69	3	6	10
16	87	2	8	10
24	93	4	25	11

*ICP-OES quantification error of measurement is ± 0.2% of the relative concentration (Olesik, J.W., 2020).

It is evident that ITO-A is significantly more chemically unstable compared to ITO-B. A rapid increase in In concentration in a supernatant solution is observed for first 2–6 hours of stability test for ITO-A indicating that during this time this support loses ~69% of In compared to only 6% for ITO-B. In contrast, low amounts of dissolved Sn were seen for both ITO supports (Figure 5.4).

Therefore, the yellow-coloured, low BET surface area ITO support was more stable compared to the blue-coloured and high BET surface area ITO. This may be due to the different In and Sn species being present on the surface of the support particles, as the blue-coloured ITO is the partially reduced form of the yellow-coloured ITO. However, to confirm this, further investigation into the nature of the ITO supports with XPS would be recommended.

4.3 Electrochemical stability of the ITO support

The electrochemical stability of the commercially available ITO support material was examined by applying the same stability testing protocol that was established for electrocatalysts (*Chapter 3*, *Section 3.3.4*). The average observed charge during the stability test for the ITO support was calculated by the area under the chronoamperometry graph i.e. by the multiplication of the average current (from three readings) with length of time for stability test (7 200 seconds). The complete dissolution charge for Sn^{2+} and In^{3+} was determined with approximated mass of Sn or In present in the ITO support material deposited onto the working

electrode's surface. The following equation was used to calculate the dissolution charge for Sn^{2+} and In^{3+}:

$$\frac{mass\ of\ element\ present\ on\ electrode}{Mr\ of\ element} \times number\ of\ moles\ of\ electrons \times 96\ 485\ C\ (Faraday's\ constant)\ (4)$$

Table 4.6 shows the average observed charge experienced during the stability testing and lists the calculated dissolution charges for In and Sn in all ITO supports.

Table 4.6: Charge analysis of the stability CA step for the commercially available ITO support materials.

Sample I.D.	Average observed charge at applied potential of 1.6 V (C)	Calculated dissolution charge for Sn^{2+} (C)	Calculated dissolution charge for In^{3+} (C)
ITO-A	0.10 ±0.06	6.50×10^{-6}	1.82×10^{-4}
ITO-B	0.52 ± 0.62	6.50×10^{-6}	1.82×10^{-4}
ITO-C	0.11 ± 0.13	1.30×10^{-5}	1.92×10^{-4}
ITO-D	0.05 ± 0.03	1.30×10^{-5}	1.92×10^{-4}

ITO-B had the highest observed charge of all ITO support materials. The values for the blue-coloured, small particle sized ITO support materials (ITO-A and ITO-C) were similar. Overall, it was noted that ITO supports displayed low current responses (refer to Figure 4.5) This is due to ITO being electrochemically inert in the tested OER potential window of -0.46 V to 2.15 V vs. RHE in an acidic environment (Benck et al., 2014). The observed charges are significantly higher than calculated dissolution charges, possibly due to the good electronic conductivity of ITO. Blue-coloured ITO support is expected to have a higher electronic conductivity compared to the yellow-coloured ITO support (Guenther et al., 2008). However, as ITO was shown to undergo chemical dissolution in the $HClO_4$ electrolyte used in this study (refer to *Section 4.2.5*), this could possibly be the reason for the decrease in the observed charge seen in ITO-B and ITO-C compared to ITO-A.
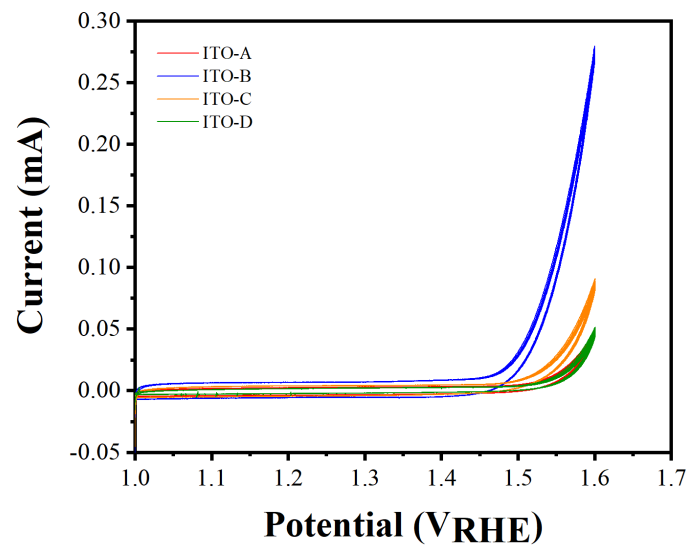
Figure 4.5: Representation of the cyclic voltammograms (CVs) seen for each of the ITO supports at the end of the stability testing protocol.

CHAPTER 5: IRIDIUM-BASED SUPPORTED ELECTROCATALYSTS – PHYSICOCHEMICAL PROPERTIES

This chapter summarises the results of the physical characterisation of the IrO$_x$/ITO supported electrocatalysts prepared by the Metal-organic Chemical Deposition technique. Focus was placed on the physical characterisation by Transmission Electron Microscopy and X-ray photoelectron spectroscopy which was performed on all the prepared supported electrocatalysts to gain an understanding of the particle size, distribution, nature and composition of the catayltic nanoparticles present on the surface of the IrO$_x$/ITO electrocatalysts.

5.1 Iridium loading of the electrocatalysts

Iridium loading of the prepared IrO$_x$/ITO supported electrocatalysts was determined via SEM-EDX analysis. The naming convention used for the prepared electrocatalysts corresponds to the ITO support materials discussed in *Chapter 4* and is summarised in Table 5.1.

Table 5.1: The sample identification of the prepared IrO$_x$/ITO supported electrocatalysts and their achieved Ir loadings.

Catalyst sample ID	Ir loading (wt.%) (with standard deviation)	ITO support used
CAT-A	8.0 ± 0.4	ITO-A
CAT-B	11.0 ± 0.8	ITO-B
CAT-C	12.0 ± 0.5	ITO-C
CAT-D	11.0± 0.9	ITO-D

*EDX quantification error of measurement for this element (Ir) is 0.1-0.2 wt% (GlobalSino, 2020).

For the IrO$_x$ deposition, a nominal iridium loading of 20 wt.% was aimed, however the SEM-EDX measurements confirmed that values between 8–12 wt.% were achieved. This reduction in actual vs. targeted iridium loading was also observed in the application of the MOCD technique with ATO support. Such discrepancy is a consequence of the incomplete transfer of Ir species from the precursor to the ITO support. In the early stage of the deposition process, Ir(acac)$_3$ which is mixed with the ITO support, starts to vaporise at ~ 200 °C, and forms a thin

coating on the reactor walls. As a result, the amount of the precursor that remains in contact with the support is lesser compared to the beginning of the process. When the reactor reaches precursor decomposition temperatures of 250–350 °C, IrO_x nanoparticles form on the support, leading to the catalyst with a loading lower than targeted (Music´ et al., 2003; Rajan et al., 2020).

5.2 Structural studies

The structural characterisation of the prepared electrocatalysts was determined from X-ray diffractograms. Figure 5.1 illustrates diffractograms measured from four prepared electrocatalysts (represented in polychromatic lines). A representative example of an X-ray diffractogram of the commercially available ITO support, previously discussed in *Chapter 4* (represented in grey-coloured line) was also presented.
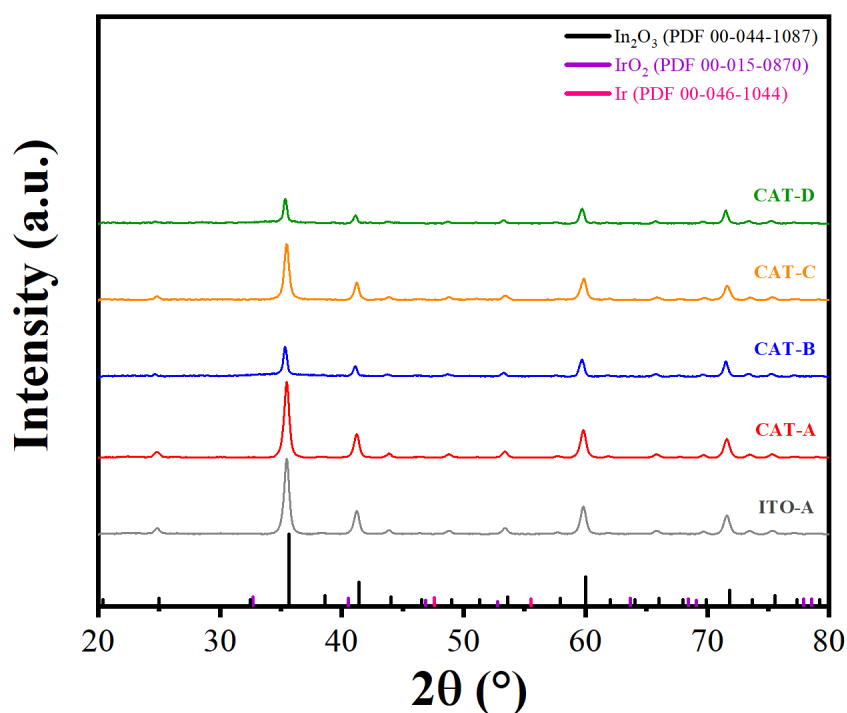
Figure 5.1: X-ray diffractograms of the prepared IrO_x /ITO electrocatalysts investigated in this study.

A decrease in intensity seen in the XRD patterns of the prepared electrocatalysts was possibly a result of the limited quantity of the electrocatalysts available for measurement compared to that of the ITO support material. All prepared electrocatalysts had no distinguishable peaks displayed on the XRD patterns for the identification of the Ir metal and IrO_2. This could be explained with the low loading of iridium on the ITO support material, small particle size of

the IrO$_x$ nanoparticles (below the detection limit of 3 nm) and possible masking of the IrO$_x$ peaks by In$_2$O$_3$ pattern.

5.3 Microstructure of the deposited catalyst

The microstructure of IrO$_x$ catalytic nanoparticles on the ITO support was evaluated from the TEM micrographs. Figure 5.2 displays the dispersion and particle size of the deposited catalyst on the commercial ITO supports, while Figure 5.3 provides a close-up look into IrO$_x$ arrangement in CAT-A and B.
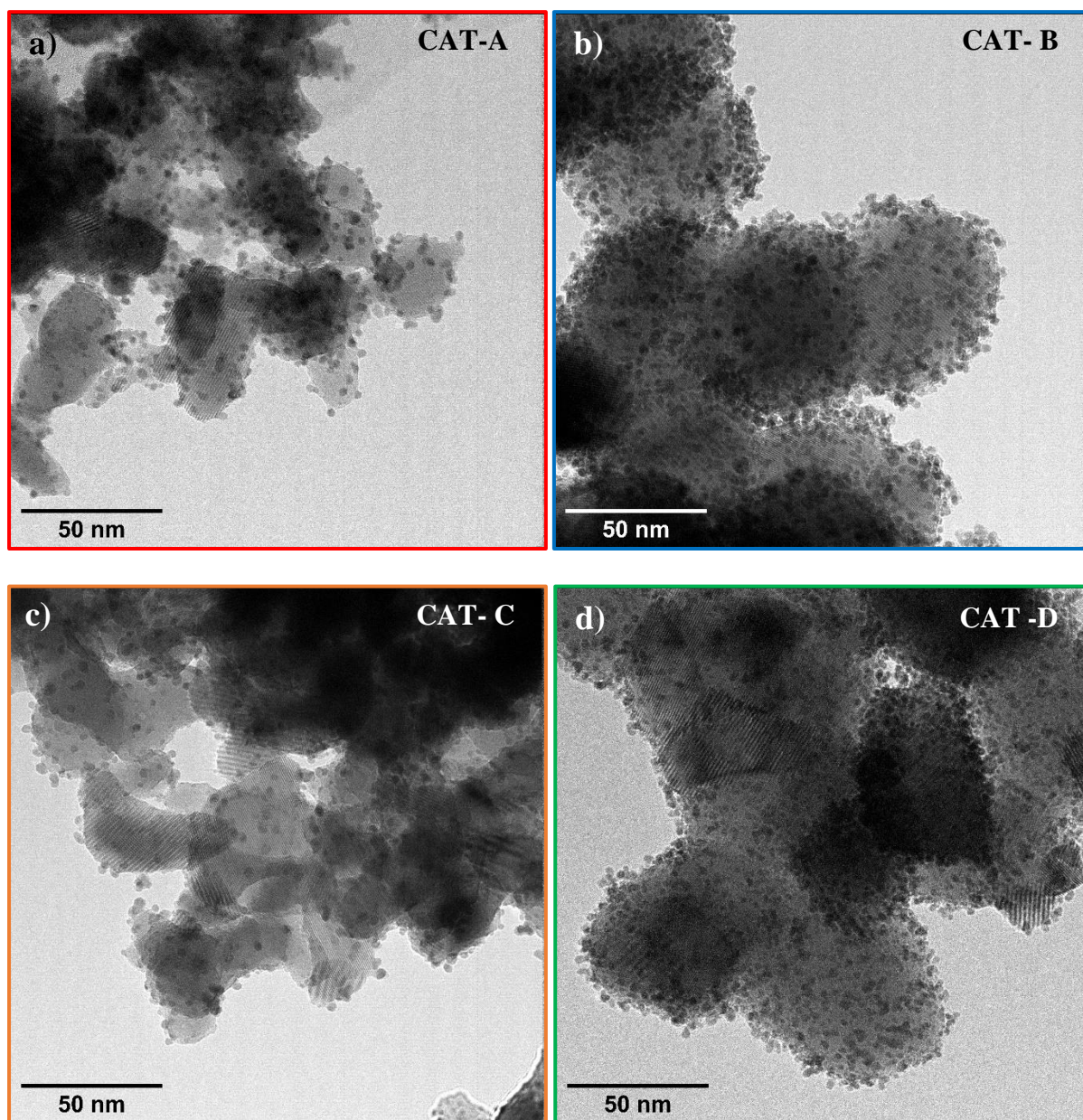
Figure 5.2: TEM micrographs of the prepared IrO$_x$/ ITO electrocatalysts of **a)** CAT-A. **b)** CAT-B, **c)** CAT-C and **d)** CAT-D.

All electrocatalysts have uniformly dispersed IrO_x catalytic nanoparticles, however the coverage differs between the low and high BET surface area ITO supports. The IrO_x catalytic nanoparticles coverage is greater for CAT-B and CAT-D where low BET surface area ITO support (10 m^2g^{-1}) was used. Whereas lower coverage is exhibited by CAT-A and CAT-C which utilise high BET surface area ITO support (29–32 m^2g^{-1}). Notably these variations cannot be assigned to differences in Ir loadings as all electrocatalysts have similar Ir amounts (Table 5.1). Taking this into consideration, an inverse relationship is then observed between the BET surface area of the support and IrO_x catalytic nanoparticles coverage over the support.
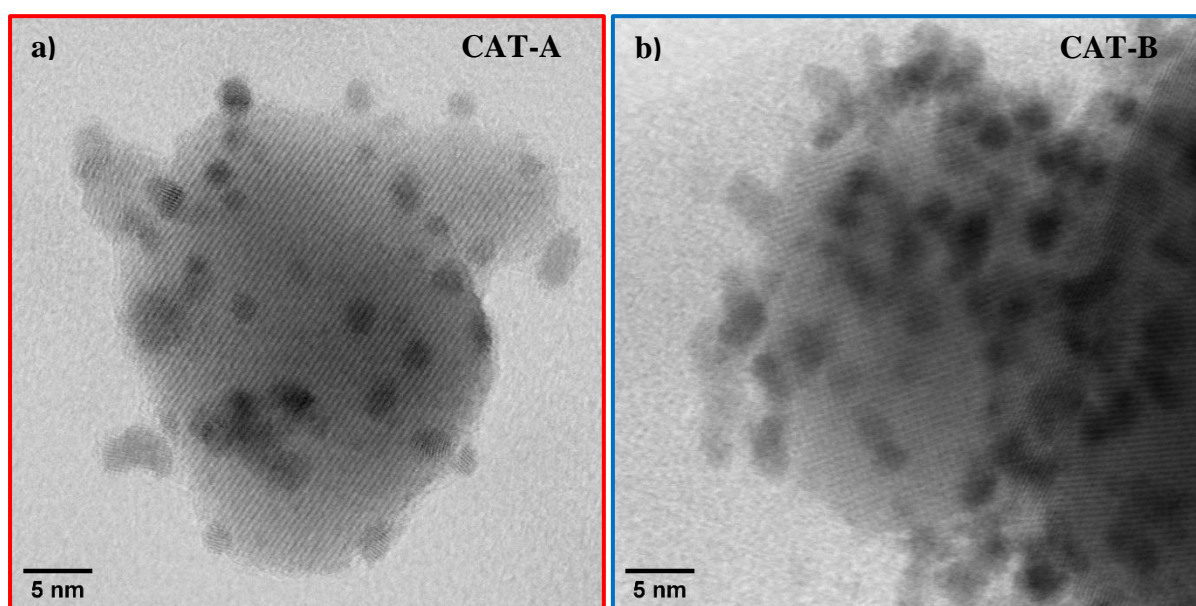
Figure 5.3: High magnification of the HR-STEM micrographs of **a**) CAT-A and **b**) CAT-B.

The IrO_x particle size distribution was determined for all electrocatalysts (refer to Figure 5.4) CAT-A, B and C have similar frequency distributions with frequency maxima of ~2.2 nm, while CAT-D also has a frequency maximum of ~2.2 nm, it has less contribution to its frequency distributions from particles bigger than 3 nm. All electrocatalysts had an average particle size in the range of 2.1–2.4 nm.
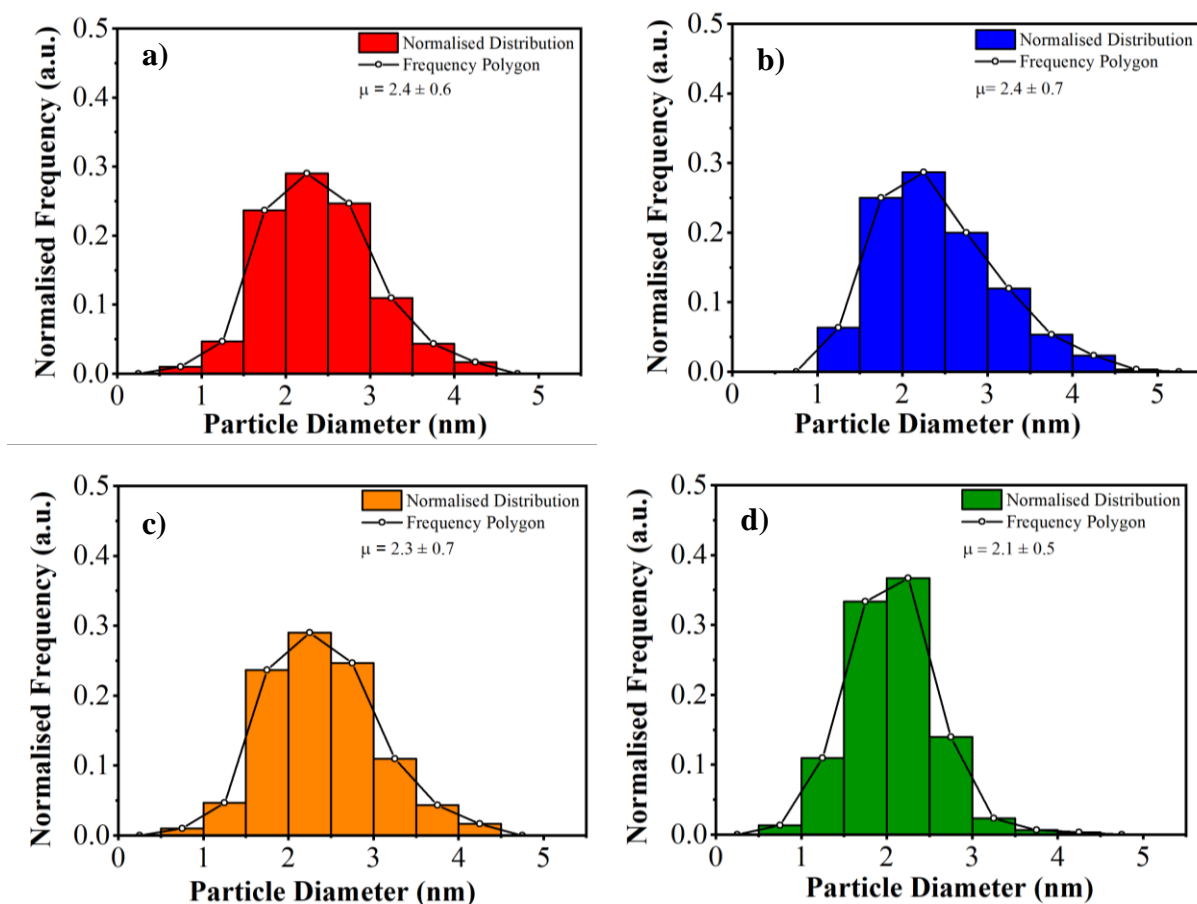
Figure 5.4: Particle size distributions of the IrO$_x$ catalytic nanoparticles of **a)** CAT-A, **b)** CAT-B, **c)** CAT-C and **d)** CAT-D.

It can also be concluded that the MOCD deposition of IrO$_x$ on ITO resulted in a similar average particle size as previously demonstrated for IrO$_x$ on ATO (Rajan et al., 2020).

Figure 5.5 shows distribution and composition of electrocatalyst components in CAT-A. This catalyst was chosen for HR-STEM EDX mapping, because of well-dispersed IrO$_x$ catalytic nanoparticles and therefore sufficiently exposed support surface. Elemental maps for In, Sn are recognised to come from the ITO support material while Ir signal is clearly associated with catalytic nanoparticles deposited on to the ITO. The In signal appears stronger compared to that of the Sn signal, which is because of significantly larger In concentration, but also because of limitations of the EDX detector (small window results in low X-ray counts collection in mapping operating mode). As such the colour composite elemental map (refer to Figure 5.5 b)) was compiled using the In and Ir elemental distributions only.
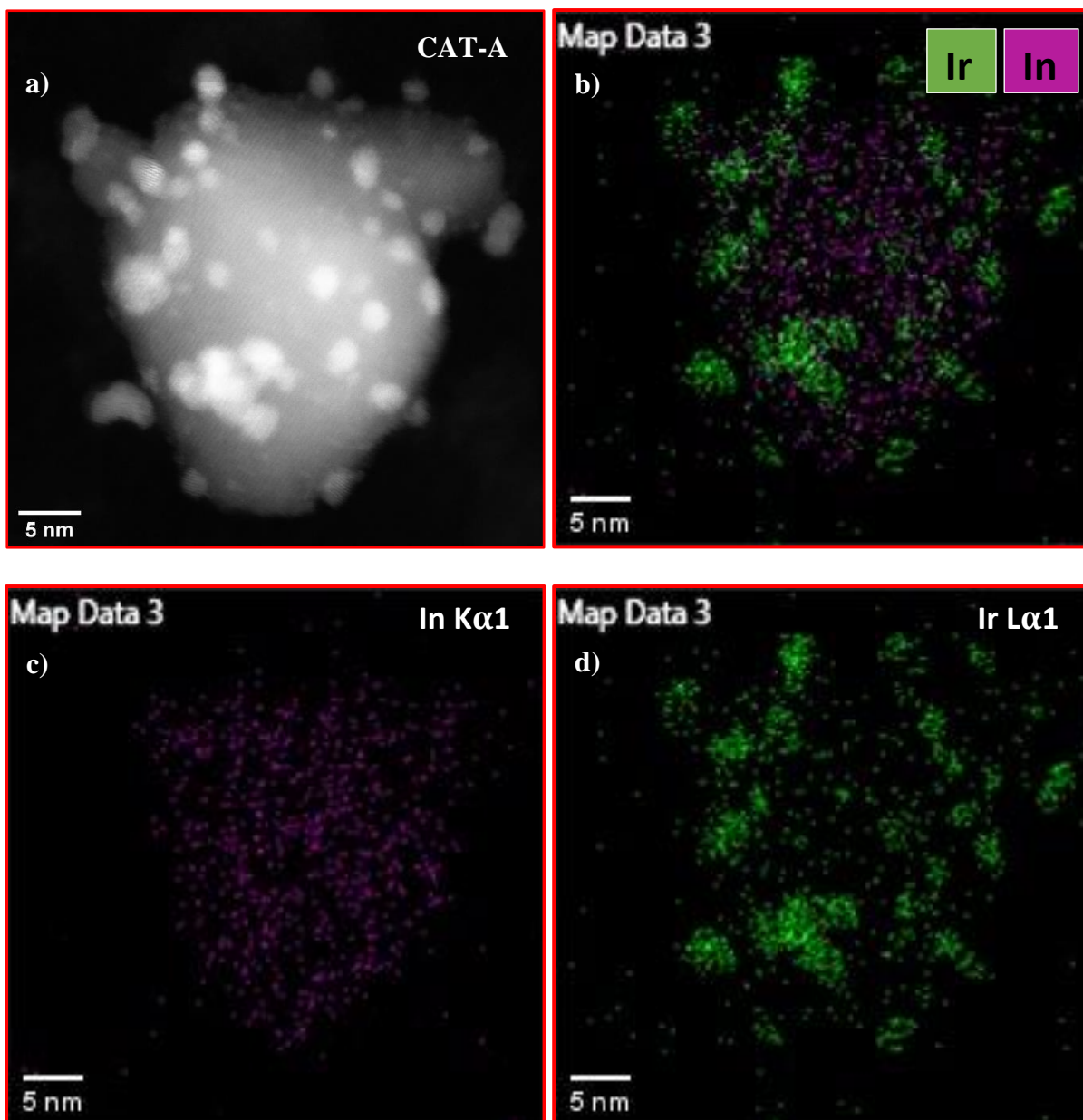
Figure 5.5: HR-STEM EDX maps: **a)** HAADF micrograph for CAT-A, **b)** with corresponding colour composite elemental map showing In and Ir signal distribution, **c)** In signal distribution only and **d)** Ir signal distribution only.

Identification of the Ir species present can be deduced by measuring the visible particle lattice spacings from HR-STEM micrographs. Figure 5.6 shows selected particle used for determination of the lattice spacings. Please refer to *Figure B.1* in *Appendix B* for all the HR-STEM micrographs used for lattice spacing measurement of CAT-A.
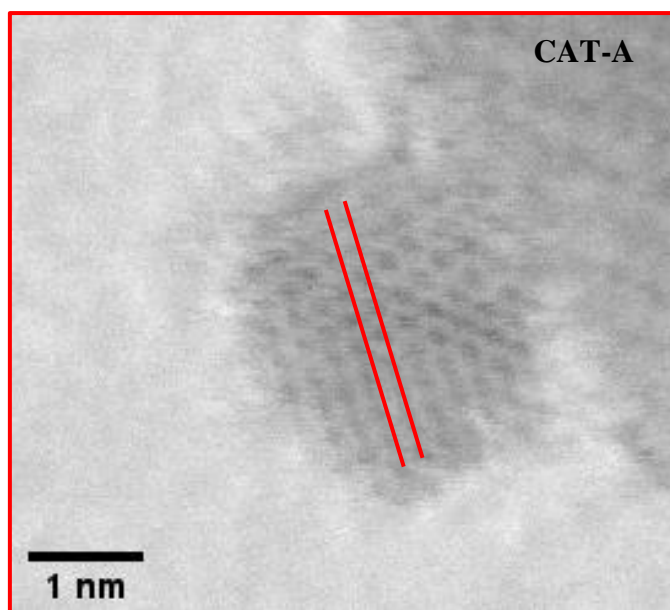
Figure 5.6: HR-STEM micrographs of CAT-A, with IrO_x catalytic nanoparticle used in lattice spacings' measurement indicated.

Lattice spacings which were visible for CAT-A, further confirmed the presence of the cubic Ir metal nanoparticles and rutile tetragonal IrO_2. Measurements were taken from eight IrO_x catalytic nanoparticles, and lattices spacings were compared to the nearest known values for the Ir species (refer to Table 5.2).

Table 5.2: Measured lattice spacings for IrO_x catalytic nanoparticles for CAT-A, with comparison to known cubic Ir metal and tetragonal IrO_2 lattice spacings.

Particle count	Obtained lattice spacings (Å)	Known lattice spacings in cubic Ir metal (Å)	Known lattice spacings in tetragonal IrO_2 (Å)	Probable Ir species observed
1	3.06 ± 0.04	2.22 (111)	3.18 (110)	IrO_2
2	2.23 ± 0.06	2.22 (111)	2.25 (200)	Ir/IrO_2
3	3.22 ± 0.12	2.22 (111)	3.18 (110)	IrO_2
4	3.18 ± 0.10	2.22 (111)	3.18 (110)	IrO_2
5	2.57 ± 0.02	2.22 (111)	2.58 (101)	IrO_2
6	2.23 ± 0.06	2.22 (111)	2.25 (200)	Ir/IrO_2
7	2.19 ± 0.08	2.22 (111)	2.25 (200)	Ir/IrO_2
8	2.97 ± 0.08	2.22 (111)	3.18 (110)	IrO_2

5.4 Nature and composition of the support and deposited catalyst

To gain knowledge on the surface composition and nature of the prepared MOCD IrO_x/ITO electrocatalysts and to determine if and how the support materials (varied In_2O_3: SnO_2 ratios and particle size) influence nature of deposited catalyst, it was necessary to perform XPS measurements on all the electrocatalysts that were investigated in this study. Low resolution XPS survey scans were used for qualitative and quantitative analysis, while high resolution spectra for nature of subcomponents. Element quantification from XPS surface analysis is presented in Table 5.3.

Table 5.3: Quantitative analysis of the electrocatalysts' surface components.

Element / ratio	Sample I.D.							
	CAT-A		CAT-B		CAT-C		CAT-D	
	Atomic concentration (At.%)	Mass concentration (wt.%)	Atomic concentration (At.%)	Mass concentration (wt.%)	Atomic concentration (At.%)	Mass concentration (wt.%)	Atomic concentration (At.%)	Mass concentration (wt.%)
O	25.99	15.19	24.53	15.14	40.62	16.74	35.41	15.31
Sn	1.70	7.36	0.63	2.87	2.79	8.52	1.88	6.03
In	8.14	34.14	4.86	21.53	15.44	45.66	11.25	34.92
C	61.44	26.95	65.68	30.43	37.54	11.61	45.67	14.82
Ir	2.24	15.71	4.00	29.63	3.51	17.38	5.52	28.67
Cl	0.50	0.64	0.30	0.41	0.11	0.10	0.26	0.25
surface Ir/In ratio	0.28	0.46	0.82	1.38	0.23	0.38	0.49	0.82

*Error of measurement for the XPS quantitative analysis is $\pm$ 10% (Smart, 2021).

In terms of atomic surface concentrations, carbon is present between 20–60% in all prepared electrocatalyst. This is due to an adventitious carbon, a common contaminant that occurs at the surface of all samples that have been exposed to ambient atmosphere (Baer & Engelhard, 2010) and/or a carbon remained from the decomposition of Ir metal-organic precursor. Its high contribution to the overall electrocatalyst surface compositions illustrates how surface sensitive XPS technique is. Such as that chlorine, with atomic and mass surface concentration of $<$ 1%,

was detected on the surface of all the electrocatalysts. Its presence can be explained as possible contamination from ITO supports, handling of electrocatalysts and/or by deposition process.

All ITO supports' surface compositions differed from their bulk compositions. The surface composition data of the electrocatalysts indicated that more Sn is present at the electrocatalyst surface relative to In, compared to their bulk Sn/In wt.% ratio (see *Table B.1* in *Appendix B*). However, as only XPS data post-deposition was analysed, it would be recommended to perform an XPS analysis on the ITO supports only to determine if the deposition process may have changed the amount of Sn present on the surface.

It is interesting to explore if any relationship exists between catalyst coverage and the surface Ir/In wt.% ratio. Figure 5.7 illustrates the correlation between the surface Ir/In wt.% ratio measured from the surface of electrocatalysts, and support in-house measured average BET surface area.
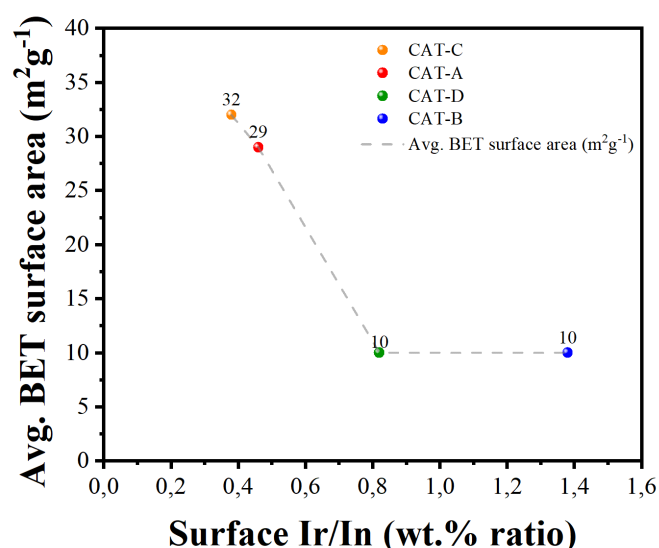
Figure 5.7: Correlation between the electrocatalysts' surface Ir/In wt.% ratio and the ITO supports' average BET surface area.

It is evident that the electrocatalysts with the low BET surface areas (large particle sized) ITO supports, such as CAT-B and CAT-D, have a higher surface Ir/In wt.% ratio compared to those using high BET surface areas (small particle sized) ITO supports. The higher Ir/In surface ratio indicated more Ir species being deposited onto those supports. This is consistent with conclusions drawn from the TEM micrographs (Figure 5.2).

Initial observations and preliminary findings regarding the nature of electrocatalyst surfaces can be deduced from the high resolution XPS raw spectra while curve fitting is necessary for understanding on chemical bonding and to quantify sub-component contributions. Curve fitting of O 1s, Sn 3d, In 3d and Ir 4f spectra were performed in order to obtain an understanding of the nature and composition of the IrO_x nanoparticles and ITO support surface post-deposition.

5.4.1 Analysis of the XPS narrow scans

The preliminary findings of the XPS data are drawn from the Figure 5.8 below.
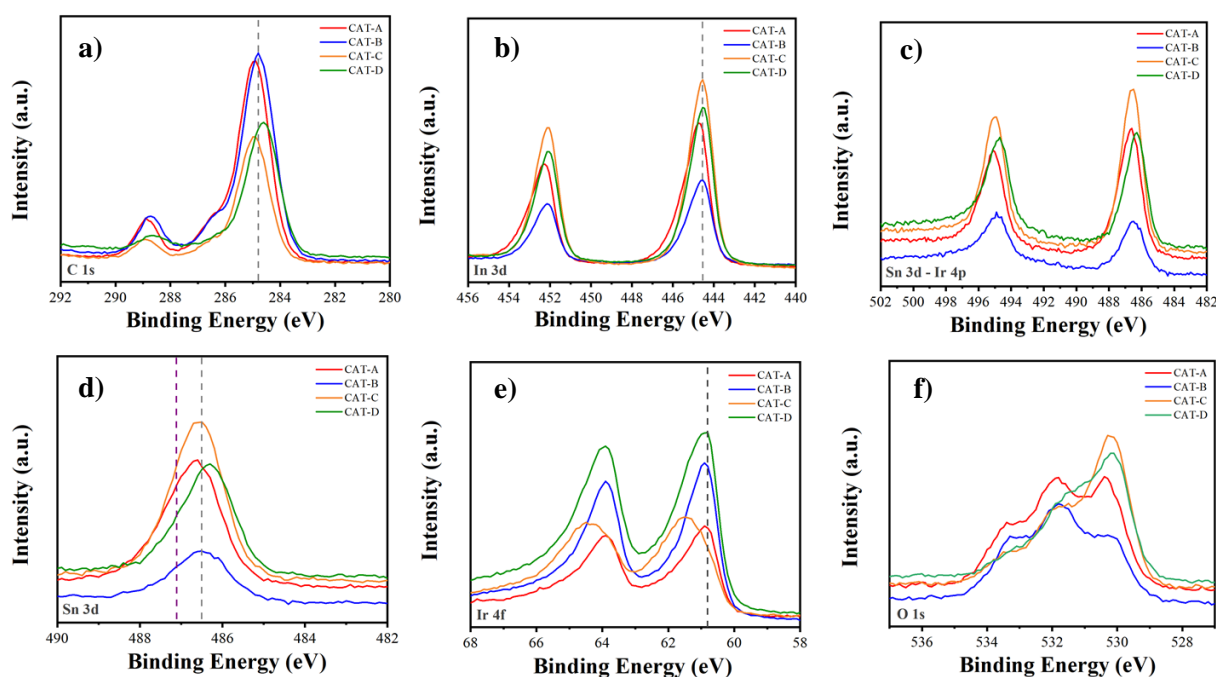
Figure 5.8: XPS narrow scans showing **a)** C 1s region, **b)** In 3d region, **c)** Sn 3d and Ir 4p regions, **d)** close-up of Sn $3d_{5/2}$ peak, **e)** Ir 4f region and **f)** O 1s region.

The C 1s spectra showed two major components for all measured electrocatalysts (Figure 5.8 a)). The peak at 284.8 eV of binding energy scale (indicated by a grey dotted line) is due to adventitious carbon (sp^2 carbon components) and is commonly used as a cross-calibration to check for surface charging.

All C 1s spectra are well aligned suggesting the absence of surface charging. A small shift of 0.2 eV to lower binding energy side observed for CAT-D is within the instrumental error. A shoulder-like feature, which was more pronounced on CAT-A and CAT-B, in the binding energy range from 286–288 eV, indicates possible contributions from carbon bonded to oxygen species such as C-O-C; C-OH (Biesinger, 2021; Naumkin & Kraut-Vass, 2012). The peak feature observed at 288–290 eV may suggest contribution from an acetyl group which could

be leftover by-product from the Ir(acac)$_3$ precursor decomposition during the deposition process.

In Figure 5.8 b), the In spectra is shown. For In 3d$_{5/2}$ the peak position is consistent with being in 3+ oxidation state (i.e., In$_2$O$_3$), which is indicated by a grey dotted line (Detweiler et al., 2019; Donley et al., 2002). However, the asymmetric peak broadening towards higher binding energy side especially displayed in spectra from CAT-B and CAT-D suggest that another In component may be present as well.

The narrow scan in the binding energy for Sn 3d and Ir 4p region is shown in Figure 5.8 c). The visible peaks are due to Sn 3d doublet (Sn 3d$_{5/2}$ and Sn 3d$_{3/2}$), however the characteristic peak of Ir 4p$_{3/2}$ occurs at the same binding energy of the Sn 3d$_{3/2}$ at 495.0 eV. The contribution of Ir 4p$_{3/2}$ is clearly seen in the CAT-B spectra where the specific intensity ratio for the Sn 3d peaks was inverted. This is due to the stronger contribution for the overlapping Ir 4p$_{3/2}$ signal in CAT-B compared to the other samples. This is consistent with CAT-B surface composition data (Table 5.3) as the largest surface Ir mass concentration was found for this sample. Figure 5.8 d) of the Sn3d$_{5/2}$ component indicates the peak position of an Sn^{2+} (SnO) species with a grey dotted line and Sn^{4+} (SnO$_2$) species with a purple dotted line (Naumkin & Kraut-Vass, 2012; Teterin et al., 2020). Based on the peak positions, it can be deduced that majority of Sn is present in 2+ oxidation state rather than 4+.

Interestingly, the Ir 4f spectra (Figure 5.8 e)) indicated that for three electrocatalysts, the binding energy position of Ir 4f$_{7/2}$ component appears consistent with metallic iridium occurring at 60.8 eV (Pfeifer et al., 2016), while for CAT-C the spectrum is shifted to higher binding energy 61.5 eV. This was unexpected as based on the synthesis conditions which were used, iridium was expected to be in present predominantly as Ir^{4+} in all samples.

In the O 1s spectra, three overlapping peaks are visible. In Figure 5.8 f) the peaks for CAT-C and CAT-D have an appearance of shoulder-like feature than defined peaks seen in CAT-A and CAT-B. The peak occurring at 530.2–530.4 eV of binding energy scale, is the dominant contribution in all O 1s spectra, and is characteristic for oxygen bonded to metallic components (Biesinger, 2021; Naumkin & Kraut-Vass, 2012). Peaks in the binding energy range of 531–533 eV likely correlate to oxygen bonded to carbon species.

5.4.2 Interpretation of the XPS curve-fitted spectra

As raw XPS data indicated that electrocatalyst components are present in more than one oxidation state, curve fitting process was applied to explore possible sub-components and quantify their contributions. Figure 5.9 illustrates fitted spectra for In $3d_{5/2}$, Sn $3d_{5/2}$, Ir 4f and O1s obtained from CAT-A as an example, while the information on how the quantitative contribution from these sub-components changes between electrocatalysts is presented in Figure 5.10. Please refer to *Figure B.2*, *B.3 and B.4* in *Appendix B* to see the fitted spectra for all other electrocatalysts.

The curve-fitting for In 3d and Sn 3d spectra fitting for all prepared electrocatalysts followed a similar approach taken by Detweiler et al. (2019), Donley et al. (2002) and Teterin et al. (2020). For Ir 4f and O 1s curve-fitted spectra was performed by with reference to fitting done by to Rajan et al. (2020), Pfeifer et al. (2016) and Yu et al. (2018). The quantification of contributions of each component (Figure 5.10) was determined from the fitted area of each component, relative to the total fitted area.
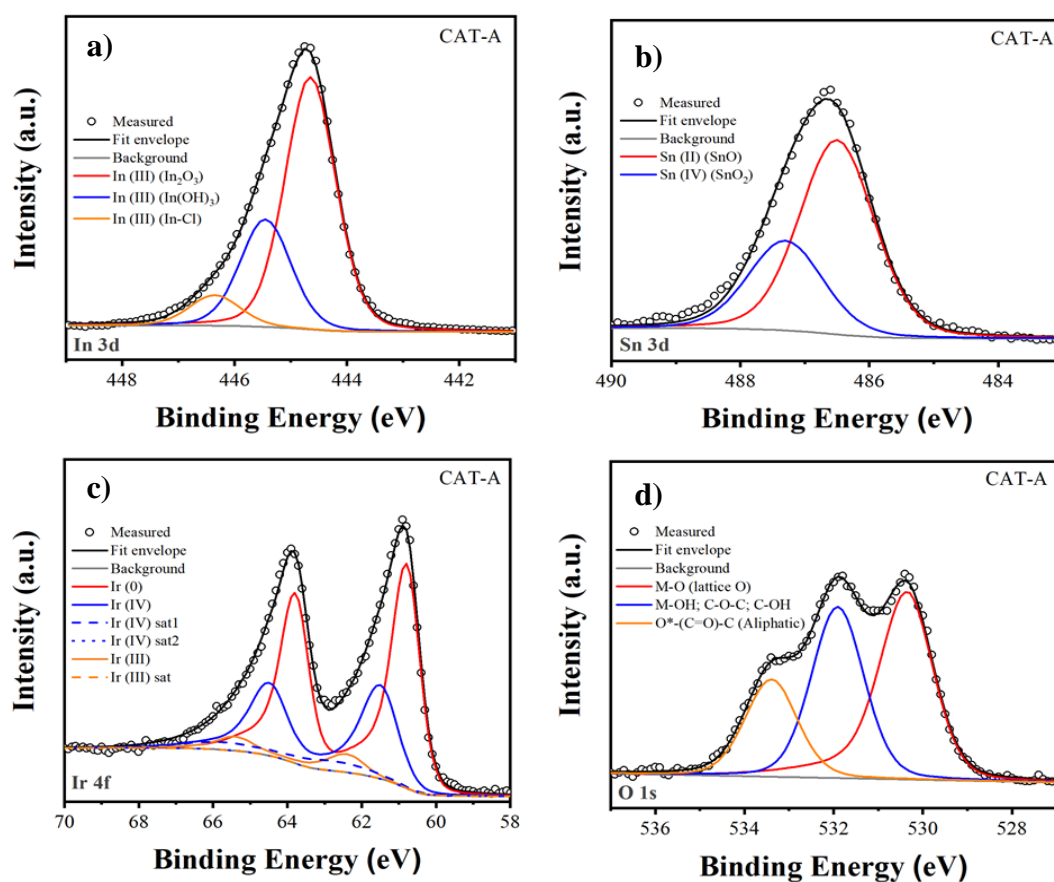
Figure 5.9: XPS curve-fitted spectra for CAT-A of a) In 3d, b) Sn 3d, c) Ir 4f and d) O 1s regions.

For CAT-A, the curve-fitted In spectra (refer to Figure 5.9 a)), shows all contributions are attributed to the +3 oxidation states and that major component is due to In_2O_3. Peaks shifted to higher binding energies are consistent with contributions from $In(OH)_3$ at 445.5 eV and In bonded to chlorine species at 446.4 eV (Biesinger, 2021; Naumkin & Kraut-Vass, 2012). $In(OH)_3$ is most likely due to the hydroxylation on the surface of the ITO surface due to the disrupted ITO lattice (Donley et al., 2002). In Figure 5.9 b), the Sn spectra display that asymmetric broadening of the peak correlates with presence of two Sn components: SnO at 486.5 eV and SnO_2 at 487.1 eV. This combination of SnO and SnO_2 present on the surface of the electrocatalysts, may be attributed to imperfections in the ITO lattice structure (Teterin et al., 2020). The Ir spectra, shows that the Ir species on the surface consists mostly of metallic Ir (refer to Figure 5.9 c), however the peak shifts towards the higher binding energy region due the contribution of Ir^{4+} and minor contribution Ir^{3+} and their associated satellites. The O spectra in Figure 5.9 d) shows the overlapping of three major components that have contributions belonging to metal bonded to oxygen, hydroxyl group and several possible hydrocarbon groups which are in this binding energy range.
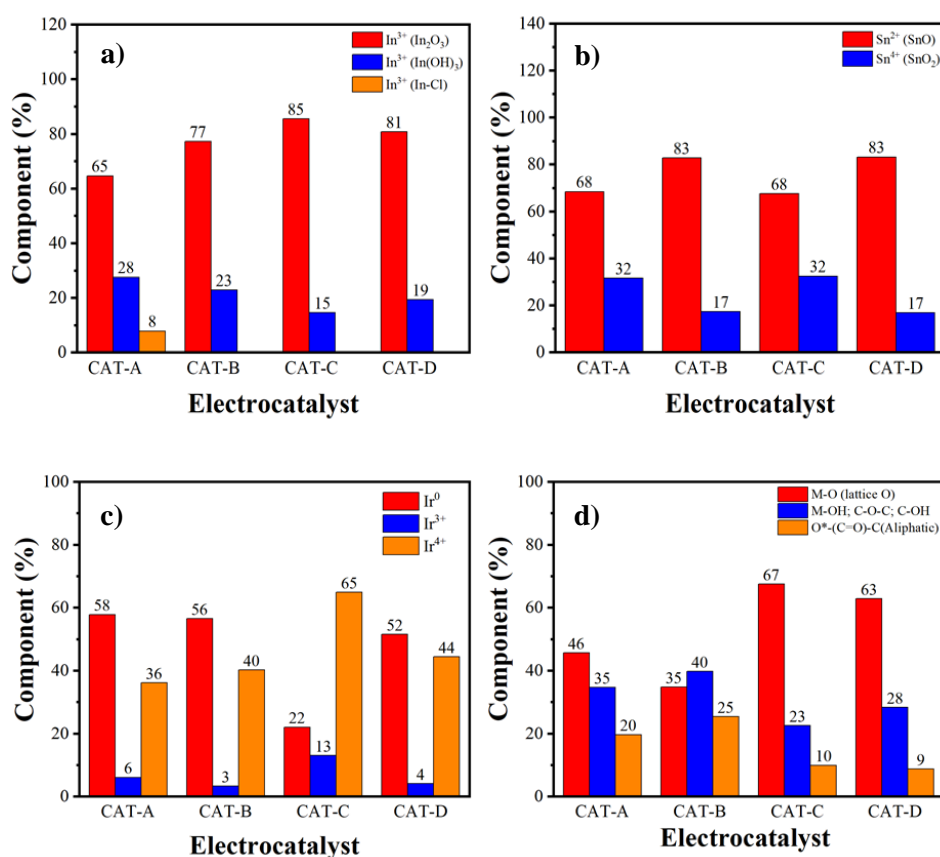
Figure 5.10: Component contributions for (**a–d**) In 3d, Sn 3d, Ir 4f and O 1s respectively, for the prepared IrO_x/ITO electrocatalysts.

As indicated in Figure 5.10 a), all electrocatalysts have dominant surface contribution from In_2O_3, followed by $In(OH)_3$ and In bonded to Cl (only occurring in CAT A) .This was consistent with the surface composition concentrations, which showed that CAT-A had the largest quantities of chlorine of 0.5% and 0.64%, for atomic concentration and mass concentration respectively (refer to Table 5.3).

For the Sn spectra, it is evident that in all prepared electrocatalysts the dominant component is Sn^{2+} (SnO) followed by and Sn^{4+} (SnO_2) (refer to Figure 5.10 b)). The electrocatalysts with small particle size or high BET surface area ITO support, CAT-A and CAT-C, have the same relative contribution of Sn^{2+} (68%) versus Sn^{4+} (32%) while those with the larger particle size or low BET surface area ITO support, CAT-B and CAT-D, both have a higher contribution of Sn^{2+} (83%). This difference in Sn component contributions could potentially be attributed to a support particle size effect in electrocatalysts. As all XPS data presented in this study were done for the electrocatalysts only, to confirm whether or not this is the case for the support materials prior to the catalytic nanoparticles' deposition, it would be recommended to perform further XPS measurements of the ITO support only.

From the Ir 4f spectra, it was found that for all the electrocatalysts except for CAT-C, that Ir is deposited in a primarily metallic form. Basically, unlike for electrocatalysts prepared on ATO support (Rajan et al. 2020), metallic iridium failed to undergo complete oxidation on ITO support. A small contribution for Ir^{3+} implied possible formation of iridium oxyhydroxide species (Pfeifer et al., 2016), or that perhaps not all the metal-organic Ir(acac)$_3$ precursor decomposed during the deposition process. This is interesting as all catalysts underwent the same MOCD deposition conditions as in Rajan et al. (2020), who reported Ir^{4+} as the dominating Ir species on ATO ($SnO_2:Sb_2O_3$ = 90:10 wt.%, approx. 30 nm particle size; < 95 m^2g^{-1} BET surface area). For ATO support, most of the bulk and surface Sn is in 4+ oxidation state as SnO_2, while in ITO support, Sn is the minority component and occurring in more than one oxidation state (Teterin et al., 2020). A possible reason may be due to the interaction of the different surface groups on the surface of the support with precursor of the deposited catalyst during the deposition process as proposed by a study by Jackson et al. (2020) which utilised the same deposition technique for the preparation of Pt supported electrocatalysts (Jackson et al., 2020). Another possible reason for differences seen in nature of IrO_x species on ITO and ATO may be due the deposition heat treatment temperature (320°C) not being sufficient to drive the formation of Ir^{4+} on the surface of ITO support. Such as a temperature of only 400 °C

or greater is suggested to produce the successful formation of Ir^{4+} onto an oxide support (Kasian et al., 2021). This implies that the support material can significantly influence the nature of the Ir species forming during the MOCD process.

For CAT-C, a large portion successfully underwent complete oxidation as it had dominant contribution for Ir^{4+} of 65%, with secondary contribution for metallic iridium of 22% and a contribution for Ir^{3+} of 13%. (Figure 5.10 c)). This suggests a possible optimum reached for Ir^{4+} component contribution, with a small particle size and larger surface Sn dopant content compared to the other electrocatalysts (see Table 5.3).

In Figure 5.10 d), the O 1s spectra, the highest contribution for all the electrocatalysts except for CAT-B, was from oxygen bonded to metal species 530.3 eV of binding energy scale. However relative contributions from Sn, In or Ir oxygen bonded species cannot be distinguished. The oxygen bonded to metal contribution in CAT-C and CAT-D is higher (67% and 63% respectively) than compared to those seen in CAT-A (46%) and CAT-B (35%). For CAT-B, peak at the binding energy of 532 eV combines of contributions from metal bonded to hydroxyl group (Sn, In and Ir hydroxyl species) as well as oxygen bonded to hydrocarbon moieties present on the surface. The 3rd component with smallest contribution seen in all electrocatalysts is assigned to oxygen bonded to carboxylic group in aliphatic carbon species. This is in agreement with components displayed in C 1s spectra due to incomplete removal of the $Ir(acac)_3$ decomposition by-products.

To investigate if and how the ITO support influences the nature of the deposited catalytic nanoparticles, various surface component ratios of electrocatalysts were correlated against ITO supports' average BET surface area. Figure 5.11 illustrates correlations found between electrocatalyst surface ratio components and ITO average BET surface area. It is clear from Figure 5.11 a) that in electrocatalysts utilising low BET surface area ITO supports, higher surface Sn^{2+}/Sn^{4+} and lower $In(OH)_3/In_2O_3$ component ratios were observed. More interestingly, Figure 5.11 b) shows that in electrocatalysts higher surface Ir^{4+}/Ir^{3+} component ratio correlates with larger Sn^{2+}/Sn^{4+} and lower average BET surface area ITO supports.

These findings further reinforce the conclusion that the nature of ITO surface, especially with respect to the nature of Sn species influences the nature of deposited catalytic nanoparticles on its surface. In addition, the results in this chapter showed that the MOCD technique was successfully extended from utilisation with ATO to ITO support material, where uniformly distributed, small (2.1–2.4 nm) size, IrO_x nanoparticles were deposited.
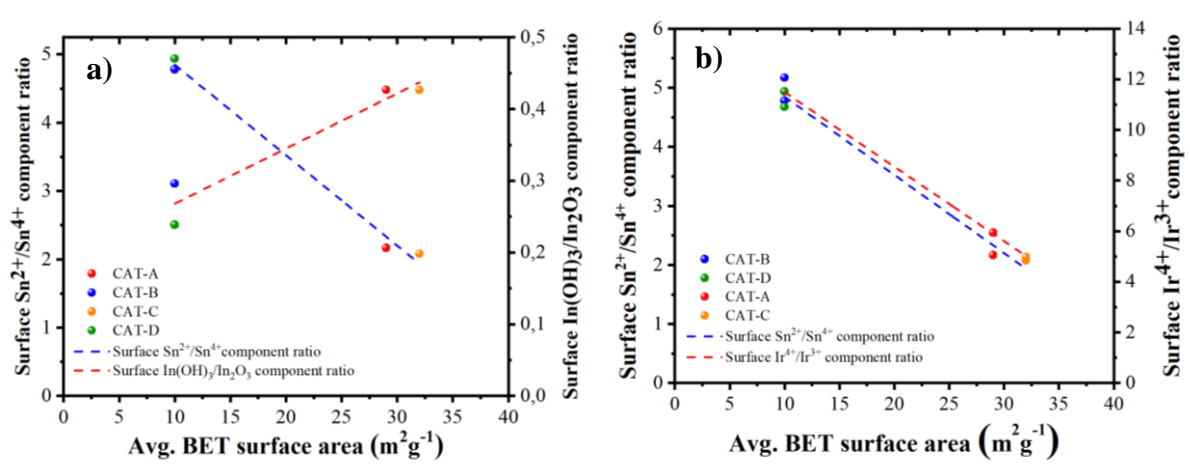
Figure 5.11: **a)** Correlations between the electrocatalysts' surface Sn and In component ratios vs. average BET surface area and **b)** Correlations between the electrocatalyst's surface Sn and IR component ratios and average BET surface area.

CHAPTER 6: IRIDIUM-BASED SUPPORTED ELECTROCATALYSTS – ELECTROCHEMICAL PROPERTIES

In this chapter, the development of an understanding of the behaviour of the electrochemical performance of the prepared MOCD IrO$_x$/ITO electrocatalysts, is done by taking into consideration the results achieved by the physical characterisation of these electrocatalysts. The best performing electrocatalyst is also compared to other ITO and ATO supported electrocatalysts from recent publications.

6.1 The electrochemical performance evaluation of the electrocatalysts

The *ex-situ* OER electrochemical evaluation of the prepared electrocatalysts was done according to the testing protocol described in *Chapter 3*, *Section 3.3.4*. Table 6.1 summarises the derived the mass specific OER activities, relative OER percentage activity loss after stability tests and the corresponding Tafel slopes values before and after stability tests were carried out.

Initial performance evaluation indicates that CAT-A and CAT-B are the most promising as they have significantly higher mass-specific OER activities compared to CAT-C and CAT-D (refer to Table 6.1). These activities were between 10 to 25 times better than that of the IrO$_2$/TiO$_2$ commercial benchmark tested under the same conditions. In comparison to other IrO$_x$/ITO electrocatalysts, the prepared electrocatalysts had better initial electrochemical performance than the electrocatalysts reported by Lebedev & Copéret (2019), however they were outperformed by electrocatalysts prepared by Lebedev et al. (2020). Based on initial OER activities, this indicate that ITO may indeed be a suitable OER catalyst support.

However, in some studies (Benck et al., 2014; Geiger et al., 2017; Ledendecker et al., 2019) it has been said that the stability of ITO hinders its ability to perfom well as an OER support material. As such, the usage of ITO support is brought into question. Here we aim to explore if the nature of deposited IrO$_x$ nanoparticles and their coverage potentially stabilise ITO support, making it more applicable for OER. To this end, the most active CAT-A and second active but most stable CAT-B is discussed in more detail compared to the other two electrocatalysts.

As reported in *Chapter 3*, these electrocatalysts were prepared using high and low BET surface area ITO supports respectively. In general, it is expected that initial mass specific OER activity

of a catalyst on high surface area supports will be higher compared to that on low surface area support. Given that the particle size and iridium loading of IrO_x catalytic nanoparticles are similar, the outcome of the electrochemical performance cannot be due to the methodology used. That is why it is interesting to understand why CAT-B has a higher performance compared to both CAT-C and CAT-D. A possible link to the bulk composition of the ITO support could be made, where CAT-A and CAT-B both have the same bulk composition of In_2O_3: $SnO_2 = 95:5$, suggesting that lower dopant content is optimal for the preparation of these electrocatalysts.

Figure 6.1 shows comparison of *ex-situ* mass specific OER activities for the prepared electrocatalysts, before and after stability test.
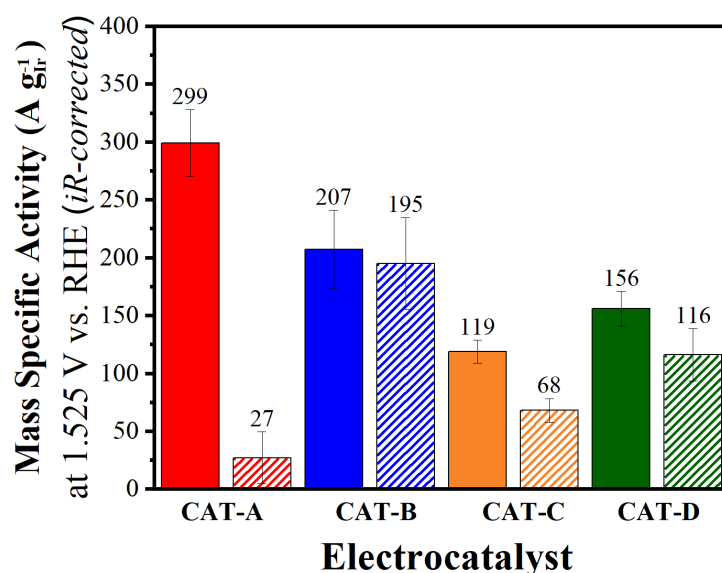
Figure 6.1: *Ex-situ* mass specific OER activities of all prepared IrO_x/ITO electrocatalysts, before (solid bar) and after (pattern bar) stability testing by chronoamperometry.

Electrocatalysts prepared on the low BET surface area ITO supports demonstrated higher stability compared to those on low surface area ITO, with CAT-B experiencing only 6% relative OER activity loss (refer to Table 6.1). The most active CAT-A is the least stable MOCD IrO_x/ITO electrocatalyst, while in comparison the IrO_2/TiO_2 commercial benchmark demonstrated 70% relative mass-specific OER activity loss. From these results, an ITO supported electrocatalyst with low iridium loading of 11 wt.% prepared in this study, proved to be more active and relatively stable compared to the commercial benchmark with significantly higher iridium loading of 75 wt.%. This could be owing to greater iridium utilisation over the conductive ITO support.

Table 6.1: *Ex-situ* mass specific OER activities at 1.525 V vs.RHE, iR-corrected, Tafel slope values and summary of key data from the physical characterisation of the prepared MOCD IrO$_x$/ITO electrocatalysts.

Sample I.D.	Support Avg. BET surface area	Avg. Ir loading (wt.%)	IrO$_x$ Particle size (nm)	Surface Ir^{4+}/Ir^{3+} component ratio	Surface Metallic Ir/Ir^{3+} component ratio	Initial Mass-specific OER activity (A g$_{Ir}^{-1}$)	After 1.6V CA Mass-specific OER activity (A g$_{Ir}^{-1}$)	Relative OER activity loss (%)	Initial Tafel slope value (mV dec^{-1})	After 1.6 V CA Tafel slope value (mV dec^{-1})
CAT-A	29	8	2.4 ± 0.6	5.94	9.50	299± 29	27 ± 23	91	54 ± 4	84 ± 4
CAT-B	10	11	2.4 ± 0.7	12.04	16.95	207 ± 34	195 ± 40	6	57 ± 7	49 ± 2
CAT-C	32	12	2.3 ± 0.7	4.97	1.69	119 ± 10	68 ± 10	43	62 ± 6	70 ± 4
CAT-D	10	11	2.1 ± 0.5	10.90	12.66	156 ± 15	116 ± 23	26	58 ± 1	52 ± 2
Commercial benchmark	-	75	-	-	-	11.9 ± 3.3	3.6 ± 1.8	70	54 ± 2	61 ± 1

6.2 Correlations between nature of electrocatalysts and their electrochemical performance

The following discussion focuses on understanding if the nature of MOCD IrO_x/ITO electrocatalysts, especially their surface compositions correlate with electrochemical performance and stability.

For CAT-A, CAT-B and CAT-D, the XPS analysis showed that they exhibited the same nature of Ir species. Metallic iridium was the dominant species ($\sim$51–58 %) in these electrocatalysts and can be attributed to their initial large mass specific activity compared to CAT-C as Ir metal produces a higher OER activity than of its corresponding metal oxide, IrO_2. The initial higher OER activity corresponds to metallic iridium becoming electrochemically activated for OER as upon subjection to an oxidising electrochemical potential as it immediately oxidises on the surface of the electrode leading to the formation amorphous IrO_x, which has the combination of Ir^{4+} and Ir^{3+} species (Lebedev & Copéret, 2019; Pfeifer et al., 2016; Zagalskaya & Alexandrov, 2020). As Ir^{3+} is most likely to undergo iridium dissolution, this could be significantly contributing to the instability of the electrocatalysts. CAT-B and CAT-D, both made from low BET surface area supports have similar Ir, Ir^{4+} and Ir^{3+} amounts, but the initial activity of CAT-B is somewhat larger, and catalyst is more stable. This can be explained by increased IrO_x catalytic nanoparticles coverage for CAT-B compared to CAT-D (refer to Figure 5.7 and Ir/In surface wt.% ratio, Table 5.3), as well as larger surface Ir^{4+}/Ir^{3+} component ratio (refer to Table 6.1).

For CAT-A and CAT-B, the difference in the initial mass specific OER activities between the two electrocatalysts, may be due a greater Ir utilisation on the surface of ITO support. Highly dispersed IrO_x catalytic nanoparticles with lower coverage are present on the small particle sized ITO support in CAT-A. In addition, the blue-coloured ITO is also seen to be more electronically conductive than the yellow-coloured ITO material, which could possibly explain the higher initial mass specific OER activity for CAT-A compared to CAT-B. As CAT-A and B have exhibited the same composition and nature, with regards to the Ir species, it would be expected that both electrocatalysts should lack stability, however this is not the case. Figure 6.2 a) shows that, CAT-B has a lower surface $In(OH)_3/In_2O_3$ and greater surface Ir^{4+}/Ir^{3+} component ratios than CAT-A which plays a role in the stability seen. CAT-B also has highest Metallic Ir/Ir^{3+} component ratio value (Figure 6.2 b). It is speculated that higher $In(OH)_3/In_2O_3$

measured from electrocatalysts (post-deposition) would contribute to their lower stability due to dissolution of $In(OH)_3$ species.
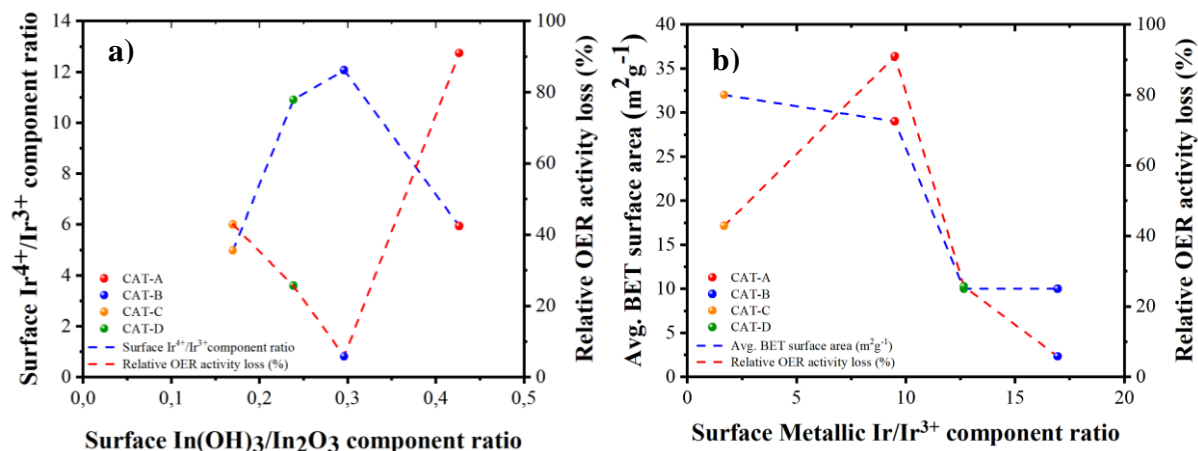
Figure 6.2: Correlations between the relative OER activity loss and the surface nature of the electrocatalysts a) for surface $In(OH)_3/In_2O_3$ component ratio vs. Ir^{4+}/Ir^{3+} component ratio and relative OER activity loss and b) for surface Metallic Ir/Ir^{3+} component ratio vs. average BET surface area of the ITO support and relative OER activity loss.

Figure 6.3 a) illustrates CAT-A and CAT-B the Tafel slopes for CAT-A and CAT-B of 54 mV dec^{-1} and 57 mV dec^{-1}, which changed after the stability testing to 49 mV dec^{-1} and 84 mV dec^{-1}, respectively. The Tafel slope for CAT-A was comparable to reported 60 mV dec^{-1} for unsupported iridium oxides (Oh, H.S. et al., 2016; Reier, Oezaslan & Strasser, 2012). The slight drop in the Tafel slope value for CAT-B is most likely correlated to the degree of hydration of the hydrous, amorphous IrO_x that formed during the electrochemically during the OER performance evaluation (Minguzzi et al., 2015). The significant change in Tafel slope values for CAT-B was indicative to the relative loss of OER activity. This can also be observed from the raw data of the stability testing, refer to Figure 6.3 b), where a steeper decline in the current response (at applied potential of 1.6 V vs. RHE) was seen for CAT-A compared to CAT-B. Although it was noted in this study that that relative OER activity loss was determined by comparison of OER activities after an applied potential rather than iR-corrected potential. This is due to fluctuations seen ohmic losses observed where high current response is seen. The average iR-corrected potential vs. RHE for this stability CA step was determined and showed that experienced potential differed from each other where 1.554 V and 1.542 V for CAT-A and CAT-B respectively.
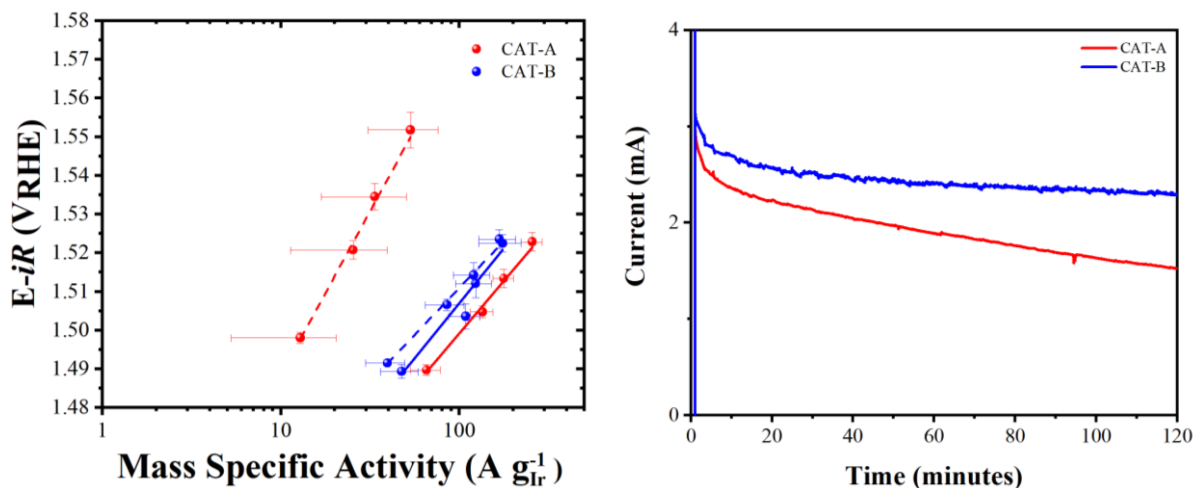
Figure 6.3: **a)** Mass specific Tafel slopes for CAT-A and CAT-B, before (solid line) and after (dashed line) stability testing by chronoamperometry. **b)** The averaged current response seen for CAT-A and CAT-B at the applied potential of 1.6 V vs. RHE held for 2hrs.

In recent studies, the operating conditions of the electrochemical RDE set-up have been reported not to lead to activity loss of the electrocatalysts through dissolution of the IrO_x catalytic nanoparticles or by their physical detachment of these supported particles (El-Sayed et al., 2019; Moriau et al., 2021). As such, the activity loss would be due to the integrity of the support material only. Thus, in this study, the relative loss in mass specific OER activity can be attributed to the degradation of the ITO support itself. This would weaken the interaction between the support and IrO_x catalytic nanoparticles leading to a rapid decline in the electrochemically active surface area of the IrO_x. This corresponded with ITO being chemically unstable in acidic environments, which is supported by the results from the chemical dissolution of the ITO support in *Chapter 4*, *Section 4.2.5*

However, CAT-B had a significantly lower relative OER activity loss compared to CAT-A, which is consistent with the results from the chemical dissolution test which showed that the low BET surface area ITO support, i.e. ITO-B was more chemically stable compared to ITO-A. It can also be suggested that higher coverage of Ir species on the surface of CAT-B can further stabilise its ITO support.

CAT-C and CAT-A are both prepared on high surface area ITO supports. As higher surface area supports are more chemical unstable, it was expected that both electrocatalysts would experience similar relative OER mass-specific activity loss. However, CAT-C is significantly more stable, which is likely due to Ir^{4+} being the predominant IrO_x species on its surface and

lower surface $In(OH)_3/In_2O_3$ component ratio. It can therefore be concluded that the nature of IrO_x species, support surface area and its stability influenced the overall electrocatalyst activity and relative OER mass specific activity loss.

6.3 Comparison of CAT-B vs. catalysts in recently published literature

From this study, CAT-B emerges as the active and most stable ITO supported electrocatalyst. The following discussion focuses on comparison of performance of this catalyst with other ITO and ATO supported catalysts reported in recent published literature.

Figure 6.4 illustrates comparison of the initial average mass specific OER activity of CAT-B to those reported for IrO_x/ITO and IrO_x/ATO electrocatalysts, which exhibited IrO_x catalytic nanoparticles of a similar particle size (0.5–5 nm). Please refer to *Table C.1* in *Appendix C* for summary on the reported supported electrocatalysts from published literature.
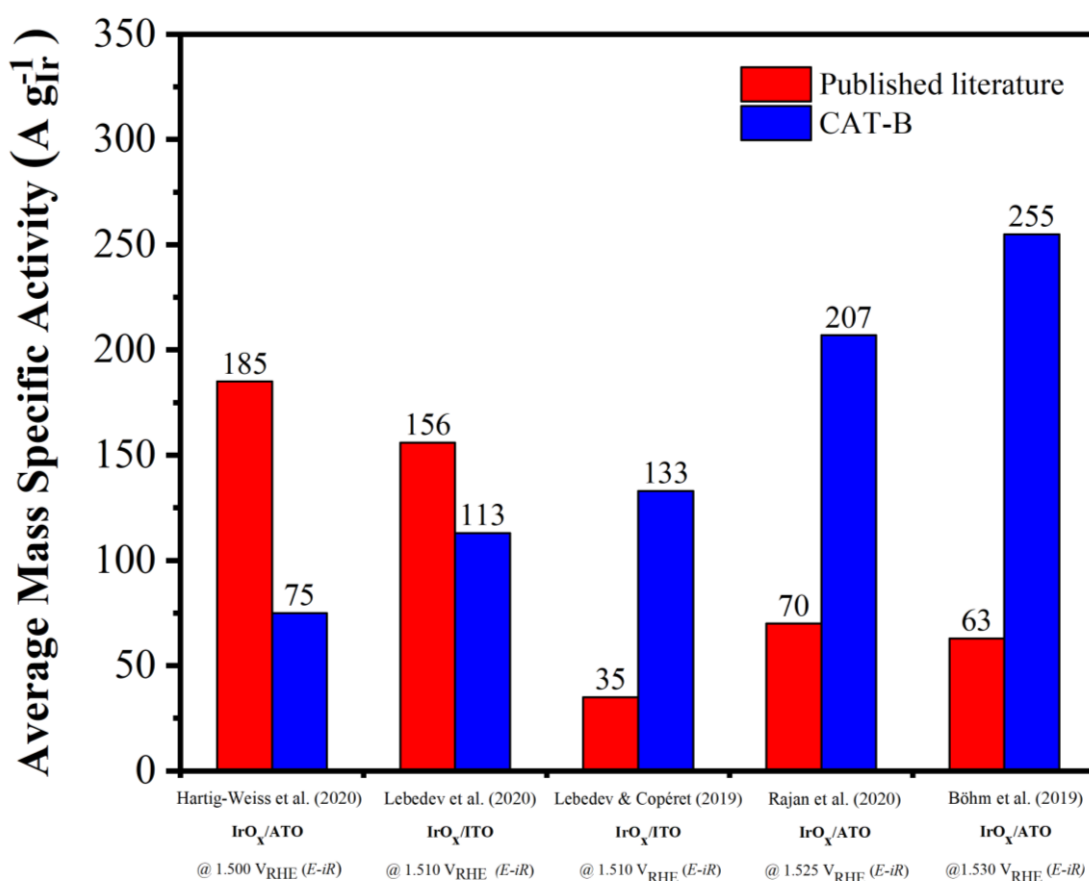

Figure 6.4: Average mass specific OER activities of IrO_x/ITO and IrO_x/ATO electrocatalysts reported in recent literature compared to CAT-B.

CAT-B had a better OER activity compared to the IrO_x/ITO electrocatalyst reported by Lebedev & Copéret (2019), however it had a weaker electrochemical performance compared to IrO_x/ITO electrocatalysts reported by Lebedev et al. (2020). This may be due to the atomically dispersed and very small particle size range of 0.5–1 nm of the IrO_x catalytic nanoparticles and their associated greater Ir utilisation over the ITO support material (Lebedev et al., 2020).

The MOCD IrO_x/ITO electrocatalyst had better initial electrochemical performance than MOCD IrO_x/ATO electrocatalyst that was prepared using similar deposition conditions. The reason for this was that higher OER activity is produced by the Ir species dominating the surface of ITO support which was metallic Ir compared to the rutile IrO_2 that Rajan et al. (2020) reported which was the dominating Ir species on the ATO support.

When evaluated against IrO_x/ATO electrocatalysts which was prepared by a different deposition technique (Hartig-Weiss et al. (2020), CAT-B had a lower electrochemical performance. This may be because IrO_x/ATO prepared by polyol method has higher catalyst utilisation with smaller IrO_x particle size distribution range of 0.5–3 nm, thus possibly demonstrating larger electrochemically active surface area compared to CAT-B.

The varying of the physiochemical properties (i.e., particle size, BET surface area; In_2O_3: SnO_2 ratios etc.) proved to influence the OER performance of the electrocatalysts. This is exhibited by the supported electrocatalysts that were prepared on large particle sized (low BET surface area) ITO supports had small IrO_x nanoparticles (2.1-2.4 nm) with higher IrO_x coverage and improved to be more stable. This suggested a possible IrO_x stabilising effect on the ITO support. Apart from the improved stability, the deposited catalyst, predominately present as Ir metal produced high mass specific OER activity of 299 ± 29 A g_{Ir}^{-1} at 1.525 V vs. RHE, seen on the lower Sn dopant content, large particle sized ITO support. It can be concluded that MOCD technique successfully prepared an IrO_x/ITO electrocatalysts that had good electrochemical performance in relation to both published IrO_x/ATO and IrO_x/ITO prepared electrocatalysts.

CHAPTER 7: CONCLUSIONS AND RECOMMENDATIONS

A summary of the main conclusions from this study and recommendations for future work is given.

This dissertation has demonstrated the successful application of the metal-organic chemical deposition (MOCD) for the deposition of IrO_x nanoparticles onto tin-doped indium oxide (ITO) support. The nature of the support surface was found to influence the deposited catalysts' coverage and oxidation state. The supported electrocatalysts prepared on the low BET surface ITO support have higher surface Sn^{2+}/Sn^{4+} and Ir^{4+}/Ir^{3+} component ratios. This indicated that Sn species on the ITO surface potentially influenced the formation of Ir^{4+}. A lower $In(OH)_3/In_2O_3$ component ratio was also observed. This coupled with the higher coverage IrO_x catalytic nanoparticles on the low BET surface area ITO support produced more electrochemically stable electrocatalysts compared to those that utilised high BET ITO surface area supports. This demonstrated the possible stabilisation of the ITO support by the deposited catalyst. The nature of the IrO_x (x = 0–2) nanoparticles influenced the electrochemical activity of the electrocatalysts as the metallic iridium was found to be the predominant catalyst component. As such, it is seen as a greater source of electrochemical activity under OER operating conditions than the rutile IrO_2, as a high mass specific OER activity was observed.

To gain further understanding of the influence of the MOCD technique on the ITO support, it would be recommended to perform XPS analysis on the ITO support prior to deposition of IrO_x nanoparticles. XPS analysis could also be used to examine the electrocatalysts post-electrochemical testing to confirm the formation of hydrous, amorphous iridium oxide from the dominating metallic iridium phase present on the surface of the electrocatalysts.

This study did not utilise techniques for investigating the electronic conductivity of the ITO support materials, such as the collinear four-point probe method to measure resistivity and Hall measurements which can provide information on both the nature and quantification of the electronic conductivity. The electronic conductivity of the support plays an essential part in the overall OER performance of an electrocatalyst as this provides pathways for electrons to move throughout the reactive interfaces and this could provide meaningful information on the influence of the varying properties of the ITO support. The influence of coverage the IrO_x nanoparticles could be investigated by an iridium mass loading study of both the high and low BET surface area ITO support materials. Further validation of the electrochemical stability

results could be performed as the stability results are based on a comparison at the same applied potential rather than same iR-corrected potential. The viability of the best IrO_x/ITO electrocatalyst for PEMWE could be further explored in an MEA configuration via single-cell electrolyser testing.

REFERENCES

Abbott, D.F., Lebedev, D., Waltar, K., Povia, M., Nachtegaal, M., Fabbri, E., Copéret, C. & Schmidt, T.J. 2016. Iridium Oxide for the Oxygen Evolution Reaction: Correlation between Particle Size, Morphology, and the Surface Hydroxo Layer from Operando XAS. *Chemistry of Materials.* 28(18):6591-6604.

Abdol Rahim, A.H., Salami Tijani, A., Kamarudin, S.K. & Hanapi, S. 2016. An overview of polymer electrolyte membrane electrolyzer for hydrogen production: Modeling and mass transport. *Journal of Power Sources* 309:56-65.

Ahmad Kamaroddin, M.F., Sabli, N., Tuan Abdullah, T.A., Siajam, S.I., Abdullah, L.C., Abdul Jalil, A. & Ahmad, A. 2021. Membrane-Based Electrolysis for Hydrogen Production: A Review. *Membranes.* 11(810).

Akbari, B., Tavandashti, M. Pirhadi, and Zandrahimi, M. 2011. PARTICLE SIZE CHARACTERIZATION OF NANOPARTICLES –A PRACTICAL APPROACH. *Iranian Journal of Materials Science & Engineering.* 8(2):48-56.

Audichon, T., Mayousse, E., Morisset, S., Morais, C., Comminges, C., Napporn, T.W. & Kokoh, K.B. 2014. Electroactivity of RuO2–IrO2 mixed nanocatalysts toward the oxygen evolution reaction in a water electrolyzer supplied by a solar profile. *International Journal of Hydrogen Energy.* 39(30):16785-16796.

Ayeshamariama, A., Kashif, M., Bououdina, M., Hashimb, M., Jayachandrane, M. & Ali, M.E. 2014. Morphological, structural, and gas-sensing characterization of tin-doped indium oxide nanoparticles. *Ceramics International.* 40:1321-1328.

Bareiß, K., de la Ruaa, C., Möckl, M. & Hamacher, T. 2019. Life cycle assessment of hydrogen from proton exchange membrane water electrolysis in future energy systems. *Applied Energy.* 237:862-872.

Benck, J.D., Pinaud, B.A., Gorlin, Y. & Jaramillo, T.F. 2014. Substrate Selection for Fundamental Studies of Electrocatalysts and Photoelectrodes: Inert Potential Windows in Acidic, Neutral, and Basic Electrolyte. *PLoS ONE.* 9(10): e107942.

Bender, G., Carmo, M., Smolinka, T., Gago, A., Danilovic, N., Mueller, M., Ganci, F., Fallisch, A. et al. 2019. Initial approaches in benchmarking and round robin testing for proton exchange membrane water electrolyzers. *International journal of hydrogen energy* 44:9174-9187.

Biesinger, M.C. 2021. *X-ray Photoelectron Spectroscopy (XPS) Reference Pages*. Available: http://www.xpsfitting.com/ [2021, 20 December].

Böhm, D., Beetz, M., Schuster, M., Peters, K., Hufnagel, A.G., Döblinger, M., Böller, B., Bein, T. et al. 2019. Efficient OER Catalyst with Low Ir Volume Density Obtained by Homogeneous Deposition of Iridium Oxide Nanoparticles on Macroporous Antimony-Doped Tin Oxide Support. *Advanced Functional Materials.* 30(1): 1906670.

Bosch, H. & Peppelenbos, A. 1977. Automatic and low-cost determination of BETsurface areas. *Journal of Physics E: Scientific Instruments.* 10: 605-608.

Bowen, P. 2002. Particle Size Distribution Measurement from Millimeters to Nanometers and from Rods to Platelets. *JOURNAL OF DISPERSION SCIENCE AND TECHNOLOGY.* 23(5):631-662.

Brauns, J. & Turek, T. 2020. Alkaline Water Electrolysis Powered by Renewable Energy: A Review. *Processes.* 8(248).

Bühler, M., Holzapfel, P., McLaughlin, D. & Thiele, S. 2019. From Catalyst Coated Membranes to Porous Transport Electrode Based Configurations in PEM Water Electrolyzers. *Journal of the Electrochemical Society.* 166(14):F1070-F1078

Carmo, M., Fritz, D.L., Mergel, J. & Stolten, D. 2013. A comprehensive review on PEM water electrolysis. *International Journal of Hydrogen Energy.* 38:4901-4934.

Che, M. & Ve´drine, J.J.C. 2012. *Characterization of Solid Materials and Heterogeneous Catalysts From Structure to Surface Reactivity.*

Collins, L. 2019. *Recharge: Global News and Intelligence for the Energy Transition.* Available: https://www.rechargenews.com/transition/worlds-largest-green-hydrogen-plant-begins-operation-in-austria/2-1-708381 [2021, 16 December].

Da Silva Veras, T., Mozer, T.S., da Costa Rubim Messeder dos Santos, D. & da Silva César, A. 2017. Hydrogen: Trends, production and characterization of the main process worldwide. *International Journal of Hydrogen Energy.* 42:2018-2033.

Detweiler, Z.M., Wulfsberg, S.M., Frith, M.G. & Bocarsly, A.B., Bernasek, S.L. 2019. *The oxidation and surface speciation of indium and indium oxides exposed to atmospheric oxidants.*

Donley, C., Dunphy, D., Paine, D., Carter, C., Nebesny, K., Lee, P., Alloway, D. & Armstrong, N.R. 2002. Characterization of Indium-Tin Oxide Interfaces Using X-ray Photoelectron Spectroscopy and Redox Processes of a Chemisorbed Probe Molecule: Effect of Surface Pretreatment Conditions. *Langmuir.* 18(2):450-457.

El-Sayed, H.A., Wei, A., Olbrich, L.F., Putro, G.P., and & Gasteiger, H.A. 2019. OER Catalyst Stability Investigation Using RDE Technique: A Stability Measure or an Artifact? *Journal of the Electrochemical Society.* 166(8):F458-F464.

Fabbri, E., Habereder, A., Waltar, K., Kötz, R. & Schmidt, T.J. 2014. Developments and perspectives of oxide-based catalysts for the oxygen evolution reaction. *Catal. Sci. Technol.* 4(11):3800-3821.

Fornaciari, J.C., Gerhardt, M.R., Zhou, J., Regmi, Y.N., Danilovic, N., Bell, A.T. & Weber, A.Z. 2020. The Role of Water in Vapor-fed Proton-Exchange-Membrane Electrolysis. *Journal of the Electrochemical Society.* 167(104508).

Garcia, A.C. & Koper, M.T.M. 2018. Effect of Saturating the Electrolyte with Oxygen on the Activity for the Oxygen Evolution Reaction. *ACS Catal.* 8(10):9359-9363.

Geiger, S., Kasian, O., Mingers, A.M., Mayrhofer, K.J.J. & Cherevko, S. 2017. Stability limits of tin-based electrocatalyst supports. *Sci Rep.* 7(1):4595.

GlobalSino. 2020. *Accuracy of EDS Quantification: Practical Electron Microscopy and Database: An Online Book* Available: https://www.globalsino.com/EM/page2513.html [2021, 20 December].
Guenther, G., Schierning, G., Theissmann, R., Kruk, R., Schmechel, R., Baehtz, C. & Prodi-Schwab, A. 2008. Formation of metallic indium-tin phase from indium-tin-oxide nanoparticles under reducing conditions and its influence on the electrical properties. *Journal of Applied Physics.* 104(034501). DOI:10.1063/1.2958323.

Gulf Publishing Holdings LLC, G.P.H. 2021. *Gas Processing & LNG.* Available: http://www.gasprocessingnews.com/news/construction-of-worlds-largest-pem-electrolyzer-completed.aspx [2021, 15 December].

Hartig-Weiss, A., Miller, M., Beyer, H., Schmitt, A., Siebel, A., Freiberg, A.T.S., Gasteiger, H.A. & El-Sayed, H.A. 2020. Iridium Oxide Catalyst Supported on Antimony-Doped Tin Oxide for High Oxygen Evolution Reaction Activity in Acidic Media. *ACS Applied Nano Materials.* 3(3):2185-2196.

Holladay, J.D., Hu, J., King, D.L. & Wang, Y. 2009. An overview of hydrogen production technologies. *Catalysis Today.* 139(4):244-260.

Jackson, C., Smith, G.T., Mpofu, N., Dawson, J.M.S., Khoza, T., September, C., Taylor, S.M., Inwood, D.W. et al. 2020. A quick and versatile one step metal–organic chemical deposition method for supported Pt and Pt-alloy catalysts. *RCS Advances.* 10:19982–19996.

Kalamaras, C.M. & Efstathiou, A.M. 2013. Hydrogen Production Technologies: Current State and Future Developments. *Conference Papers in Energy.* 2013:1-9. DOI:10.1155/2013/690627.

Kasian, O., Li, T., Mingers, A.M., Schweinar, K., Savan, A., Ludwig, A.a. & Mayrhofer, K. 2021. Stabilization of an iridium oxygen evolution catalyst by titanium oxides. *Journal of Physics: Energy.* 3. (034006).

Khan, H., Yerramilli, A.S., D'Oliveira, A., Alford, T.L., Boffito, D.C. & Patience, G.S. 2020. Experimental methods in chemical engineering: X-ray diffraction spectroscopy—XRD. *The Canadian Journal of Chemical Engineering.* 98(6):1255-1266.

Kim, H., Yoo, T.Y., Bootharaju, S.M., Kim, J.H., Chung, D.Y. & Hyeon, T. 2021. Noble Metal-Based Multimetallic Nanoparticles for Electrocatalytic Applications. *Adv. Sci.* (2104054).

Kumar, S.S. & Himabindu, V. 2019. Hydrogen production by PEM water electrolysis – A review. *Materials Science for Energy Technologies* 2: 442-454.

Lebedev, D. & Copéret, C. 2019. Small, Narrowly Distributed Iridium Nanoparticles Supported on Indium Tin Oxide for Efficient Anodic Water Oxidation. *ACS Applied Energy Materials.* 2:196-200.

Lebedev, D., Ezhov, R., Heras-Domingo, J., Comas-Vives, A., Kaeffer, N., Willinger, M., Solans-Monfort, X., Huang, X. et al. 2020. Atomically Dispersed Iridium on Indium Tin Oxide Efficiently Catalyzes Water Oxidation. *ACS Central Science.* 6:1189-1198.

Ledendecker, M., Geiger, S., Hengge, K., Lim, J., Cherevko, S., Mingers, A.M., Göhl, D., Fortunato, G.V. et al. 2019. Towards maximized utilization of iridium for the acidic oxygen evolution reaction. *Nano Research.* 12(9):2275-2280.

Lee, A. 2020. *Recharge: Global News and Intelligence for the Energy Transition*. Available: https://www.rechargenews.com/transition/japan-opens-worlds-largest-green-hydrogen-plant-near-fukushima-disaster-site/2-1-769361 [2021, 16 December].
Liu, J., Qiao, B., Song, Y., Huang, Y. & Liu, J.J. 2015. Hetero-epitaxially anchoring Au nanoparticles onto ZnO nanowires for CO oxidation. *Chem Commun (Camb).* 51(83):15332-15335.

Mamaca, N., Mayousse, E., Arrii-Clacens, S., Napporn, T.W., Servat, K., Guillet, N. & Kokoh, K.B. 2012. Electrochemical activity of ruthenium and iridium based catalysts for oxygen evolution reaction. *Applied Catalysis B: Environmental.* 111-112:376-380.

Massué, C., Pfeifer, V., Huang, X., Noack, J., Tarasov, A., Cap, S. & Schlogl, R. 2017. High-Performance Supported Iridium Oxohydroxide Water Oxidation Electrocatalysts. *ChemSusChem.* 10(9):1943-1957.

Minguzzi, A., Locatelli, C., Lugaresi, O., Achilli, E., Cappelletti, G., Scavini, M., Coduri, M., Paolo Masala, P. et al. 2015. Easy Accommodation of Different Oxidation States in Iridium

Oxide Nanoparticles with Different Hydration Degree as Water Oxidation Electrocatalysts. *ACS Catalysis.* 5:5104−5115.

Moriau, L., Bele, M., Marinko, Z., Ruiz-Zepeda, F., Podboršek, G.K., Šala, M., Šurca, A.K., Kovač, J. et al. 2021. Effect of the Morphology of the High-Surface-Area Support on the Performance of the Oxygen-Evolution Reaction for Iridium Nanoparticles. *ACS Catalysis.* 11:670-681.

Moschovi, A.M., Zagoraiou, E., Polyzou, E. & Yakoumis, I. 2021. Recycling of Critical Raw Materials from Hydrogen Chemical Storage Stacks (PEMWE), Membrane Electrode Assemblies (MEA) and Electrocatalysts. *IOP Conf. Series: Materials Science and Engineering.* 1024(012008).

Music´, S., Popovic´ , S., Maljkovic´, M., Skoko, Z., K. Furic´ , K. & Gajovic´, A. 2003. Thermochemical formation of IrO2 and Ir. *Materials Letters.* 57:4509-4514.

Naumkin, A.V. & Kraut-Vass, A., Gaarenstroom, S.W., Powell, C.J. 2012. *NIST X-ray Photoelectron Spectroscopy Database.* Available: https://srdata.nist.gov/xps/Default.aspx [2021, 20 December].

Niemantsverdriet, J.W. 2007. *Spectroscopy in Catalysis: An Introduction.* Weinheim: WILEY-VCH Verlag GmbH & Co. KGaA.

Nong, H.N., Gan, L., Willinger, E., Teschner, D. & Strasser, P. 2014. IrOx core-shell nanocatalysts for cost- and energy-efficient electrochemical water splitting. *Chem. Sci.* 5(8):2955-2963.

Oakton, E., Lebedev, D., Povia, M., Abbott, D.F.F., Emilliana, Fedorov, A. & Nachtegaal, M.C.r., Christophe Schmidt, Thomas J. 2017. IrO2-TiO2: A High-Surface-Area, Active, and Stable Electrocatalyst for the Oxygen Evolution Reaction. *ACS Catalysis.* 7:2346-2352.

Odetola, P., Popoola, P., Popoola, O. & Delport, D. 2016. Electrodeposition of Functional Coatings on Bipolar Plates for Fuel Cell Applications – A Review. In *Electrodeposition of Composite Materials.* IntechOpen. 232-252.

Oh, H.-S., Nong, H.N. & Strasser, P. 2015. Preparation of Mesoporous Sb-, F-, and In-Doped SnO2Bulk Powder with High Surface Area for Use as Catalyst Supports in Electrolytic Cells. *Advanced Functional Materials.* 25(7):1074-1081.

Oh, H.S., Nong, H.N., Reier, T., Gliech, M. & Strasser, P. 2015. Oxide-supported Ir nanodendrites with high activity and durability for the oxygen evolution reaction in acid PEM water electrolyzers. *Chem Sci.* 6(6):3321-3328.

Oh, H.S., Nong, H.N., Reier, T., Bergmann, A., Gliech, M., de Araújo, J.F., Willinger, E., Schlögl, R. et al. 2016. Electrochemical Catalyst−Support Effects and Their Stabilizing Role for IrOx Nanoparticle Catalysts during the Oxygen Evolution Reaction. *Journal of the American Chemical Society.* 138:12552−12563.

Olesik, J.W. 1991. Elemental Analysis Using An Evalution and Assessment of Remaining Problems. *Analytical Chemistry.* 63(1).

Olesik, J.W. 2020. *Spectroscopy: ICP-OES Capabilities, Developments, Limitations, and Any Potential Challengers?* Available: https://www.spectroscopyonline.com/view/icp-oes-capabilities-developments-limitations-and-any-potential-challengers [2021, 20 December].

Pfeifer, V., Jones, T.E., Velasco Velez, J.J., Massue, C., Greiner, M.T., Arrigo, R., Teschner, D., Girgsdies, F. et al. 2016. The electronic structure of iridium oxide electrodes active in water splitting. *Phys Chem Chem Phys.* 18(4):2292-2296.

Pham, H.H., Nguyen, N.P., Do, C.L. & Le, B.T. 2015. Nanosized IrxRu1−xO2 electrocatalysts for oxygen evolution reaction in proton exchange membrane water electrolyzer. *Advances in Natural Sciences: Nanoscience and Nanotechnology.* 6(025015).

Polonsky´, J., Kody´m, R., Va´gner, P., Paidar, M., Bensmann, B. & Bouzek, K. 2017. Anodic microporous layer for polymer electrolyte membrane water electrolysers. *J Appl Electrochem* 47:1137–1146.

Pourbaix, M. 1974. *Atlas of electrochemical equilibria in aqueous solutions.* Second English Edition. Houston, Texas.

Puthiyapura, V.K., Mamlouk, M., Pasupathi, S., Pollet, B.G. & Scott, K. 2014a. Physical and electrochemical evaluation of ATO supported IrO2 catalyst for proton exchange membrane water electrolyser. *Journal of Power Sources.* 269:451-460.

Puthiyapura, V.K., Pasupathi, S., Su, H., Liu, X., Pollet, B. & Scott, K. 2014b. Investigation of supported IrO2 as electrocatalyst for the oxygen evolution reaction in proton exchange membrane water electrolyser. *International Journal of Hydrogen Energy.* 39:1905-1913.

Qu, H.Y., He, X., Wang, Y. & Hou, S. 2021. Electrocatalysis for the Oxygen Evolution Reaction in Acidic Media: Progress and Challenges. *Appl. Sci. .* 11(4320).

Radowitz, B. 2021. *Recharge: Global News and Intelligence for the Energy Transition.* Available: https://www.rechargenews.com/transition/linde-to-build-world-s-largest-electrolyser-to-produce-green-hydrogen/2-1-944080 [2021, 16 December].

Raja, P.M.V. & Barron, A.R. 2021. *Chemistry Libretexts.* Available: https://chem.libretexts.org/Bookshelves/Analytical_Chemistry/Physical_Methods_in_Chemis

try_and_Nano_Science_(Barron)/02%3A_Physical_and_Thermal_Analysis/2.03%3A_BET_ Surface_Area_Analysis_of_Nanoparticles [2021, 19 December].

Rajan, Z.S.H.S., Binninger, T., Kooyman, P.J., Susac, D. & Mohamed, R. 2020. Organometallic chemical deposition of crystalline iridium oxide nanoparticles on antimony-doped tin oxide support with high-performance for the oxygen evolution reaction. *Catalysis Science & Technology.* 10(12):3938-3948.

Regmi, Y.N., Peng, X., Fornaciari, J.C., Max Wei, M., Myers, D.J., Weber, A.Z. & Danilovic, N. 2020. A low temperature unitized regenerative fuel cell realizing 60% round trip efficiency and 10000 cycles of durability for energy storage applications. *Energy Environ. Sci.,.* 13(2096).

Reier, T., Oezaslan, M. & Strasser, P. 2012. Electrocatalytic Oxygen Evolution Reaction (OER) on Ru, Ir, and Pt Catalysts: A Comparative Study of Nanoparticles and Bulk Materials. *ACS Catalysis.* 2(8):1765-1772.

Sapountzi, F.M., Gracia, J.M., Weststrate, C.J., Fredriksson, H.O.A. & Niemantsverdriet, J.W. 2017. Electrocatalysts for the generation of hydrogen, oxygen and synthesis gas. *Progress in Energy and Combustion Science.* 58:1-35.

Sasaki, K., Takasaki, F.N., Zhiyun, Hayashi, S., Shiratori, Y. & Ito, K. 2010. Alternative Electrocatalyst Support Materials for Polymer Electrolyte Fuel Cells. *ECS Transactions.* 33(1):473-482

Saveleva, V.A., Wang, L., Luo, W., Zafeiratos, S., Ulhaq-Bouillet, C., Gago, A.S., Friedrich, K.A. & Savinova, E.R. 2016. Uncovering the Stabilization Mechanism in Bimetallic Ruthenium-Iridium Anodes for Proton Exchange Membrane Electrolyzers. *J Phys Chem Lett.* 7(16):3240-3245.

Saveleva, V.A., Wang, L., Teschner, D., Jones, T., Gago, A.S., Friedrich, K.A., Zafeiratos, S.,, Schlögl, R. & Savinova, E.R. 2018. Operando Evidence for a Universal Oxygen Evolution Mechanism on Thermal and Electrochemical Iridium Oxides. *The Journal of Physical Chemistry Letters.* 9:3154-3160.

Schmidt, T.J. 1998. Characterization of High-Surface-Area Electrocatalysts Using a Rotating Disk Electrode Configuration. *Journal of the Electrochemical Society* 145(7):2354-2358.

Senthilkumar, V., Senthil, K. & Vickraman, P. 2012. Microstructural, electrical and optical properties of indium tin oxide (ITO) nanoparticles synthesized by co-precipitation method. *Materials Research Bulletin.* 47:1051-1056.

Siemens Energy, 2020-2021. *Siemens Energy: Priorities: Future Technology: Hydrogen.* Available: https://www.siemens-

energy.com/global/en/priorities/futuretechnologies/hydrogen.html#Offerings [2021, 16 December 2021].

Silva, G.C., Venturini, S.I., Zhang, S., Löffler, M., Scheu, C., Mayrhofer, K.J.J., Ticianelli, E.A. & Cherevko, S. 2020. Oxygen Evolution Reaction on Tin Oxides Supported Iridium Catalysts: Do We Need Dopants? *ChemElectroChem.* 7(10):2330-2339.

Speakman, S.A. 2021. *MIT Center for Materials Science and Engineering: Estimating Crystallite Size Using XRD.* Available: http://prism.mit.edu/xray [2021, 20 December].

Spöri, C., Briois, P., Nong, H.N., Reier, T., Billard, A., Kühl, S., Teschner, D. & Strasser, P. 2019. Experimental Activity Descriptors for Iridium-Based Catalysts for the Electrochemical Oxygen Evolution Reaction (OER). *ACS Catalysis.* 9:6653-6663.

Tackett, B.M., Sheng, W., Kattel, S., Yao, S., Yan, B., Kuttiyiel, K.A., Wu, Q. & Chen, J.G. 2018. Reducing Iridium Loading in Oxygen Evolution Reaction Electrocatalysts Using Core–Shell Particles with Nitride Cores. *ACS Catalysis.* 8(3):2615-2621.

Teterin, Y.A., K. I. Maslakov, K.I.,, Murav'ev, E.N., Teterin, A.Y., Bulychev, N.A., Meshkov, B.B. & Stepnov, D.S. 2020. X-Ray Photoelectron Spectroscopy Study of Indium Tin Mixed Oxides on the Surface of Silicate Glass. *Inorganic Materials.* 56(5):507-518.

Verleysen, E., Thorsten Wagner, T., Hans-Gerd Lipinski, H.G., Kägi, R., Koeber, R., Boix-Sanfeliu, A., De Temmerman, P.J. & Mast, J. 2019. Evaluation of a TEM based Approach for Size Measurement of Particulate (Nano)materials. *Materials (Basel).* 12(14).

Walton, K.S.a.S., R. Q. 2007. Applicability of the BET Method for Determining Surface Areas of Microporous Metal-Organic Frameworks. *Journal of American Chemistry Society.* 129(27).

Wang, Z.L. 2000. Transmission Electron Microscopy of Shape-Controlled Nanocrystals and Their Assemblies. *Journal of Physical Chemistry B.* 104(6):1153-1175.

Wei, C., Rao, R.R., Peng, J., Huang, B., Stephens, I.E.L., Risch, M., Xu, Z.J. & Shao-Horn, Y. 2019. Recommended Practices and Benchmark Activity for Hydrogen and Oxygen Electrocatalysis in Water Splitting and Fuel Cells. *Adv Mater.* 31:e180629.
Xu, J., Liu, G., Li, J. & Wang, X. 2012. The electrocatalytic properties of an IrO2/SnO2 catalyst using SnO2 as a support and an assisting reagent for the oxygen evolution reaction. *Electrochimica Acta.* 59:105-112.

Zagalskaya, A. & Alexandrov, V. 2020. Mechanistic Study of IrO2 Dissolution during the Electrocatalytic Oxygen Evolution Reaction. *The Journal of Physical Chemistry Letters.* 11:2695-2700.

APPENDIX A: EXPERIMENTAL

Chemical list:

*PN=Product number

Metal-organic precursor:

Iridium (III) Acetylacetonate ($Ir(acac)_3$), 97% purity, Sigma Aldrich, PN: 333352

ITO support materials:

Indium Tin Oxide (ITO) Nanopowder, $In_{0.95}Sn_{0.05}O_2$, $In_2O_3:SnO_2 = 95:5$, 99.99+% purity, 18 nm, blue, US Research Nanomaterials, Inc.; PN: US3812

Indium Tin Oxide (ITO) Nanopowder, $In_{0.95}Sn_{0.05}O_2$, $In_2O_3:SnO_2 = 95:5$, 99.99+% purity, 20-70 nm, US Research Nanomaterials, Inc.; PN: US3858

Indium Tin Oxide (ITO) Nanopowder, $In_{0.9}Sn_{0.1}O_2$, $In_2O_3:SnO_2 = 90:10$, 99.99+% purity, 18 nm, blue, US Research Nanomaterials, Inc.; PN: US3811

Indium Tin Oxide (ITO) Nanopowder, $In_{0.9}Sn_{0.1}O_2$, $In_2O_3:SnO_2 = 90:10$, 99.99+% purity, 20-70 nm, blue, US Research Nanomaterials, Inc.; PN: US Research Nanomaterials, Inc., PN: US3855

Gases:

Oxygen (O_2), Grade: Research 5.0, Air Liquide

Equipment list:

Analytical balance: RADWAG; AS220/C/2; 407840

Hot plate stirrer: Heidolph Instruments; MR Hei-End; 505-5000-00-1; 110902331

Potentiostat: Bio-Logic Science Instruments; SP-300; 0335

Rotator: Clarion Safety Systems; 12240; 1154-R65WHPL

Rotator motor (Rotating electrode motor): Gamry Instruments; RDE 710; H6019/6057-CJDHPU

Tubular furnace: KILN Contractors; Labofurn; TUB002; TUB002-111-4-3

APPENDIX B: PHYSICAL CHARACTERISATION

High Resolution Scanning Transmission Electron Microscopy: Lattice spacings
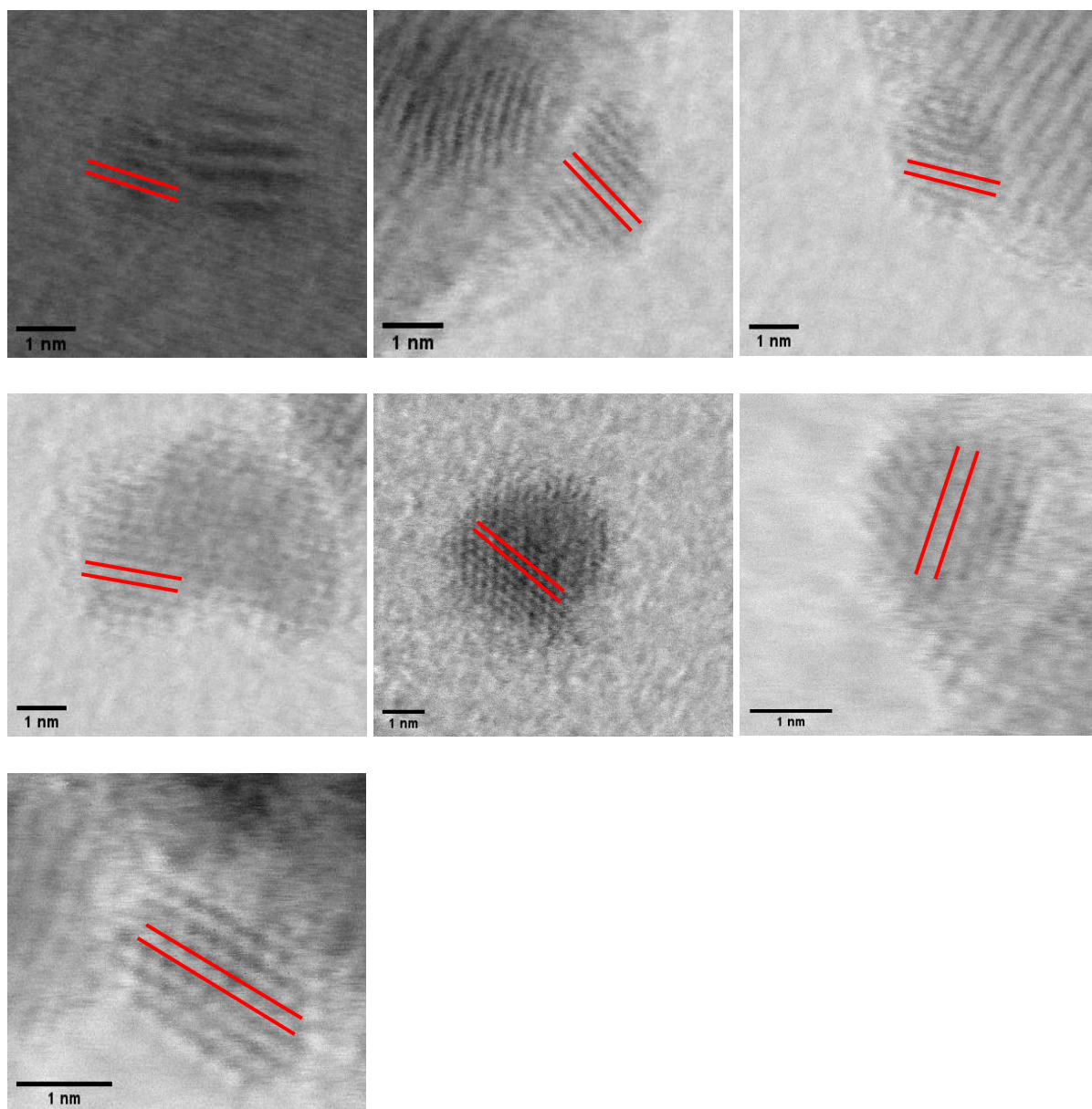

Figure B.1: High resolution-scanning transmission electron microscopy (HR-STEM) micrographs of CAT-A, that were used in the determination of the lattice spacings (indicated by the red parallel lines)

X-ray Photoelectron Spectroscopy: Elemental composition data

Table B.1: Sn/In bulk content compared to the Sn/In surface content

Sample I.D.	Sn/In bulk content (theoretical) (wt.%)	Sn/In surface content (obtained from XPS survey scans) (wt.%)
CAT-A	0.05	0.21
CAT-B	0.05	0.13
CAT-C	0.11	0.18
CAT-D	0.11	0.17

X-ray Photoelectron Spectroscopy: Curve-fitted XPS spectra
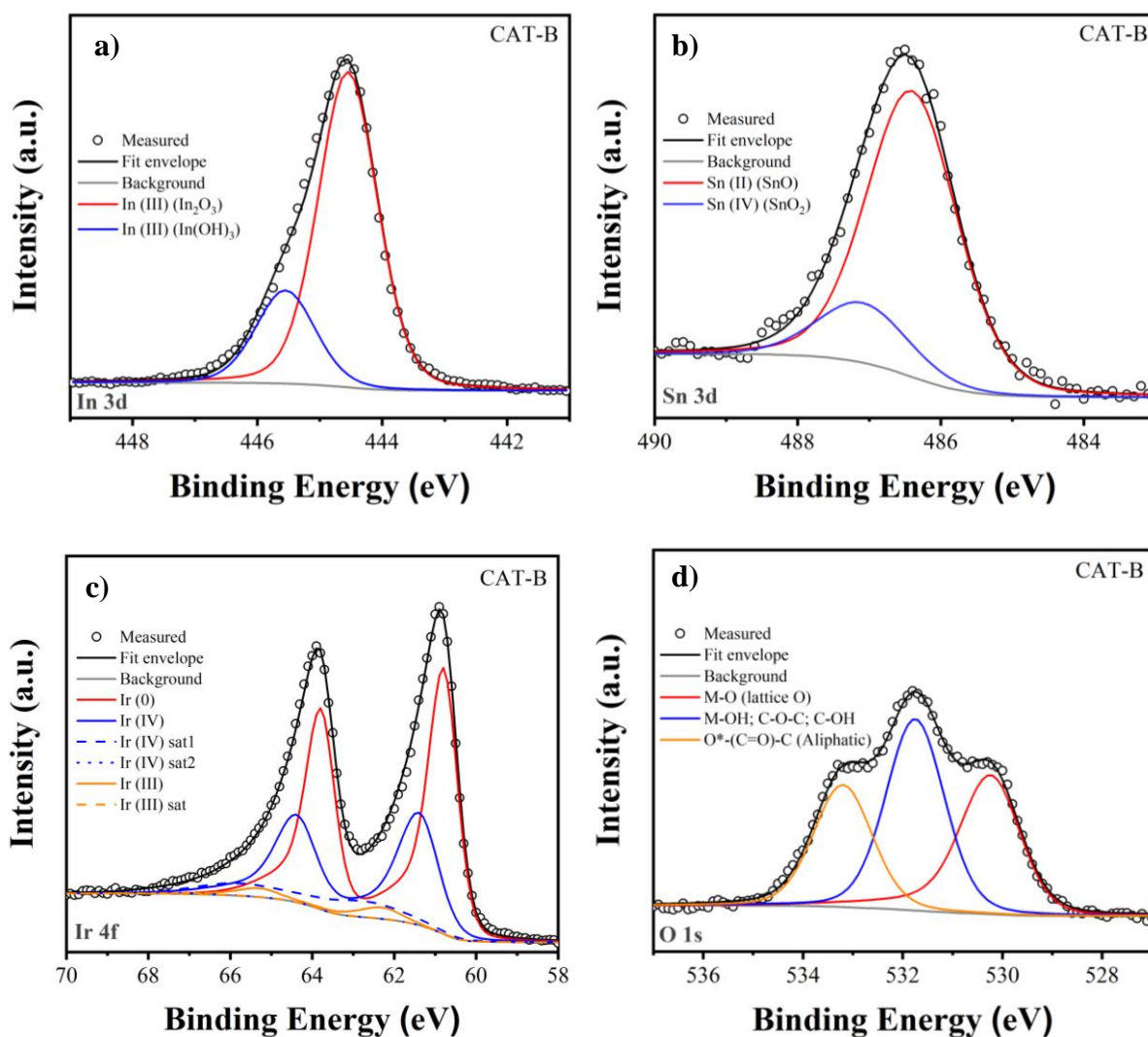

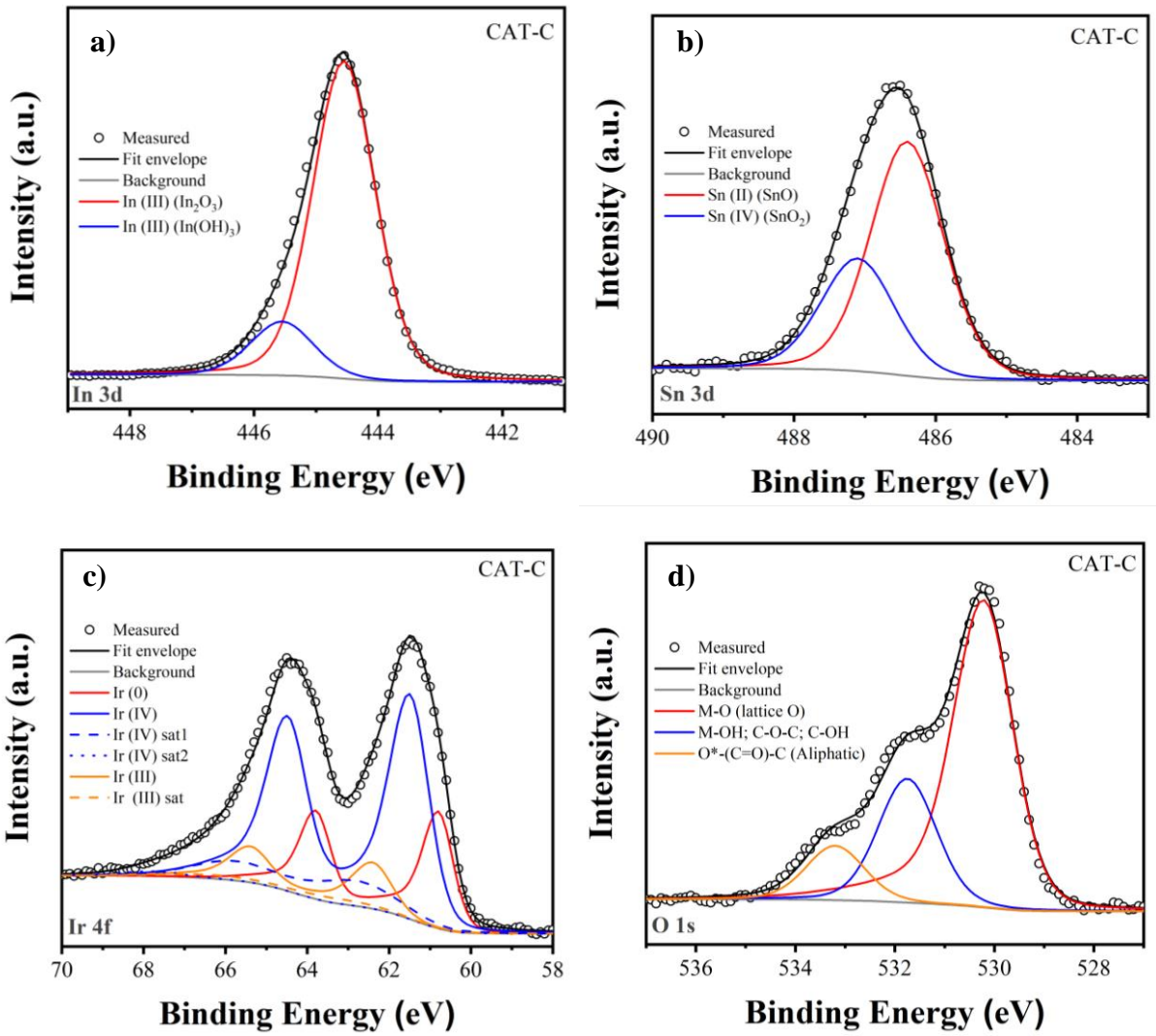**Figure B.2**: Curve fitted XPS spectra for CAT-B of **a)** In 3d, **b)** Sn 3d, **c)** Ir 4f and **d)** O 1s regions.

Figure B.3: Curve fitted XPS spectra for CAT-C **a)** In 3d, **b)** Sn 3d, **c)** Ir 4f and **d)** O 1s regions.
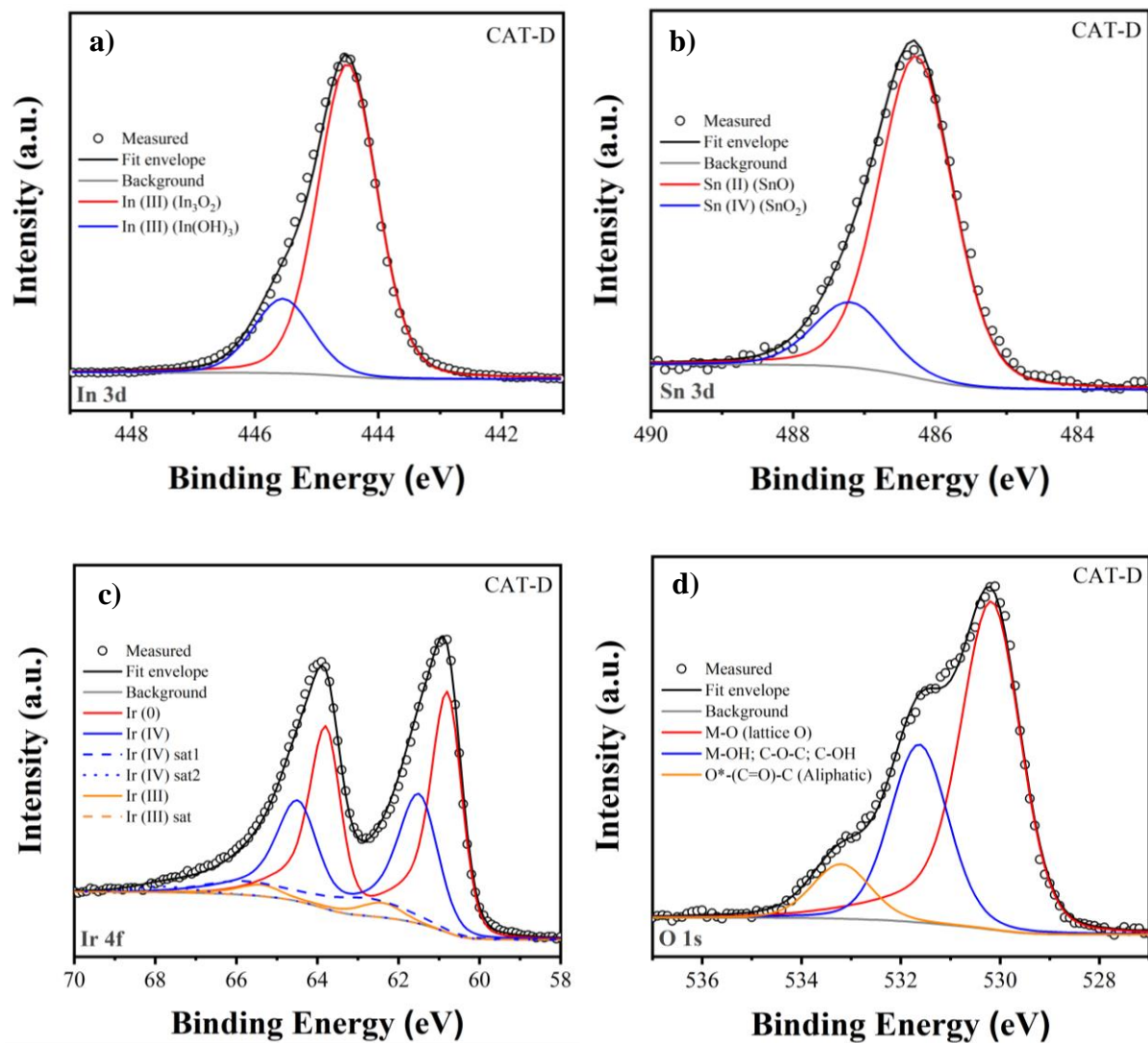
Figure B.4: Curve fitted XPS spectra for CAT-D of **a)** In 3d, **b)** Sn 3d, **c)** Ir 4f and **d)** O 1s regions.

.

APPENDIX C: ELECTROCHEMICAL CHARACTERISATION

Table C.1: The electrochemical OER performance of the MOCD IrO$_x$/ITO electrocatalyst. CAT-B compared to recent studies of unsupported and supported electrocatalysts with IrO$_x$ catalytic nanoparticles with a similar particle size

Deposition technique of Ir species	Support material	IrO$_x$ particle size (nm)	Ir species(s)	Ir loading (wt.%)	Tafel slope value (mV dec^{-1})	Mass-specific OER activity (A g$_{Ir}^{-1}$)			Publication reference
						Potential (V$_{RHE}$) iR-corrected	Reference	CAT-B (This study)	
Solvothermal	ATO	2-3	Rutile IrO$_2$	25	N/A	1.530	63	**255**	(Böhm et al., 2019)
Polyol	ATO	0.5-3	Ir metal and oxyhydroxide IrO$_x$	11	45	1.500	185	**75**	(Hartig-Weiss et al., 2020)
MOCD	ATO	1-5	Rutile IrO$_2$	9	64	1.525	70	**207**	(Rajan et al., 2020)
This study (**MOCD**)	**ITO**	**1-5**	**Ir metal and oxyhydroxide IrO$_x$**	**11**	57	**1.525**	-	207	-
Surface organometallic chemistry (SOMC) + Chemical reduction	ITO	0.5-1	Ir metal and oxyhydroxide IrO$_x$	-	46	1.510	156	**113**	(Lebedev et al., 2020)
Solvothermal	ITO	1-2	Ir metal and oxyhydroxide IrO$_x$	4.1	52	1.510	35	**113**	(Lebedev & Copéret, 2019)